California Energy Commission

Energy Research and Development Division

FINAL PROJECT REPORT

Investigation of Potential Induced Seismicity Related to Geologic Carbon Dioxide Sequestration in California

California Energy Commission

Edmund G. Brown Jr., Governor

PREPARED BY:

Primary Author(s)

William Foxall	Sharon Borglin
Christine Doughty	Katie Freeman
Kyung Jae Lee	Jonathan Ajo-Franklin
Seiji Nakagawa	Preston Jordan
Thomas Daley	Timothy Kneafsey
Elizabeth Burton	Curtis Oldenburg
Corinne Layland-Bachmann	Craig Ulrich

Lawrence Berkeley National Laboratory
1 Cyclotron Rd.
Berkeley, CA 94720-8099

Contract Number: 500-12-010

PREPARED FOR:
California Energy Commission

David Stoms
Project Manager

Aleecia Gutierrez
Office Manager
Energy Generation Research Office

Laurie ten Hope
Deputy Director
ENERGY RESEARCH AND DEVELOPMENT DIVISION

Robert P. Oglesby
Executive Director

ACKNOWLEDGEMENTS

PREFACE

The California Energy Commission's Energy Research and Development Division manages the Natural Gas Research and Development program, which supports energy-related research, development, and demonstration not adequately provided by competitive and regulated markets. These natural gas research investments spur innovation in energy efficiency, renewable energy and advanced clean generation, energy-related environmental protection, energy transmission and distribution and transportation.

The Energy Research and Development Division conducts this public interest natural gas-related energy research by partnering with RD&D entities, including individuals, businesses, utilities and public and private research institutions. This program promotes greater natural gas reliability, lower costs and increases safety for Californians and is focused in these areas:

- Buildings End-Use Energy Efficiency.

- Industrial, Agriculture and Water Efficiency

- Renewable Energy and Advanced Generation

- Natural Gas Infrastructure Safety and Integrity.

- Energy-Related Environmental Research

- Natural Gas-Related Transportation.

Investigation Of Potential Induced Seismicity Related To Geologic Carbon Dioxide Sequestration In California is the final report for the Investigations of Potential Induced Seismicity Related to Geologic Carbon Dioxide Sequestration in California project, Contract Number 500-12-010 conducted by Lawrence Berkeley National Laboratory. The information from this project contributes to Energy Research and Development Division's Energy-Related Environmental Research Program.

For more information about the Energy Research and Development Division, please visit the California Energy Commission's website at www.energy.ca.gov/research or contact the California Energy Commission at 916-327-1551.

ABSTRACT

Geological carbon sequestration (GCS), in which carbon dioxide (CO_2) is injected into a permeable rock layer, could contribute to meeting California's greenhouse gas reduction goals. However, injecting CO_2 could potentially cause earthquakes induced by elevated fluid pressures on faults in the subsurface, and earthquake slip on faults within the caprock seal overlying the storage reservoir could lead to leakage of CO_2 and other contaminant fluid into shallow drinking water sources and to the atmosphere. This study investigated the risks potentially associated with CO_2 sequestration in California and the potential for leakage through faults. Specifically, the study demonstrated a procedure that could be used to assess the risks from induced seismicity at a GCS site to inform planning and regulatory decisions before CO_2 injection begins, and carried out a laboratory experiment to investigate the stability of a fault in a shale caprock when subjected to shear stress loading and elevated fluid pressure. The risk assessment procedure is based upon modeling the flow of CO_2 and pressure buildup in the storage reservoir, and simulations of earthquakes that occur when the pressure front encounters local faults. The flow modeling examined the sensitivity of pressure buildup to the rate of injection and fault permeability, and to mixing of CO_2 with residual methane when the storage layer is a depleted natural gas reservoir like the one selected for the demonstration. Ground motions from the simulated earthquakes were calculated to assess the risk, which in the demonstration scenario is primarily from nuisance caused by ground shaking being felt by people. Multiple seismicity simulations that take into account the uncertainties in geological characterization of the injection site and other modeling parameters were carried out to estimate the uncertainty bounds on the risk. Finally, the report discusses regulatory implications of the study for GCS in California.

TABLE OF CONTENTS

LIST OF FIGURES

LIST OF TABLES

EXECUTIVE SUMMARY

Introduction

Capturing carbon dioxide (CO_2) from sources such as natural gas-burning power plants and injecting it into permeable geologic formations, a process known as geological carbon sequestration, could substantially contribute to meeting California's ambitious greenhouse gas reduction goals. The captured CO_2 gas would be compressed, transported, and injected into a deep underground storage layer where it changes to a supercritical fluid. A supercritical fluid is neither a gas nor a liquid, but can diffuse through a solid like a gas and dissolve other materials like a liquid. The Scoping Plan for the Global Warming Solution Act of 2006 (AB 32) specifically identifies geological carbon sequestration as a strategy that holds significant potential to reduce emissions of this greenhouse gas. California has invested in research on the science, technology, and economics of geological carbon sequestration to investigate this potential.

However, operations that inject fluids into the earth's subsurface under high-pressure can give rise to environmental hazards. These include the potential for triggering or inducing earthquakes by altering the pressure and stress state on critically-stressed faults. To date, induced earthquakes related to CO_2 injection have been limited to micro-earthquakes and a few events that were felt at the surface. Fluid injection, however, for other purposes has induced significant felt and even damaging earthquakes during the past few years. For example, since 2008, the well-publicized series of small to moderate earthquakes as large as magnitude 5.8 in Oklahoma has been associated with the increase in injecting produced wastewater from boosted oil and gas production, assisted, in part by the proliferation of hydrofracturing activity.

A successful geological carbon sequestration project requires a permeable rock formation to pump the CO_2 into and an impermeable layer, called a caprock, above the reservoir to keep the CO_2 from escaping. Slippage along a fault in the caprock seal of a reservoir during an induced earthquake could cause leaks of CO_2 and other contaminant fluids into shallow drinking water sources closer to the surface.

Because injection of CO_2 is similar to other large-volume fluid injection operations, the hazards and risks potentially associated with geological carbon sequestration must be assessed, both to minimize risk during and after injection and gain public acceptance. Experience is currently limited to a few relatively small sequestration projects around the world. Better understanding of this risk, specifically in California, is necessary as the state considers implementing sequestration as a climate strategy.

Project Purpose

This study investigated the potential risks from induced seismic events related to geological carbon sequestration in California. More specifically, the study demonstrates the type of end-to-end procedure that could be carried out before CO_2 injection begins assessing the potential for elevated seismic hazard and risk associated with an industrial-scale geological carbon sequestration project. These potential risks, or a public perception that a risk exists, could present

1

major barriers to commercial application of this strategy to reduce greenhouse gas emissions. The hazard and risk assessment would be used during project planning to inform regulatory and permitting decisions.

Project Process

Currently, there are no commercial sequestration projects operating in California, so no observed data are available to assess induced seismicity directly related to geological carbon sequestration. The first task compiled data relevant to assessing the potential for seismicity (frequency, magnitude, and distribution of earthquakes in a region) related to CO_2 sequestration in California and its associated hazard and risks. These included data from wastewater disposal operations that might be analogous in some respects to CO_2 injection. The data were reviewed by an external advisory committee to determine how useful each data set might be and how it could be used most effectively.

Data related to wastewater disposal available at that time were inadequate to be used as a basis for assessing induced seismicity. Therefore, the decision was made to focus the study on demonstrating a site-specific hazard and risk assessment procedure that employs physics-based simulation of subsurface pressures and induced seismicity, and that makes maximum use of currently available data. This procedure is designed to be used during project planning before injection begins to inform permitting and regulatory decisions.

The procedure analyzes and interprets the available data on rock layers and geophysical logs from wells to construct a geological model of the storage system. This model is used for computer simulations of how CO_2 injected into the geological storage layer at a given rate would flow through the layer and along local faults during and after injection, resulting in increased fluid pressures on the faults. Earthquake computer simulations are then carried out in which induced earthquakes triggered by the changes in fault pressures, and the simulated earthquake sequences are used to estimate the seismic hazard and risk.

The site selected to demonstrate the procedure was King Island near Lodi in the southern Sacramento Valley. King Island had previously been identified as one of the sites in California having the highest CO_2 storage potential. Previous characterization studies conducted at the King Island site had collected a set of data with which to construct the geological model. The data included a comprehensive suite of modern well logs from the Citizen Green #1 research well that had been drilled there. The Mokelumne River Sandstone, a depleted natural gas reservoir at about 1,400 meters depth under King Island, was selected as the target storage formation

Three-dimensional seismic data covering King Island was interpreted to identify local faults that could potentially be sources of induced earthquakes caused by CO_2 injection in the Citizen Green #1 well. The rock mechanical properties used in the earthquake simulations can be calculated from the speeds at which seismic waves propagate through the Earth's crust, which are also used to calculate how the much the ground moves during a seismic event. Direct measurements of seismic wave speeds are available for only a limited depth range in the Citizen Green #1 well. Therefore, regional data and generic relationships for California were used to estimate velocities

and rock properties at greater depths, although these estimates have significant uncertainties. The seismicity simulations also require estimates of underground stresses and of the type and long-term rate of fault slip. Because these are unknown at King Island, these were estimated from regional data for this demonstration.

Simulations were done for injection rates of 8 and 12 million metric tons per year over 20 years into the Mokelumne River Sandstone and a range of assumed fault permeability values. Despite the normal meaning of "depleted," the fact is that depleted gas reservoirs like the Mokelumne River Sandstone may still contain significant amounts of methane. When CO_2 mixes with methane the density of the mixture decreases, which means that the pressure in a gas reservoir can increase even after the injection of CO_2 has stopped. Therefore, an additional flow modeling analysis was carried out to investigate the effect of mixing CO_2 with residual methane on pressure buildup, and its sensitivity to how porous (i.e., how much of the rock volume is taken up by void space) the reservoir is and how permeable the reservoir and faults are (i.e., how easily fluids can flow through them).

The modeled pressure changes on two faults in the King Island geologic model from the 8 million metric tons per year injection were used as input to seismicity simulations. Simulated induced earthquakes were triggered as increasing fluid pressure reduced the frictional resistance of the faults. Earth science data and the parameters interpreted from them generally have significant uncertainties, which translate to uncertainties in the estimated seismic hazard and risk. The seismicity simulation method employed in the study enabled a large number of simulations to be carried out that randomly sample the uncertainties in the input parameters in order to estimate statistical uncertainty bounds on the hazard and risk.

The final technical activity of the study was a laboratory experiment to investigate the effects of elevated fluid pressure and fault slip on the integrity of shale caprock. The experiment measured shear displacement on a fracture in a caprock sample and the change in the fracture's permeability after it had been activated by increasing the fluid pressure. This provided insight into how fast a fault in the caprock might leak if it slipped during an earthquake.

Project Results

The modeling results showed that increasing the injection rate from 8 to 12 million tons per year (more than double that for the largest geological carbon sequestration projects currently planned), increased the magnitudes of pressure changes proportionately, but with little effect on the overall pattern of CO_2 movement or pressure response. Decreasing the fault permeabilities, on the other hand, greatly impacted both where the CO_2 went and how much it changed the pressures. Because fault permeabilities are generally very poorly known in practice, their large impact on pressure change and the flow of CO_2 underground signifies the importance of developing site characterization methods to learn more about fault properties.

Because methane can be compressed under pressure more than water, the study found that the pressure rise at the faults from CO_2 injection is less in a reservoir containing methane than a

reservoir without methane. The study also found that the effect of mixing CO_2 with methane is negligible.

The results for the demonstration hazard and risk scenario at King Island showed a modest increase in the likelihood of ground shaking (the hazard) during and after injection, but these translated to only small increases in the nuisance to people (the risk). The risk of damage even at a site close to the two active faults is very low.

In the laboratory experiment, the fracture sealed immediately after the shale sample was saturated with pore fluid. The result of this sealing effect was that externally applied pore pressures well above the estimated critical pressure for fault activation failed to cause shear displacement on the fracture. Subsequent further increases in shear stress resulted in failure of the bulk rock rather than slip along the fracture. The results of the experiment suggest that self-healing of faults in shales rich in swelling clays may limit the potential for leakage along faults within the caprock of a CO_2 storage reservoir.

Benefits to California

This study demonstrated a procedure assessing the hazard and risk from induced seismicity that could be applied to a real geological carbon sequestration project. The researchers used the best available data from the region around the King Island site or from other sources; however, the hazard and risk results cannot be regarded as definitive for the King Island site. They could be generally indicative of the impact that CO_2 injection might have at sites in California having similar characteristics to the King Island scenario and where the background seismic hazard and risk are low. The CO_2 injection rate of 8 million metric tons per year is substantially larger than the largest geological carbon sequestration projects currently planned, however, is thought to represent future industrial-scale projects.

By sampling ranges of parameter values where the true values are not well known, the researchers were able to identify a number of factors that may significantly affect the level of hazard and risk, such as fault permeability. The study highlights the primary requirement for a real-world application of the risk assessment method will be a comprehensive site characterization that includes site-specific measurements of underground state and rock and fault properties. The study also identifies laboratory- and field-scale research to improve the fundamental understanding of induced seismicity and caprock integrity, and reduce uncertainties in crucial parameters.

This study has made a major contribution to indicating how the risk of induced seismicity from geological carbon sequestration should be assessed during the planning and permitting stage of a project. It has also identified the remaining challenges in putting this assessment to work in practice, such as completing site characterization of uncertain parameters, modeling changes in fault permeability in seismic events with CO_2 flow and understanding fault slip impacts on caprock integrity. This assessment also helps identify what the future research priorities are as the state considers adopting this greenhouse gas reduction strategy while safeguarding ratepayers, property, and the environment. The proposed procedure provides essential

information to guide drafting future regulations, including site criteria and monitoring for a quantification method and permanence protocol for geological sequestration being developed by the California Air Resources Board to ensure stored CO_2 does not leak to the atmosphere from induced seismic activity.

CHAPTER 1:
Introduction

1.1: Background

Geologic carbon sequestration (GCS), whereby CO_2 captured from stationary point sources such as power plants is injected into permeable geologic formations, is considered to be a promising means of decreasing CO_2 concentration in the atmosphere while minimizing the economic disruption in moving towards low-carbon energy generation. Sedimentary basins in California, particularly in the Central Valley, have substantial CO_2 storage potential, and it has been recognized that GCS could substantially contribute to meeting the state's ambitious greenhouse gas reduction goals (Burton et al., 2016). California's Scoping Plan for the Global Warming Solution Act of 2006 (AB 32) specifically identifies GCS as a strategy that holds significant potential to reduce emissions of this greenhouse gas.

However, GCS projects, like other fluid injection operations, can give rise to several environmental hazards that need to be addressed. These include the potential for inducing earthquakes of concern by altering the pressure and stress state in the subsurface. Furthermore, it has been suggested that slip along a fault in the caprock seal of a subsurface reservoir during an induced earthquake could increase the permeability of the fault leading to leakage of CO_2 and other contaminant fluids into shallow drinking water sources.

1.2: Overview of the Potential for Seismicity Related to CO_2 Injection

Most earthquakes occur when the tectonic shear stress acting parallel to a fault in the Earth's crust overcomes its frictional resistance to slip, causing the two sides of the fault suddenly to slide past each other. The slip resistance, or strength, derives from the component of the stress perpendicular (normal) to the fault plane, which forces the two sides of the fault together. Fluid pressure within the fault acts in the opposite direction to the tectonic normal stress, so that the effective stress determining the strength of the fault is equal to the tectonic normal stress minus the pressure. Therefore, an earthquake can occur, either when the shear stress increases or the effective normal stress decreases, reducing the fault strength. Fault slip triggered by a decrease in effective stress resulting from increased fluid pressure within a fault under constant shear stress is considered to be the primary cause of fluid-induced seismicity. In the case of GCS, induced earthquakes can potentially occur when the plume of elevated pressure propagating away from the injection well encounters a fault that is close to slipping under the prevailing stress state, i.e., critically stressed.

Induced earthquakes related to CO_2 injection to date – for either long-term storage or enhanced oil recovery – have been limited to small (magnitude 1 or less) micro-earthquakes and a few felt events (White and Foxall, 2016). For example, the seismic networks monitoring the largest (1 million tonnes between 2011 and 2014) demonstration GCS project to date in the U.S. at Decatur,

Illinois, recorded about 10,000 events in the magnitude range -2 to 1. However, fluid injection for other purposes – most notably for disposal of large volumes of wastewater produced along with oil and gas in the mid-continental U.S. – has induced significant felt and even damaging earthquakes up to magnitude 5.8 during the past few years (e.g. Yeck et al., 2017; Ellsworth, 2013; Keranen et al, 2013). Since injection of CO_2 is similar in some respects to these other injection operations, the hazard and risk potentially associated with GCS projects need to be assessed quantitatively, both to minimize risk during and after injection and to gain acceptance of the technology by the public.

In a comprehensive review of induced seismicity related to energy technologies, including oil and gas and geothermal production, the National Research Council (2013) identified the net fluid balance – i.e., the net volume change in a formation resulting from both injection and production – as the most important factor governing the likelihood of induced seismicity. They identified GCS as one technology that may have the potential for inducing large events because industrial-scale GCS envisions injecting large volumes (up to billions of tonnes) of CO_2 over long periods of time, with no production to balance the injection. This would lead to over pressuring large volumes of the subsurface, hence increasing the probability that a plume of elevated pressure (i.e. above the pre-existing in situ fluid pressure) will encounter a critically-stressed fault capable of generating seismicity of concern. A more recent study by Weingarten et al. (2015) found that seismicity associated with wastewater disposal in the U.S. is correlated with the rate of fluid injection rather than the net volume accumulated over decade-long time periods, because a sharp increase in the rate of injection over a time interval significantly shorter than the pressure diffusion time scale can result in a rapid buildup of overpressure.

1.3: Assessment of Hazard and Risk from Induced Seismicity

The focus of this study is assessment before the start of injection of potential risks from injection-induced seismicity. This type of risk assessment would be used to inform regulatory and permitting decisions. Induced seismicity risks can be assessed using the same overall Probabilistic Seismic Risk Analysis (PSRA) approach commonly used to estimate the risk of structural damage from naturally-occurring earthquakes, but with important modifications (White and Foxall, 2016). PSRA combines the probabilities of different levels of earthquake ground shaking occurring (the hazard) with their consequences. In the case of induced seismicity, the potential consequences are structural damage and nuisance to people in the vicinity of the project caused by felt ground shaking.

The first modification to conventional PSRA concerns estimation of earthquake occurrence frequencies (frequency-magnitude distribution) that are used to calculate the hazard. Whereas in conventional PSRA earthquake occurrence is usually assumed to be stationary in time and uniformly distributed on each earthquake source, the occurrence of fluid-induced seismicity is strongly time- and space-dependent as a result of the growth of the pressure plume away from the injection point. Furthermore, estimation of earthquake occurrence frequencies is usually based on a record of past seismicity and long-term tectonic fault slip rates. Given that no induced

seismicity record can exist before the start of injection, a method of estimating induced earthquake frequency-magnitude distributions at this pre-injection stage that is dependent on injection-induced time- and space-dependent subsurface pressure changes is required.

The second modification is needed to account for the risk of nuisance from shallow earthquakes as small as about magnitude 2, which requires alternative methods of calculating earthquake ground shaking from small earthquakes at close distances. This is because the empirical ground motion prediction equations usually used in PSRA are very poorly constrained below magnitude 6 and at short distances.

This study demonstrates an end-to-end procedure that could be carried out to assess the elevated seismic hazard and risk that potentially could be associated with CO_2 injection at a specific site. The procedure is centered on hazard assessments that utilize physics-based simulations of induced and natural earthquake sequences. Subsurface fluid pressure changes over time during and after injection are calculated within a site geological model by hydrological simulation of given injection scenarios. The pressure time histories are passed to a numerical earthquake simulation program where they modify the effective normal stress distributions on faults within the model, which are also subject to a long-term tectonic loading rate. The induced earthquakes in the resulting simulated seismicity sequences therefore depend directly on injection parameters and exhibit the expected time- and space-dependencies. An analytical method is used to propagate seismic waves from the earthquake sources through the site geological model to calculate ground motions at the Earth surface.

An integral and important part of probabilistic hazard and risk assessment is estimating the uncertainty in the results. Earth science data and model parameters are inevitably often subject to large uncertainties. Therefore, multiple realizations of seismicity time histories (catalogs) that randomly sample the uncertainty distributions of the simulation model parameters are needed to bound the uncertainties in earthquake occurrence frequencies, and hence in the hazard.

The site chosen for the demonstration is on King Island, about 20 km southwest of Lodi in the southern Sacramento Valley of California. The choice of King Island and the final work scope carried out in the second phase of the project followed the recommendations of an external Project Advisory Committee (PAC), based upon their review of statewide data collected during the first phase and a set of alternative in-depth studies proposed by the project team. In addition to King Island having been identified as one of the sites in California having the highest CO_2 storage potential (Burton et al., 2015; 2016), the PAC's recommendations rested largely upon the database already available for the site.

1.4: Project Work Flow and Report Organization

Chapter 2 discusses the data and sample collection during the first phase of the project and the PAC recommendations that formed the basis for the final project scope of work. Chapter 3 describes analyses carried out in the second phase of site-specific and regional data to estimate hydrological, material and stress parameters needed for the simulation-based PSRA demonstration. Hydrological flow modeling at King Island to synthesize the subsurface pressure

changes input to the seismicity simulations and to assess the sensitivity of pressures to variations in injection volume and fault permeability is described in Chapter 4. Chapter 5 investigates the effects of mixing of CO_2 with residual methane on long-term pressure buildup in a depleted natural gas reservoir, like the target storage formation at King Island. Chapter 6 contains a detailed discussion of the simulation-based induced seismicity risk assessment approach, and describes its application to one of the synthetic injection scenarios at King Island. Chapter 7 discusses the potential for leakage of CO_2 and other contaminants to the atmosphere and drinking water sources through caprock faults, and describes the conduct and results of a laboratory experiment to investigate the mechanical and hydrological effects of elevated fluid pressure and fault slip on shale caprock integrity. Technology transfer and regulatory aspects are explored in Chapter 8. Chapter 9 presents the project's conclusions.

CHAPTER 2:
Project Objectives and Technical Scope of Work

2.1: Project Objectives

The original overall objective of the study presented in this report was to investigate the potential for induced seismicity related to GCS in California. Upon completion of the first, data collection and review, technical task of the project, this broad objective was refined to focus on demonstrating a procedure for assessing the hazard and risk from induced seismicity at a specific site, and to investigate the potential for CO_2 leakage caused by earthquake slip on a fault in a shale caprock.

2.2: Original Technical Tasks

The project technical work scope comprised three tasks, Tasks 2.1, 2.2 and 2.3. The goal of Task 2.1 was to identify and acquire data and rock samples that could be used to investigate the potential for induced seismicity and related fault leakage caused by GCS in California. The goal of Task 2.2 was to carry out data-driven analyses and simulation and experimental studies to investigate the potential for GCS-related induced seismicity. The nature and scope of the Task 2.2 research was to be determined by evaluation of the data sets and samples assembled in Task 2.1 under the guidance of the external PAC convened at the end of that task. The objective of Task 2.3 was to make the knowledge gained, experimental results and lessons learned during Task 2.2 available to decision makers.

The results of Task 2.1, the conduct of the PAC workshop, its ensuing recommendations and the final Task 2.2 work scope, and the scope of Task 2.3 are described in the remainder of this chapter. The analyses, modeling and experiments carried out in Task 2.2 are described in Chapters 3 through 7 of the report. Task 2.3 technology transfer activities are discussed in Chapter 8.

2.2.1: Task 2.1; Identify and Acquire Data and Samples

Existing, publically-available data sets and rock samples to be acquired during this task included:

- Injection and production volume rates and injection pressures from oilfield wastewater and other deep injection operations.
- Seismicity catalogs for oil-producing basins in California.
- In-situ stresses in the vicinity of potential GCS sites identified in previous studies.
- Fundamental information on subsurface CO_2 phase changes and, in particular the effects of CO_2 mixing with methane (CH_4) in depleted gas-producing formations, that may affect pressure buildup in storage reservoirs.
- Rock cores and outcrop samples of key caprock sealing formations at high-potential storage sites identified in previous studies that could be used in experiments to study flow characteristics of faults and fractures.

Injection and Production Data: Underground Injection Control (UIC) Class II wells are used to inject water produced along with oil and gas. Some of these wells are used to enhance oil production by injecting produced water to sustain pressure and provide a force to drive more oil to production wells. Other Class II wells are used to inject water into zones that contain only water already. These latter wells can be considered as a subcategory of Class II wells whose entire purpose is to dispose of produced water. The injection rates and cumulative produced volumes in many of these wells approach those planned for GCS projects, at least in the immediate future, and have been associated with several recent cases of significant induced seismicity in the U.S. mid-continent. Therefore, injection volumes and pressures for Class II wastewater disposal wells contained in the publically available California Department of Oil and Gas Resources (DOGGR) production and injection databases (ftp://ftp.consrv.ca.gov/pub/oil/new_database_format) were compiled and reviewed. The potential for induced seismicity is related to the net fluid balance – i.e. injection minus production – in a particular oil reservoir or pool, and LBNL had previously carried out preliminary analyses of net fluid flux from reservoir formations identified as high-potential storage candidates, the Stevens, Vedder and Temblor formations in the Southern San Joaquin Basin. U.S. Environmental Protection Agency (EPA) permit data (https://www.epa.gov/uic/underground-injection-control-permits-region-9) were also collected for two high-volume UIC Class I wells (industrial waste fluid disposal) in the vicinity of Stockton.

Seismicity Data: Routine seismic monitoring in California is currently carried out using the California Integrated Seismic Network (CISN) operated by the U.S. Geological Survey (USGS) in partnership with the University of California, Berkeley and the California Institute of Technology. CISN forms part of the nationwide Advanced National Seismic System (ANSS). Earthquake locations, magnitudes and source parameters are compiled (together with pre-CISN data) into the ANSS Composite Earthquake Catalog, which is available from the USGS, the Northern California Earthquake Data Center (NCEDC), and the Southern California Earthquake Center (SCEC) Data Center (SCECDC). Catalogs of high-precision relative locations are also available for northern (update to Waldhauser and Schaff, 2008) and southern (Hauksson et al., 2012) California from the NCEDC and SCECDC, respectively. A catalog of refined southern California earthquake focal (source) mechanisms (Yang et al., 2012) is available from the SCECDC. The following catalog data were downloaded:

- ANSS Composite Earthquake Catalog, 1973-2014
- Northern California high-precision locations, 1984-2011
- Southern California high-precision locations, 1981-2011
- Southern California refined focal mechanisms, 1981-2010

ANSS data for the period 2005-2012 were used to construct a map of the current spatial distribution of the estimated minimum magnitude of complete detection, M_c, by the CISN. The M_c in a particular area is an important parameter in statistically investigating possible correlations between seismicity and injection. Preliminary demonstration correlation analyses were carried out for the Santa Maria and Ventura basins using the compiled injection and seismicity data.

In addition to the seismicity, the U.S. Quaternary Fault and Fold database, http://earthquake.usgs.gov/hazards/qfaults and UCERF3 fault model (Field et al., 2014) were

downloaded. These two databases contain comprehensive data on active and potentially active earthquake source faults in California.

CO$_2$-CH$_4$ Mixing: Theoretical information on CO$_2$-CH$_4$ mixing was compiled, and an initial plan for modeling the effect of mixing on long-term pressure build-up in depleted gas reservoirs was developed.

In Situ Stress: Worldwide in situ stress measurements from borehole data and earthquake focal mechanism have been compiled into a database by the World Stress Map Project (Heidbach et al., 2008),
http://dc-app3-14.gfz-potsdam.de/pub/stress_data/stress_data_frame.html). The entire database was downloaded in .csv and .kmz formats. The latter enables the database to be plotted and interrogated directly in Google Earth. The stress data are relatively dense in the southern San Joaquin Valley, but sparse elsewhere.

Caprock Seal Samples: Very little information is available on the geomechanical properties of shale seals in general, and particularly in California. The most complete publically-available collection of core samples available for California is held by the California Well Sample Repository at the California State University, Bakersfield (CSUB). Unfortunately, relevant samples could not be found by searching the inventory catalog (http://www.wellsample.com/catalog.html) and through discussion with Prof. Janice Gillespie of CSUB. This appears to be a result of the historic disinterest in seal rocks in California because hydrocarbon resources have not been successfully recovered from them. However, core samples of the Nortonville shale had been obtained during a previous study of the high-potential GCS site at King Island, near Stockton in the southern Sacramento Valley, and preserved at LBNL. The Nortonville shale is one of the potential seal formations at King Island and at other potential storage sites in northern California.

The Task 2.1 work scope originally proposed included a preliminary investigation of whether data exist to explore the role, if any, seismicity and faults play in migration of oil and gas resulting in "missing" or dry hydrocarbon reservoirs. A brief assessment indicated that this probably would not be a fruitful avenue of investigation within the limited scope of the task.

2.2.2: Project Advisory Committee Workshop

LBNL assembled the data compiled during Task 2.1 for presentation to the PAC in a workshop in San Francisco on December 18, 2014 (during the annual fall meeting of the American Geophysical Union). The panel comprised the diverse group of subject matter experts listed in Appendix A, which also includes the workshop agenda. In addition to presenting the data, LBNL presented the following draft set of potential Task 2.2 research activities for the panel's review:

1. Estimation of net injection (positive fluid flux) into oil pools that are representative of potential CO$_2$ storage formations in California, and spatio-temporal analysis of the correlation of net injection, volume rate and overpressure with seismicity. These analyses would focus on pools having high wastewater injection rates.
2. Characterization of in situ stresses at high-potential CO$_2$ storage sites in relation to faults and fractures.

3. Geomechanical modeling of cases identified in (1) constrained by stress and fault characteristics to investigate the physics and mechanics of fluid-induced earthquakes in high-potential CO_2 storage reservoirs.
4. Hydrological modeling of the King Island site to provide pressure change histories along faults for input to induced seismicity simulations, and to investigate the potential for CO_2-CH_4 mixing to contribute to increased pressure in a storage system.
5. Laboratory measurements on Nortonville core from King Island to determine caprock properties and deformation mechanisms that influence induced seismicity and leakage.
6. Preliminary simulation-based induced seismicity hazard and risk assessment using King Island as a demonstration site and the results of the analysis, modeling and experimental measurements as constraints. These simulations would augment the geomechanical modeling in investigating the general potential for induced seismicity in the tectonic environment of the Central Valley.

The PAC's report and recommendations are presented in Appendix B and summarized here.

The PAC agreed that Activity 1 and the associated Activities 2 and 3 would be valuable in understanding the potential for fluid-induced seismicity associated with injection into high-potential CO_2 storage reservoirs in California generally. However, the committee pointed out that the success of these activities would depend on the quality of available data, especially reservoir pressures, in situ stresses and reservoir properties. As the quality of at least some of the data presently available in publically-accessible databases is probably inadequate for the proposed analyses, and apparent inconsistencies among the seismicity databases would need to be resolved, Activity 1 was not judged a high priority given the limited resources available.

The PAC's primary recommendation was that Task 2.2 activities and resources should be focused on the King Island site. This is because previous work centered on the Citizen Green #1 (CG1) deep research well located there provides a good basis for research important to assessing the potential for fluid injection-induced seismicity in California. The advantages of focusing on King Island they identified were:

- The relevance of King Island to GCS in California. One high-potential and two other potential storage reservoirs together with regionally persistent shale seals are present at the site.
- The geologic structure at King Island is appropriate for modeling studies of storage and induced seismicity in that preliminary assessment suggested that the lower storage formations are fault bounded on two sides.
- The large database available from the previous project, including shale seal core, comprehensive logs from the CG1 well, logs from nearby wells, and a 3D seismic survey.
- Results from previous analyses, including log interpretation, core measurements, and reservoir modeling.

The PAC therefore recommended that the Task 2.2 work scope comprise Activities 4 to 6 summarized above. Specifically, the committee identified laboratory measurements on the Nortonville core as a potentially unique contribution to advancing understanding of the geomechanical properties of shale seals. They urged that the laboratory work include experiments to address the mechanics of fault slip in fractured shale under shear loading and its impact on fluid leakage. The PAC concurred that the hydromechanical modeling effort (Activity 4) should

14

incorporate investigation of the effects of CO_2-CH_4 mixing. They were of the opinion that King Island would offer a good test scenario to support continued development of a simulation-based framework for seismic hazard and risk assessment for induced seismicity in the Central Valley. The committee recommended that fault properties and long-term slip rates be calibrated against observed induced seismicity and fault long-term slip rates in the Central Valley, to the extent that these data are available, and to a degree consistent with available project funding resources.

2.3: Final Task 2.2 Technical Scope of Work

Based on the PAC recommendations, the final technical scope of work comprised Activities 4 to 6 above. Activity 4 was split into two sub-tasks; the first to further develop the King Island TOUGH2 hydrological model and to provide input to Activity 6 earthquake simulations, and the second a parallel flow modeling effort using a smaller geological modeling domain to investigate the effects of CO_2-CH_4 mixing. The pressures in the larger model could be modified to include to perturbations resulting from mixing, if they proved to be significant. Following the PAC recommendations, the scope of Activity 5 experimental work was to focus on direct shear experiments on the Nortonville shale to investigate changes in permeability caused by induced fault slip.

2.4: Task 2.3; Technology Transfer

As a part of the Energy Commission's research program, each study must have a plan and process for demonstrating how the technology or technical concepts developed by the research project results can be usefully transferred to stakeholder entities in California. In this case, the research is fundamental and timely to the development of the Carbon Capture and Storage (CCS) regulatory landscape in the state. The issue of the potential for induced seismicity caused by GCS at industrial-scale has been raised at both the state and national levels. After WESTCARB's experience in collaborating with various industry partners in permitting and siting GCS projects in California (summarized in Chapter 8), WESTCARB convened a panel of international experts who advocated for the funding of studies specific to improving the technical basis upon which to formulate regulations. The Energy Commission then provided such funding and awarded this research project. As described in Chapter 8, to date the process for permitting GCS projects in California has not dealt with the issue of induced seismicity in a consistent manner. This report will provide the basis for developing more consistency in technical approaches of future permitting proceedings and formulation of future regulations and statutes.

Most immediately, this report's findings are providing foundational information for the California Air Resources Board to set site selection criteria for GCS as part of its development of a CCS Quantification Methodology (QM) for the Cap-and-Trade and Low Carbon Fuel Standards (LCFS) programs, and potentially other state programs such as the Emission Performance Standard administered by the California Energy Commission and the California Public Utilities Commission. The CCS QM will provide standard accounting and reporting methods for quantifying greenhouse gas (GHG) emission reductions from CCS projects along with protocols for site selection and monitoring to ensure the GHG emissions reductions are real, permanent, quantifiable, and verifiable. To achieve this, the QM will need to include criteria, specifications,

or other requirements to ensure selection of a proper injection site that minimizes the likelihood of potential CO_2 surface leakage and maximizes CO_2 trapping in the underground target storage complex. Assessing the potential for and establishing monitoring requirements for induced seismicity and associated fault leakage are important elements in site selection and certification of storage permanence.

CHAPTER 3:
King Island Site Characterization

3.1: Well Logs and Stratigraphic Data

The location of the King Island Site is shown on Figure 3.1. The CG1 stratigraphic well was drilled on King Island in 2011 to a vertical depth of 2,110 m to characterize CO_2 storage target formations in a depleted natural gas reservoir and underlying saline formations (Beyer et al., 2012). The potential storage reservoirs at King Island are the Domengine, Mokelumne River, and Starkey sandstone formations, overlain by Nortonville, Capay, and H&T shale caprock, respectively (Figure 1).

Figure 1: Location of the King Island Drill Site
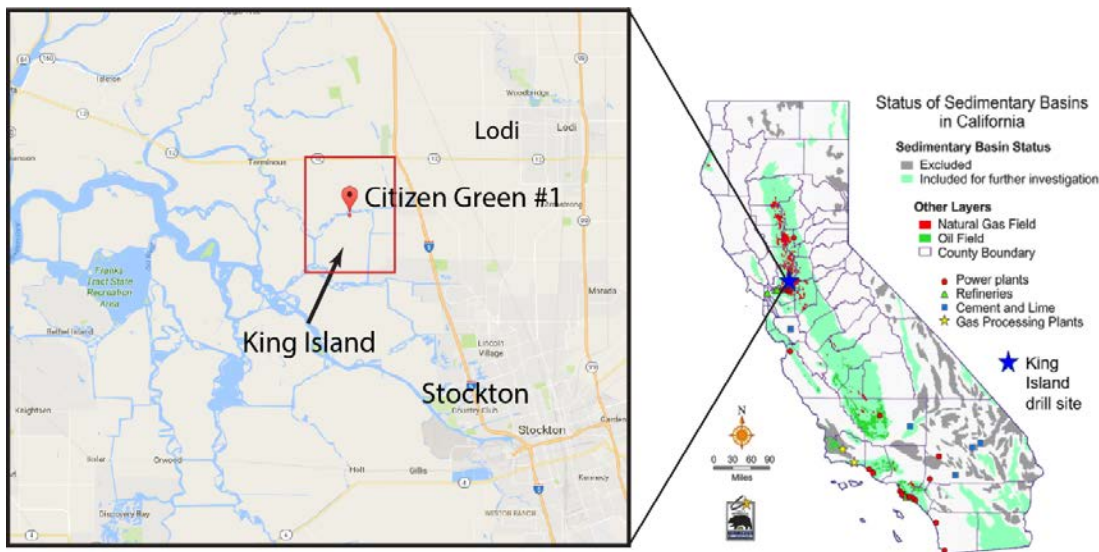
The red rectangle surrounding the CG1 well shows the area covered by the 3D seismic data discussed in Section 3.5.2.

Credit: California map from Burton et al. (2016).

A large volume of data had been collected from the well, including a comprehensive suite of high-quality, modern well logs and 20 and 50 feet of sealed whole core from the Nortonville shale and upper Mokelumne River Sandstone, respectively. Stratigraphic analysis of the logs from CG1 and an east-west line of five nearby wells was tied back to the type well, Union; Empire Tract #1, located 3.5 km to the west. The well logs used to estimate rock formation properties for the studies described in this report are listed in Table 1, with references to on-line sources that describe how each property is derived. The permeability and porosity depth profiles used to model subsurface pressure changes and CO_2 saturation from injection were derived from the Schlumberger Combinable Magnetic Resonance (CMR) log.

Table 1: Rock Properties Measured Using Citizen Green #1 Well Logs

Well log	Property	Comment
Gamma-gamma scattering	Density[1]	
Neutron	Porosity[2]	In conjunction with density
Nuclear magnetic resonance (NMR)	Porosity[3], permeability[4]	Schlumberger Combinable Magnetic Resonance (CMR) tool
Deviation	Well inclination and azimuth	
Sonic	P- and S-wave velocities[5]	

References: (1) http://petrowiki.org/Density_logging

(2) http://wiki.aapg.org/Density-neutron_log_porosity

(3) http://petrowiki.org/Porosity_determination_with_NMR_logging

(4) http://petrowiki.org/Permeability_estimation_with_NMR_logging

(5) http://petrowiki.org/Acoustic_logging

3.2: Fault Identification from Interpretation of 3D Seismic Data

3.2.1: Background

The first step in an induced seismic risk assessment is to identify individual faults or fault zones that may be capable of generating seismicity of concern should they be activated by subsurface pressure and stress changes resulting from fluid injection. This is carried out during site characterization using geologic mapping, seismic reflection surveys, well data, and recorded natural micro-earthquakes. The main factor controlling the maximum earthquake magnitude that a fault can produce is its area. Figure 2 shows a commonly used relationship between fault rupture diameter, stress drop, and earthquake moment magnitude (e.g. Scholz, 2002); this relationship assumes a circular rupture geometry, so that fault length (diameter) can be related to maximum rupture area. For example, the relationship indicates that a one km-long fault is potentially capable of generating maximum earthquakes in the M3 to M4 range, which would likely be felt in nearby communities and possibly cause minor cosmetic damage. If the fault is present in the caprock seal, the rupture could extend several hundred meters vertically above the storage reservoir.

Figure 2: King Island Stratigraphic Section and Citizen Green #1 Well Trajectory
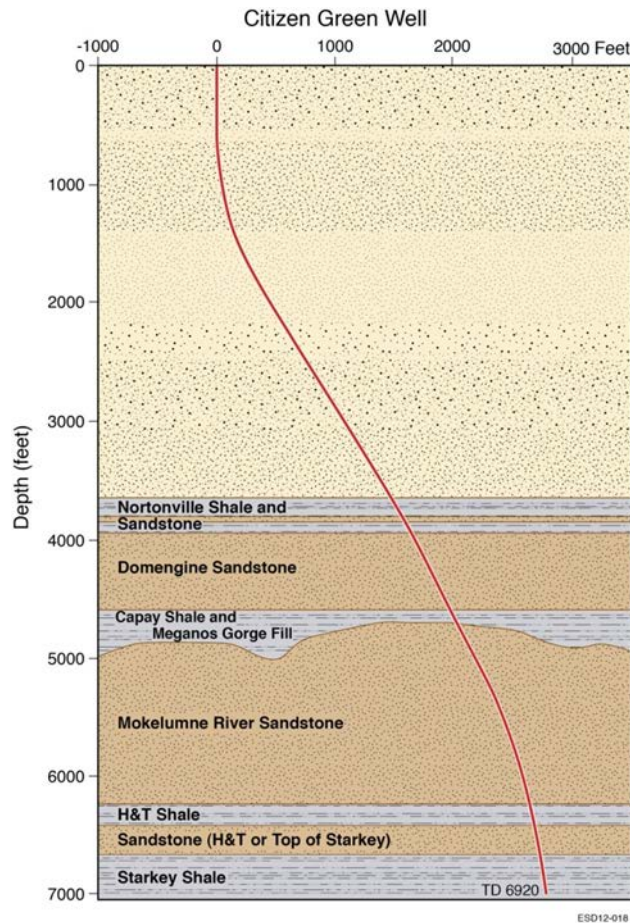
It is expected that an active-source surface seismic reflection survey will form part of the initial site characterization for any future GCS project. The primary use of surface seismic is to image laterally coherent reflections (horizons) related to interfaces that juxtapose contrasting rock properties in the subsurface. The images are then interpreted for subsurface structure, lithology and physical properties. The likelihood of detecting a fault in the subsurface depends first on its size. According to Figure 3, the one km-long fault capable of generating an earthquake of concern discussed above typically would be at the threshold of detection and may be missed in a seismic survey. Actual fault detectability achievable in a given seismic data set is highly specific to the particular site and the survey configuration. To first order, detectability is determined by the amount the fault offsets reflecting horizons vertically and the spatial resolution of the data; i.e. the ability to 'see' offset interfaces.

Careful assessment of the structural geology at a given site and of the resolution of available seismic survey data is necessary to place a lower bound on the size of detectable faults. Apart from interpretation of data from multiple wells, if they are available, the most effective way to detect and characterize smaller faults is to monitor and accurately locate local microseismicity as injection proceeds.

Figure 3: Relationship Between Fault Rupture Length and Earthquake Magnitude
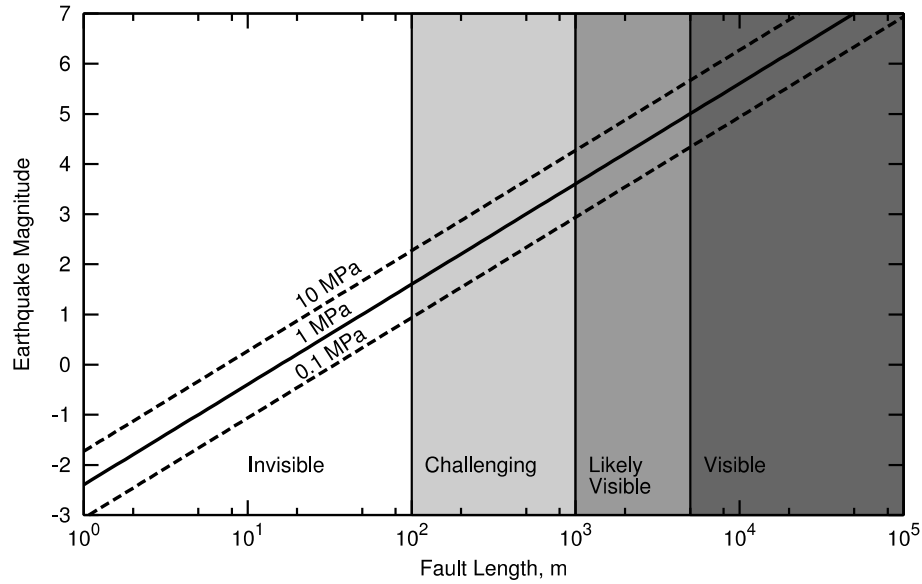
Relationship assumes circular rupture. Solid and dashed lines indicate the commonly observed range of earthquake stress drops. Shaded regions denote typical visibility of faults of different sizes using 3D seismic.

Credit: Reproduced from White and Foxall (2016).

3.2.2: Seismic Resolution

An example of fault interpretation based on offset horizons is shown in Figure.4, in which interpreted splay faults having 15 and 30 m of offset (throw) can be seen. The figure shows time sections in which the vertical axis is measured two-way travel time. Time-to-depth conversion is performed using a subsurface seismic velocity model (see Section 3.3), but depths are always uncertain to some degree because of uncertainties in the velocity model. The uncertainty can be reduced using well sonic logs (Section 3.3) and vertical seismic profiles (VSP) constructed by recording waveforms from surface seismic sources on downhole sensor arrays.

A common estimate of the inherent spatial resolution of seismic data is one-fourth of the wavelength of the data, which is a function of seismic wave velocity and the recorded frequency. The data are relatively high frequency; the 15 m offset is equivalent to about one wavelength and so is easily observed. More typical surveys have wavelengths of 50–100 m, giving a quarter-wavelength resolution of 12–25 m. More advanced techniques than using horizon offsets to detect faults employ mapping of various seismic "attributes" in 3D data to identify more subtle characteristics related to some disruption in the seismic wave propagation.

Figure 4: Example Faults in Surface Seismic Data
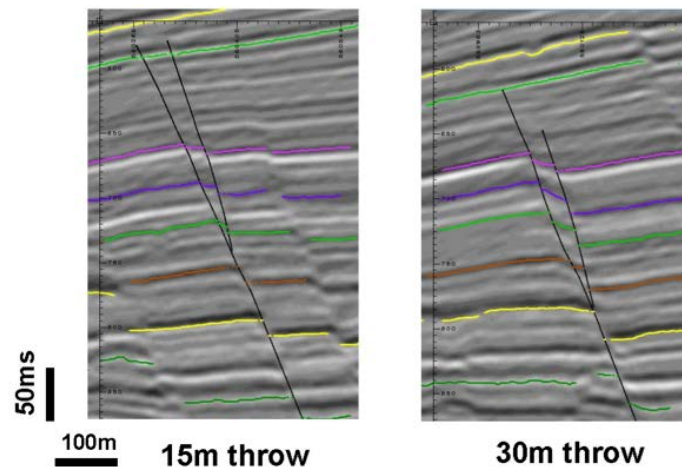
Fault is solid black line with one splay fault interpreted. Fault throw 15 m (left), 30 m (right).

Credit: Fault Analysis Group (2014).

Strike-slip faults, upon which the predominant sense of displacement is horizontal, do not significantly offset approximately horizontal reflectors and so are usually difficult to detect in seismic data, even if they have accumulated substantial lateral slip. Faults within the basement or in other geologic units where there are no or only widely-spaced stratigraphic interfaces are similarly difficult to detect.

3.2.3: Interpretation of 3D Surface Seismic Data at King Island

The same work plan that would be employed for a typical GCS project was followed for the King Island fault characterization. The first task is to search for existing, commercially available 3D seismic surveys before considering acquisition of new data. Part of a 3D seismic survey covering the King Island site originally acquired by Ovation Data was purchased from PacSeis Inc. The full survey covered an area of 58km by 27km, and the sub-grid purchased by LBNL is the 7.5km by 5.5km centered on the CG1 well as previously shown.

The first stage of analysis was time-to-depth conversion. Ideally, this would have employed seismic velocities from sonic logs in multiple wells and at least one VSP. Multiple logs enable interpolation of velocities between wells, while VSPs are used to correct for the usual mismatch between sonic velocities measured at high frequencies and the velocities of lower frequency waves recorded by surface seismic surveys. However, only the sonic logs from the CG1 well were available, and no VSP had been carried out.

Figure 5 shows a 2D cross section through the 3D seismic data volume in both its native coordinates (in-line, cross-line, time in milliseconds) and after time-to-depth conversion (in-line, cross-line, depth in feet). The distortion in the converted data inevitably increases with distance from the CG1 well owing to the lack of constraint on spatial variations in velocity. In general, this probably represents a worst-case scenario in that a high-resolution VSP survey would usually be carried out at a GCS site, even though it is likely that only one or two characterization wells would

be drilled. Examples of intersecting horizontal and vertical slices through the 3D depth-converted volume are shown in Figure 6.

Seismic horizons were next identified and digitized. The horizons were identified by matching them with lithological interfaces identified in borehole logs. Once a reflector had been identified it was 'picked' throughout the rest of the seismic volume. An example of the horizon assignments is shown on the 2D depth-converted seismic section in Figure 7.

Figure 5: 2D Slices Through the 3D Seismic Volume Showing Reflection Amplitude
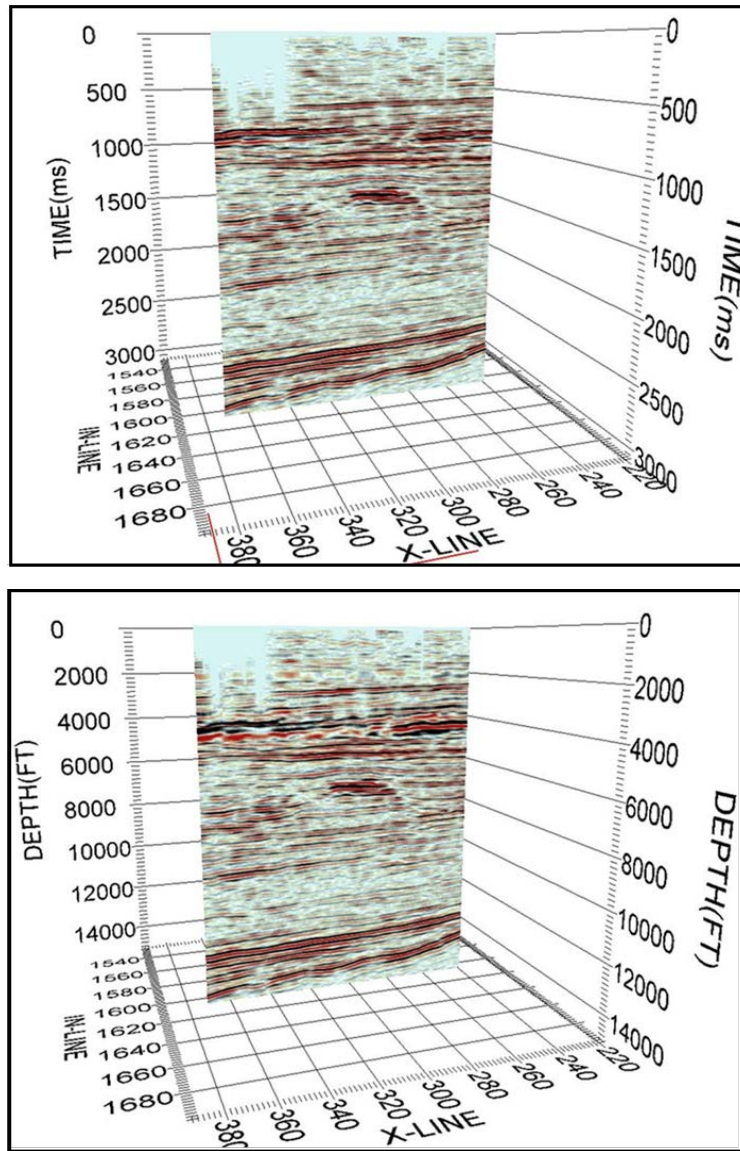
Two-way travel time (top) and depth (right) coordinates. Both displays show large positive and negative amplitudes as red and black, respectively.

3.2.4: Fault Identification

Faults were not readily apparent as spatially continuous sets of offset horizons within the King Island seismic amplitude volume, and detailed attribute analysis was beyond the scope of the

project. However, a prominent anticlinal feature was identified, which, can be seen, for example, to the left of center in Figure.7 extending from the bottom of the section (7,000 feet within the Starkey formation) to about 5,500 feet within the Mokelumne River Sandstone. To provide flow boundaries and the earthquake sources needed in the hydrological model and induced seismicity simulations, it was therefore postulated, not unreasonably, that the anticline would be bounded by steeply-dipping faults. Offset horizons and decreased reflector amplitudes seen on Figure 7 near the flanks of the anticline provide some evidence to support the existence of these hypothesized faults. The fault geometries interpreted from these features are shown as green lines on Figure 7, and the schematic fault locations were traced through the volume by making similar picks on other 2D seismic sections. The picks, plotted within the 3D volume on the right of Figure 6, only roughly define planar features, but are used to define the faults used in the flow modeling and seismicity simulations discussed in Chapters 4, 5 and 6.

Figure 6: Intersecting 2D Cross Sections Through the Depth-Converted Seismic Volume
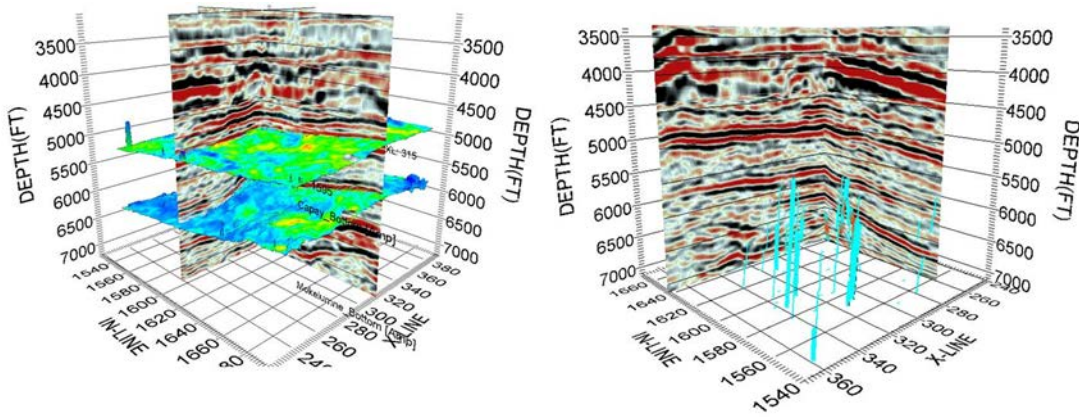
Horizon amplitudes (left) plotted using a blue to green scale, and fault picks (right) shown as steeply dipping cyan lines.

Figure 7: 2D Cross-Section Through the Depth Converted 3D Seismic Volume

23
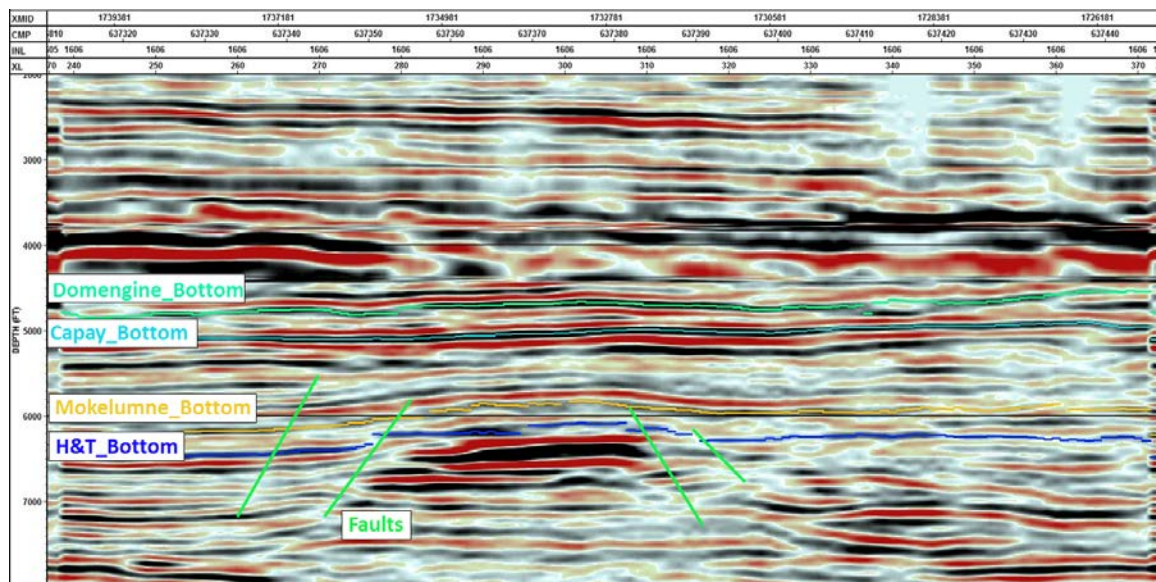
Labeled horizons: Domengine (green); Capay (cyan); Mokelumne River (yellow); H&T Shale (blue). The geometries of hypothesized steeply dipping faults suggested by horizon offsets and amplitude variations are shown as green lines.

3.3: Seismic Velocity, Attenuation and Rock Property Models

In addition to time-depth conversion of the surface 3D seismic data, seismic P- and S-wave velocities (denoted as V_p and V_s, respectively) are needed for several other purposes. The first of these is to derive models of rock density and elastic properties as functions of depth. Density-depth profiles are used directly to derive lithostatic stress profiles as part of the characterization of the in-situ stress state described in Section 3.4. Estimates of elastic moduli are required as inputs to the physics-based earthquake simulations described in Section 6.2. The second purpose is to derive the seismic Green's functions used, along with P- and S-wave attenuation models, to calculate earthquake ground motions for seismic hazard assessments, as described in Section 6.3. The depth range of interest for all of these purposes is from the ground surface to 6 km.

3.3.1: Velocity and Attenuation Models

V_p and V_s data for King Island are available from several sources, although none of these provides high-resolution site-specific data for the entire depth range of interest. The sonic logs from CG1 sample P- and S-wave velocities in the immediate vicinity of the well from 1,077 to 2,309 m depth and, for purposes of this study, each can be represented by a linear fit, as shown in Figure 3.8. The slope of the V_s fit is identical to the gradient between the surface and 1,200 m depth of a shallow S-velocity model derived for the Sacramento-San Joaquin Delta by Fletcher and Boatwright (2013), and the V_s values are in close agreement where the two models overlap between depths of 1,100 and 1,200 m.

Figure 8: Citizen Green #1 Well P- and S-Wave Velocity Logs
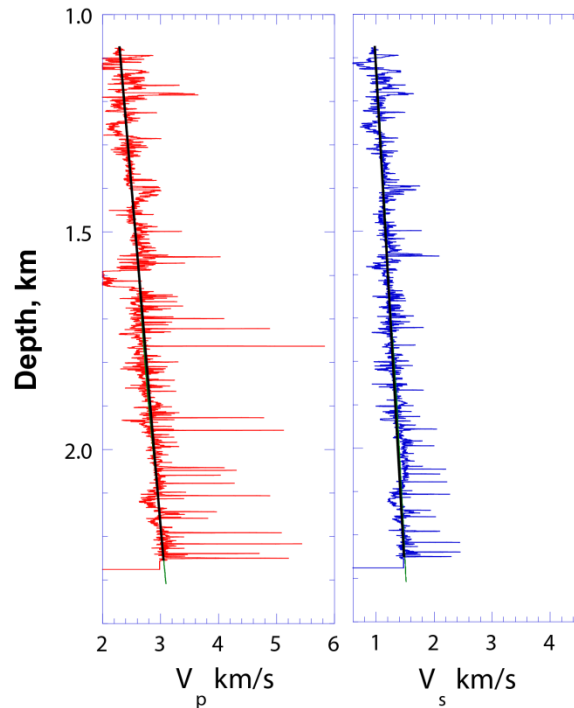
The black lines are linear fits to the velocities.

No model is available to constrain velocities under King Island between 2 and 6 km depth directly with adequate resolution. The best data available are three regional-scale seismic refraction profiles (maximum shot-receiver offset 160 km) shot along the axis of the San Joaquin Valley by the U.S. Geological Survey (USGS) in 1982 (Murphy, 1990). Two-dimensional models along the western and central profiles were published by Colburn and Mooney (1986) and Holbrook and Mooney (1987), respectively. Both of these profiles extend down to the mantle, but end about 30 km south of CG1. However, it was assumed that the Holbrook and Mooney velocity model below 2 km at the northwestern end of the central profile is generally representative of the structure towards the center of the basin and hence under King Island. The third, eastern profile extended to the northeast of King Island, but a published interpretation of these data could not be found.

Teel (2012) carried out joint inversion of earthquake travel times and gravity data to derive a regional-scale V_p model over a region of northern California that includes the Sacramento-San Joaquin Delta and King-Island. The spatial resolution of this model as it is published is too coarse to be of use at the scale required, but velocities below 4 km are in general agreement with the refraction models.

The final composite 1D V_p model for King Island shown in Figure 9 adopts the Holbrook and Mooney (1987) profile at its northwestern end below 3.7 km depth. Over the depth range of the CG1 sonic logs, the Holbrook and Mooney model diverges from the log V_p velocities, being about 0.2 km/s and 0.4 km/s faster at 1,077 and 2,309 m depth, respectively. The very close fit of the CG1 S-wave velocities to the Fletcher and Boatwright (2013) model suggests that the sonic logs provide good estimates of the seismic velocities at King Island above 2 km. Therefore, the slope of

the Holbrook and Mooney (1987) profile from the surface to 3.7 km was adjusted to match the CG1 V_p log.

Figure 9: King Island P- and S-Wave Velocity and Density Models
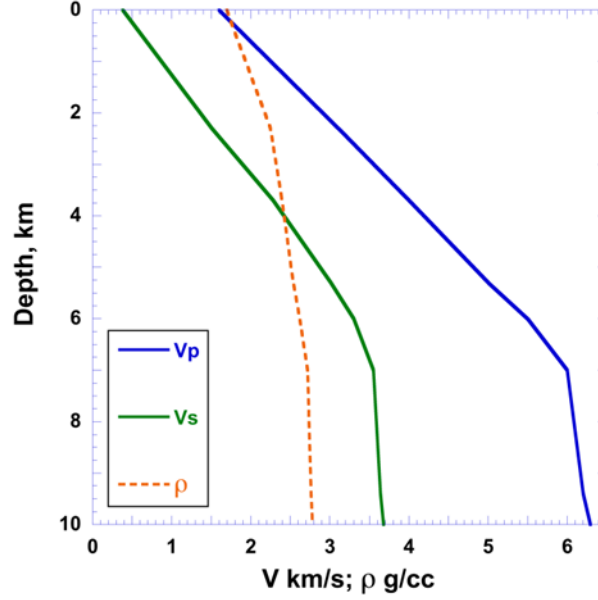
The relationship empirically determined for California sedimentary rocks by Brocher (2008) was used to calculate V_s from V_p to construct the 1D V_s model below 2,309 m. It can be seen on Figure 3.9 that this matches the shallower velocities almost perfectly.

The P- and S-wave attenuation (Q_p, Q_s) models for King Island given in Table 2 were estimated from the 3D attenuation model of (Eberhart-Phillips et al., 2014).

Table 2: King Island Attenuation Model

Depth, km	Q_p	Q_s
1	20	20
4	50	50
8	150	250

3.3.2: Density and Elastic Moduli

The empirical relationship from Ludwig et al. (1970) adopted for California by Brocher (2005) was used to calculate density from V_p. The density profile is shown in Figure 9.

Neglecting poroelastic effects, the elastic properties of an homogeneous isotropic medium are completely described by a combination of any two elastic parameters, which can be calculated from V_p, V_s and density, ρ. The earthquake simulation code RSQSim used for the seismicity simulations described in Section 6.3 requires the Lamé parameter λ and shear modulus μ as input, which are calculated from the depth-dependent velocities and density as $\lambda(z) = \rho(V_p^2 - 2V_s^2)$; $\mu(z) = \rho V_s^2$.

26

3.4: In situ Stress

Geomechanical simulations of seismicity require estimates of the background in situ tectonic stress state in the crust as a function of depth. This state is described by the orientations and magnitudes of three orthogonal principal stresses, which, assuming that the axis of one principal stress is vertical, are the vertical stress (S_V), and the maximum, (S_H) and minimum (S_h) horizontal stresses. These are then used to calculate the shear and normal stresses resolved on earthquake source faults having given geometries (strike and dip) (Jaeger et al., 2007, Chap. 14), as described in Section 6.3.

S_V at a particular depth h is assumed to be the lithostatic stress, and is calculated from the integrated density ρ of the overburden rock as $S_V = \rho g h$, where g is the acceleration due to gravity. The horizontal principal stresses would in general be estimated from site-specific measurements as part of a comprehensive characterization of a GCS site, together with existing data from nearby locations within the same tectonic regime. Stress measurement techniques include observations of borehole breakouts and drilling-induced fractures to estimate S_H orientation (Zoback et al., 1985), mini-hydrofracturing and leak-off tests to estimate S_H orientation, S_h magnitude and fracture gradient (Rummel, 1987; Amadei and Stephansson, 1997). Principal stress orientations can also be inferred from individual earthquake focal mechanisms and from inversions of ensembles of focal mechanisms on a regional scale (Gephart and Forsyth, 1984; Michael, 1987), although these methods are based on assumptions that make them inherently less reliable.

The stress state at King Island is very poorly constrained. Stress measurements were not performed in the CG1 well or, to the authors' knowledge, in other nearby wells. Therefore, stress orientations were taken from the World Stress Map (WSM) database (Heidbach et al., 2008), which is a worldwide compilation of stress measurements. The closest data to King Island are S_H directions of 049±21° from borehole breakouts at depths of 2,500-2,800 m in a well 3.1 km to the west-northwest (WSM reference USA 348), and 062±15° at 1,600-2,500 m in a well 9.9 km to the north-northwest (USA 352). The measurement from the nearest well was adopted as the best estimate for King Island. The density gradient given in Figure 3.9 yields a linear S_V gradient of 21.58 MPa/km at King Island (anchored at zero at the ground surface). No estimates of horizontal stress magnitudes are available from the local WSM data.

In general, the tectonic regime, or style of fault displacement, places a constraint on the relative magnitudes, or ordering, of the principal stresses (e.g. Zoback, 1992). For example, a strike-slip regime implies that $S_H > S_V > S_h$, while reverse faulting implies $S_H > S_h > S_V$. Unfortunately, the tectonic regime at King Island is unknown. Based on GPS data, Prescott et al. (2001) showed that there is a transition across the eastern front of the Coast Ranges from the predominant dextral strike-slip regime of the San Andreas fault system on the west to reverse or oblique reverse-right lateral at the margin of the Central Valley. This is consistent with reverse displacement on the north-striking Midland fault, 20 km west of King Island, interpreted by Unruh and Hitchcock (2009). These authors also suggested a dextral slip component on the fault, but were unable to confirm it. Chanchani et al. (2003) estimated that the virgin state of

stress at the Buena Vista Hills oilfield - located in the southern San Joaquin Valley but at roughly the same distance from the western valley margin as King Island – was

$$S_H \geq 54, \quad S_V = 25, \quad S_h = 26 \text{ MPa},$$

at 1,300 m depth; i.e., $S_H > S_V \approx S_h$, which corresponds to a reverse-oblique slip regime, with $S_H \gtrsim 2S_V$.

It has not been shown whether or not the regime at the Midland fault extends further east under the Valley, but in the absence of better information it was assumed that it does. The faulting regime at King Island was assumed to be reverse-dextral oblique; this is consistent with the 049° S_H direction relative to the strikes of the faults at King Island (Section 5.1.3), which imply a dextral component of slip on both faults. In the absence of other data, a reverse-oblique stress state modeled on Chanchani et al. (2003) was adopted. The model is anchored to the S_V gradient at King Island, with $S_H = 1.8S_V$ and $S_h = 1.2S_V$. Therefore, the linear gradients in S_H, S_V, and S_h gradients are 38.7, 21.5 25.8, respectively.

CHAPTER 4:
Hydrological Flow Modeling Of King Island CO_2 Injection

4.1: King Island Permeability Model and Injection Scenarios

At depths below about 800 m injected gaseous CO_2 changes to a supercritical fluid. This has the favorable properties of the low viscosity of a gas phase, which promotes injection, along with the high density of a liquid phase, which promotes efficient use of pore space capacity. Some CO_2 also dissolves into the aqueous phase, which increases brine density, and the resulting downward convection of CO_2-laden brine promotes security of the stored CO_2.

In the present study, hypothetical CO_2 injection and storage scenarios are numerically modeled, based on the actual geological and hydrogeologic setting at King Island. The target formation for injection is the Mokelumne River Sandstone (see Figure 3.2), a depleted natural gas reservoir. Two sub-vertical faults loosely based on picks in the 3D seismic volume extend through that formation and extend down to the bottom of the sedimentary sequence. The transient pore pressure response to CO_2 injection and storage is monitored at all points on the faults, and is used as input to the physics-based simulations of induced seismicity described in Section 6.3.

4.1.1: Numerical Simulator

The TOUGH2 numerical simulator (Pruess, 2004; Pruess et al., 2012) for multi-phase, multi-component fluid flow and heat transfer in porous or fractured media is used for the present problem, with the equation of state (EOS) package ECO2N V2.0 (Pan et al., 2016) for H_2O, NaCl, and CO_2. Fluid flow is modeled using a multi-phase extension to Darcy's law, with inter-phase effects controlled by capillary pressure and relative permeability functions. Spatial discretization is done with the integral finite difference method (Narasimhan and Witherspoon, 1976), which enables a flexible representation of relevant hydrogeologic features. Time-stepping is fully implicit, with Newton-Raphson iteration employed to linearize the problem. TOUGH2 has been widely used over the past 15 years to study GCS, including scoping and design studies, code comparisons, and analysis of laboratory and field data (Doughty and Myer, 2009; Birkholzer et al., 2012; Pruess et al., 2004; Doughty et al., 2008). ECO2N V2.0 is a recent update that extends the upper temperature limit from about 100°C to about 300°C. The higher temperature is required by the large depths to which the present model extends, but temperature changes accompanying CO_2 injection are not considered in the present study.

4.1.2: Geologic Model

TOUGH2 model development began with a regional geologic model of the sedimentary layers of the Sacramento Valley in the vicinity of King Island obtained from Jeff Wagoner of LLNL (Figure 10). The target for CO_2 injection is the high-permeability Mokelumne River Sandstone, whose top

is at a depth of about 1,400 m at King Island, and which is about 480 m thick. The Mokelumne River Sandstone is over- and underlain by extensive low-permeability layers, the Capay Shale and the Starkey Shale, respectively. Two local sub-vertical faults were added to the TOUGH2 model, loosely based on schematic picks on a 3D seismic survey as described in Section 3.2.5. They do not represent actual faults at King Island, but do represent faults that might be typically associated with the type of anticlinal structure observed in the Mokelumne River Sandstone in the seismic data. The TOUGH2 model extends from the top of the Mokelumne River Sandstone down to about 5,400 m, the approximate base of the sedimentary sequence. Formations below the Mokelumne River Sandstone are predominantly of low permeability, and fluid flow is mainly limited to the faults.

Figure 10: Geologic Model of the Southern Sacramento Valley Region Surrounding King Island
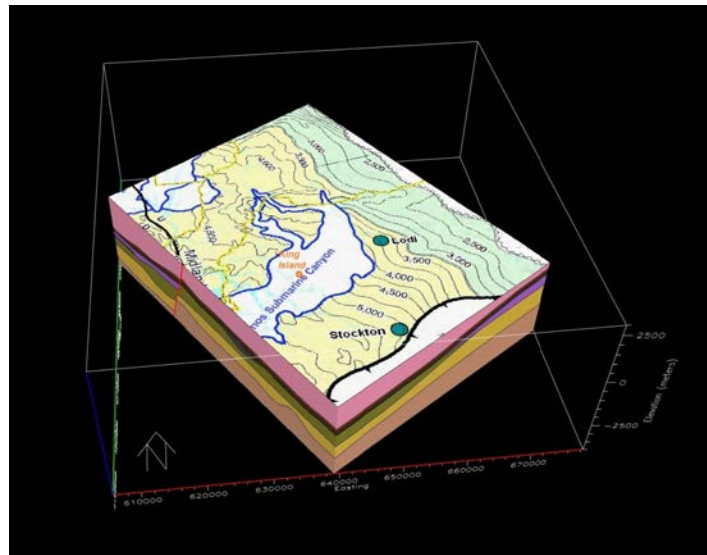
The Mokelumne River Sandstone is the light brown layer underlying the Capay Shale (dark brown) and overlying the Starkey Shale (gold).

4.1.3: Numerical Grid

The geologic model indicates that in the vicinity of King Island, the Mokelumne River Sandstone has nearly constant thickness, with a relatively uniform dip of 1.6°, up to the ENE. Therefore the numerical grid was designed as a three-dimensional (3D) rectangular grid with the +x direction being east, the +y direction being north and the +z direction being up. The model was then rotated 30° counter-clockwise about the z-axis to align the x-axis with the dip direction, and then tilted about the y-axis so that the layers are dipping up to the ENE at 1.6°.

Three of the four lateral boundaries are closed to represent regional faults or formation termination. In the +x direction, the model has a distant, constant-pressure boundary, to represent the surface outcrop of the Mokelumne River Sandstone (Figure 11).

Figure 11: Location Map for the King Island Model with Lateral Boundary Conditions
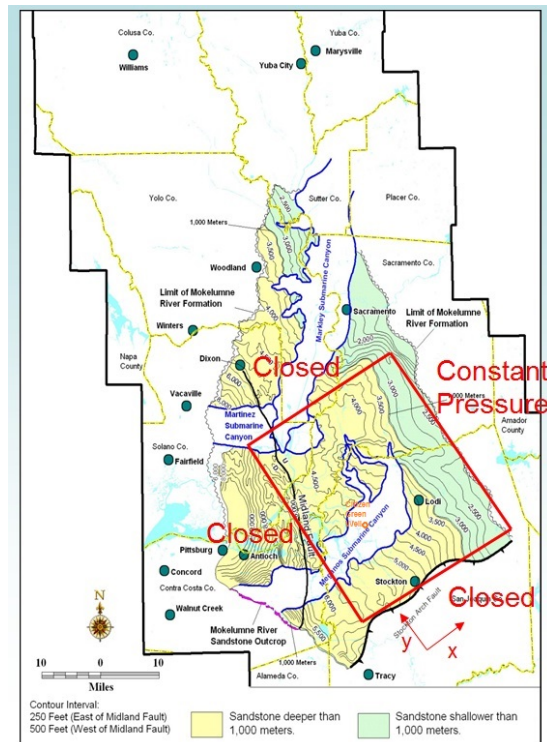
The lower boundary of the model represents the base of the sedimentary sequence and is a no-flow boundary. The top boundary is primarily the caprock of the Mokelumne River Sandstone, the Capay shale, which is modeled as a no-flow boundary. In some places, the Capay shale and upper portion of the Mokelumne River Sandstone were eroded by the Meganos Gorge, which is composed of low-permeability gouge material, making it a de facto extension of the caprock downward. Hence, the upper boundary of the permeable thickness of the Mokelumne River Sandstone is undulating. A simplified representation of the gouge is implemented in some versions of the TOUGH2 model to enable potential trapping of buoyant gases, including CO_2 and CH_4, to be simulated, as discussed in Chapter 5.

Faults and gouge are added to the model in a simple way. The basic rectangular grid is not altered, but the faults and gouge structures are represented mathematically by planar sections using the same (x,y,z) coordinate system as the rectangular grid. Then one can sweep through the grid, and assign fault or gouge properties to any grid block whose (x,y,z) coordinates coincide with those of the fault or gouge structures.

Typically for modeling CO_2 injection, lateral grid spacing is relatively fine for the areal region where the CO_2 plume is expected to go, then becomes gradually coarser farther away to model the pressure response to injection, which extends much farther than the CO_2 itself. When that approach was used with a fine-grid spacing of 50 m, the representation of the local faults, which extend beyond the fine region of the grid, was poor (Figure 11, left). Therefore, an alternative approach was taken, whereby the lateral grid resolution is 50 m at the injection well, and begins coarsening immediately as one moves away from the well. The coarsening is gradual enough so

31

that the CO_2 plume and the faults are well resolved (Figure 11, right). The fault on the right was also simplified to have a planar structure, rather than being the combination of two intersecting planes implied by the seismic picks, as described in Chapter 5 below. Beyond the faults, the rate of coarsening increases. In all, there are 2,862 grid blocks per layer, and the areal extent of the model is 99 km by 83 km. Figure 12 shows a 3D perspective view of the grid, highlighting the faults, and Figure 13 shows only the grid blocks that represent the faults themselves. The faults to the west and east of the well are designated Faults A and B, respectively. These are the points for which the transient pressure response is provided to the geomechanical model for the induced seismicity simulations.

The model uses 19 layers to represent the Mokelumne River Sandstone and an additional 16 layers to represent the underlying sedimentary layers. In the Mokelumne River Sandstone, model layer thicknesses were chosen to best represent major variations in permeability. In the underlying portion of the model, layer thickness gradually increases with depth, as shown in Figure 12.

Figure 11: Plan View of the Central Portion of the Model
(Two Local Sub-vertical Faults)
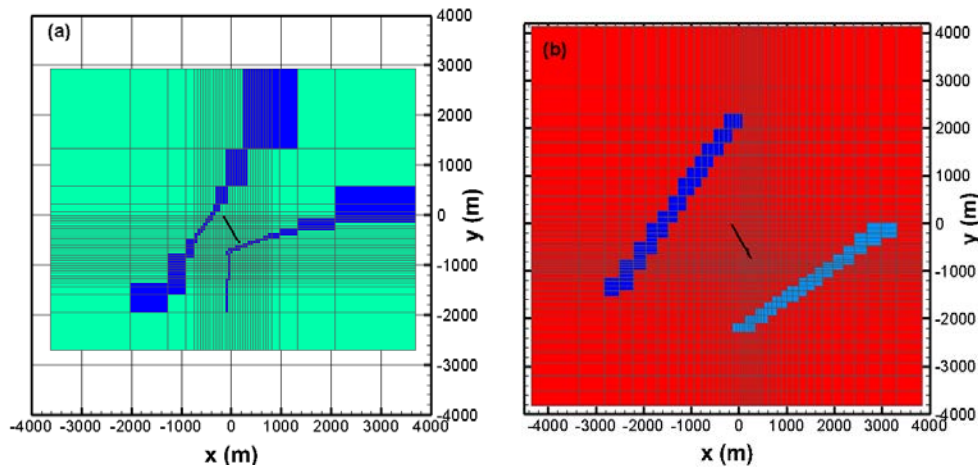
Original grid (left) with uniform spacing near the injection well, and doubling grid spacing beyond that; grid with gradually increasing spacing (right). The black line shows the trace of the CG1 well. The faults to the west (left) and east of the well are designated Faults A and B, respectively.

**Figure 12: 3D Perspective View of the Central Portion
of the Model (Sub-vertical Faults A and B)**
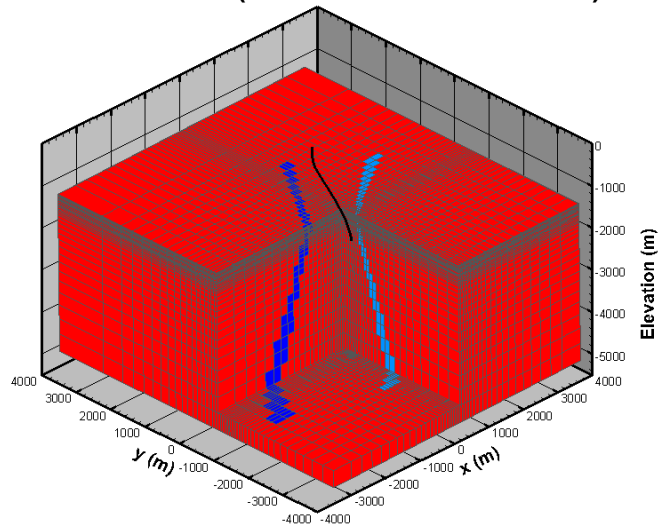
The black line shows the trace of the CG1 well.

Figure 13: Grid Blocks Representing the Faults
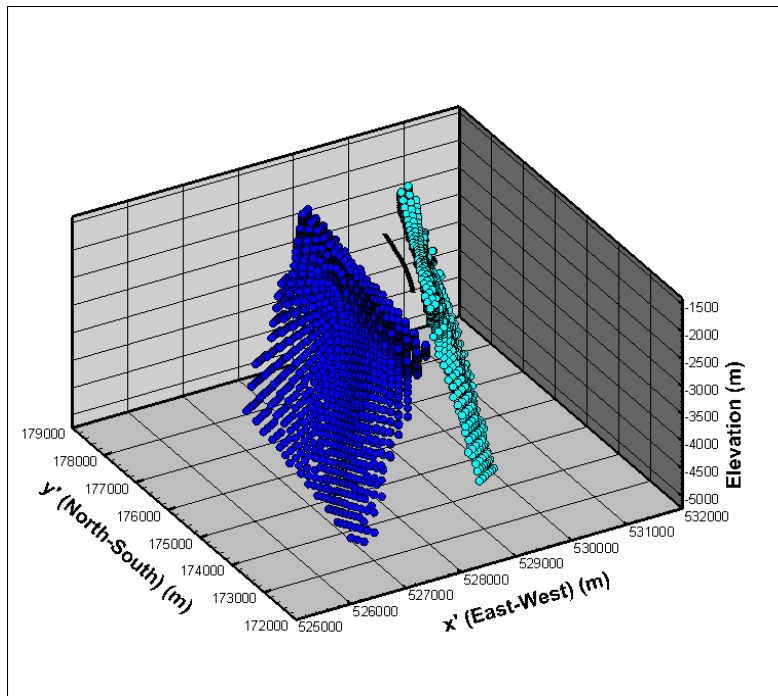
The trajectory of the CG1 well is shown as a black curve. Note that the coordinate system has been rotated and translated back to a N-S, E-W system.

4.1.4: Flow Properties

The porosity and permeability of the Mokelumne River Sandstone are taken from the well logs and sidewall core measurements collected from the CG1 well described in Section 3.1. Figure 14 shows the well-log values of porosity and permeability along with averaged values used for the 19 model layers that represent the Mokelumne River Sandstone. TOUGH2 allows permeability to be anisotropic, and here the horizontal and vertical permeability of each model layer are taken to be the arithmetic and harmonic mean of the well-log values collected within that layer, respectively. This assignment is physically reasonable for flow through a sedimentary rock that moves radially out from a well and upward by buoyancy forces. Note that because the layers of the model are dipping to align with sedimentary bedding, so-called horizontal permeability is actually permeability parallel to bedding, and so-called vertical permeability is actually permeability perpendicular to bedding. As shown in Figure 14, horizontal permeability is generally at least an order of magnitude greater than vertical permeability. Permeabilities are generally larger in the upper half of the Mokelumne River Sandstone.

Figure 14: Porosity (*left*) and Permeability (*right*) from CG1 Well Logs
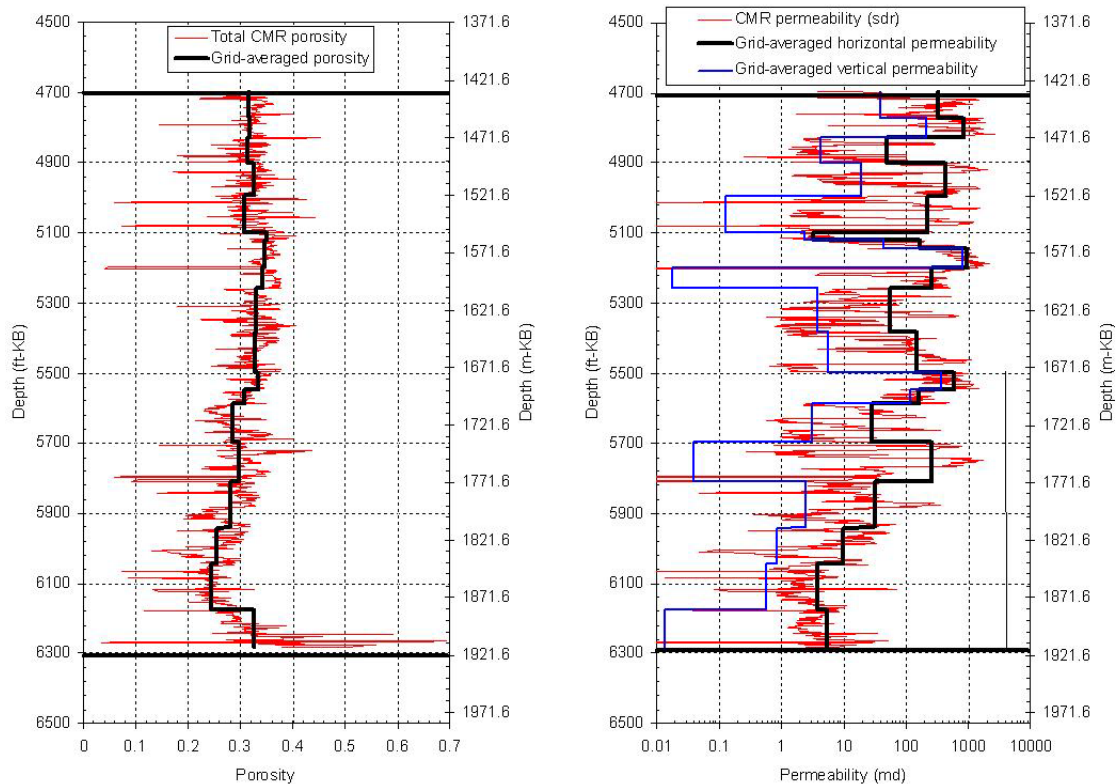
Includes average values assigned to model layers. The vertical bar on the right of the permeability plot shows the assumed perforated interval for CO$_2$ injection.

Actual values for fault properties are unknown, so a "sandwich" structure was hypothesized wherein the faults contain a low-permeability core composed of fault gouge flanked by higher permeability damage zones of fractured rock on either side. This structure implies that the faults

act as barriers to flow perpendicular to the fault plane, but a conduit for enhanced flow parallel to the fault plane. Such fault hydrology has been noted in a variety of geologic settings (Ijiri at al., 2009; Karasaki et al., 2015). As a starting point, the fault-core was assigned a permeability of 5 mD, which is small compared to the sediment permeabilities shown in Figure 4.6 but non-vanishing, and the fault-outer-conduit permeability was taken as 500 mD, which is comparable to the highest sediment permeabilities.

Because the grid is not finely enough resolved to represent the fault core and outer conduits with individual grid blocks, each fault grid block represents both components by making use of TOUGH2's anisotropic permeability provision. A special algorithm is used to assign permeability to fault grid blocks such that flow between two fault grid blocks uses the higher "horizontal" permeability value, and flow from a fault grid block to a non-fault grid block uses the lower "vertical" permeability value, regardless of whether flow is in the horizontal or vertical direction. Such an algorithm is necessary because of the "stair step" nature of the fault representation, which causes fault-fault connections to not always be vertical and fault/non-fault connections to not always be horizontal. The results from the algorithm were checked to confirm that appropriate permeability values have been assigned to the grid blocks.

Relative permeability and capillary pressure functions are generic van Genuchten (1980) functions, with shape factor m = 0.457, residual liquid saturation S_{lr} = 0.3, and residual gas saturation S_{gr} = 0.01. Although the CO_2 is supercritical, it is herein referred to as the gas phase, whereas brine is referred to as the aqueous or liquid phase.

4.2: Simulation Cases and Modeling Results

Initial conditions for all cases are a single-phase brine-saturated formation at hydrostatic pressure, with a geothermal temperature gradient. Salt mass fraction is uniform at 0.05 except for the immediate vicinity of the injection well. Here it is zero to reflect a hypothetical pre-flush operation conducted to minimize the potential for salt precipitation around the injection well, as water evaporates into the supercritical CO_2 phase (Pruess and Müller, 2009).

Supercritical CO_2 is injected into the model at a constant rate for 20 years, and then the evolution of the system under undisturbed conditions is modeled for the following 50 years. The injection interval is assumed to occur at the CG1 well through a perforated interval open over the lower half (239 m) of the Mokelumne River Sandstone (Figure 4.6). A wellbore model is not used; instead, the total injection rate is divided among the eight model layers representing the perforated interval in proportion to the permeability-thickness product of each layer. Using this algorithm, the majority of the injection occurs into the upper four layers, for an effective perforated thickness of 95 m.

4.2.1: Base Case

The base case considers constant injection for 20 years at a rate of 8 Mt/year (8 x 10^6 metric tons/year or 8 x 10^9 kg/year), then a rest period for 50 years. For simplicity, the low-permeability gouge that represents the Meganos Gorge is not included. This is not expected to impact the pressure response on the faults significantly, as the gouge is limited to the upper few layers of the

model whereas injection occurs in the lower half. Figure 4.7 shows the spatial distribution of CO_2 through a vertical cross-section of the model at several times during the injection period. There is strong preferential flow of CO_2 into the higher permeability layers of the Mokelumne River Sandstone, and within these layers there is strong upward buoyancy flow of CO_2. The lower permeability layers effectively act to decrease the overall vertical permeability of the formation itself, but the two faults provide paths for upward flow of CO_2.

Figure 15: Base Case CO_2 Distribution
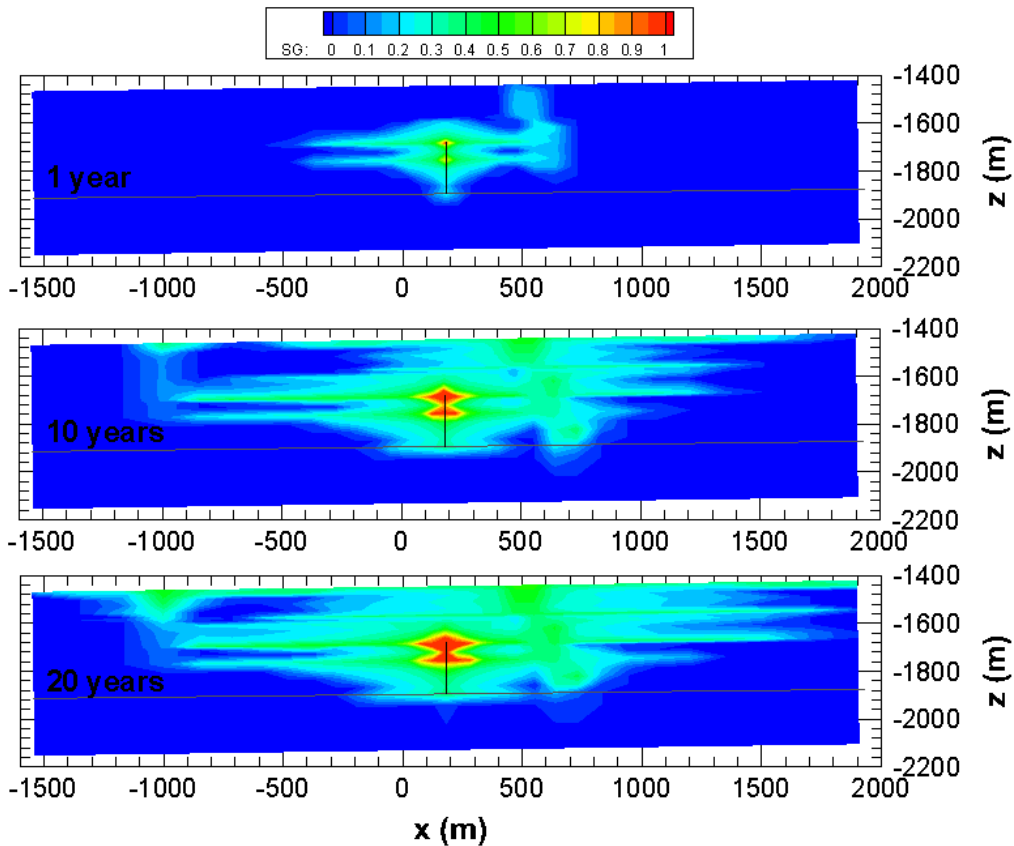
Base case is plotted as saturation of gas phase SG in a vertical cross-section through the injection well (black bar) at several times during the 20-year injection period. The lower limit of the Mokelumne River Sandstone is shown as a gray line.

Figure 16 shows the spatial distribution of the CO_2 and pressure change (that is, pressure minus initial, hydrostatic pressure) in two horizontal layers at the end of the injection period. The faults act to limit lateral flow and promote vertical flow of CO_2. Note that the pressure response extends far beyond the CO_2 plume itself.

Figure 16: Base Case CO$_2$ Distributions (color scale) and Pressure Change (contours).
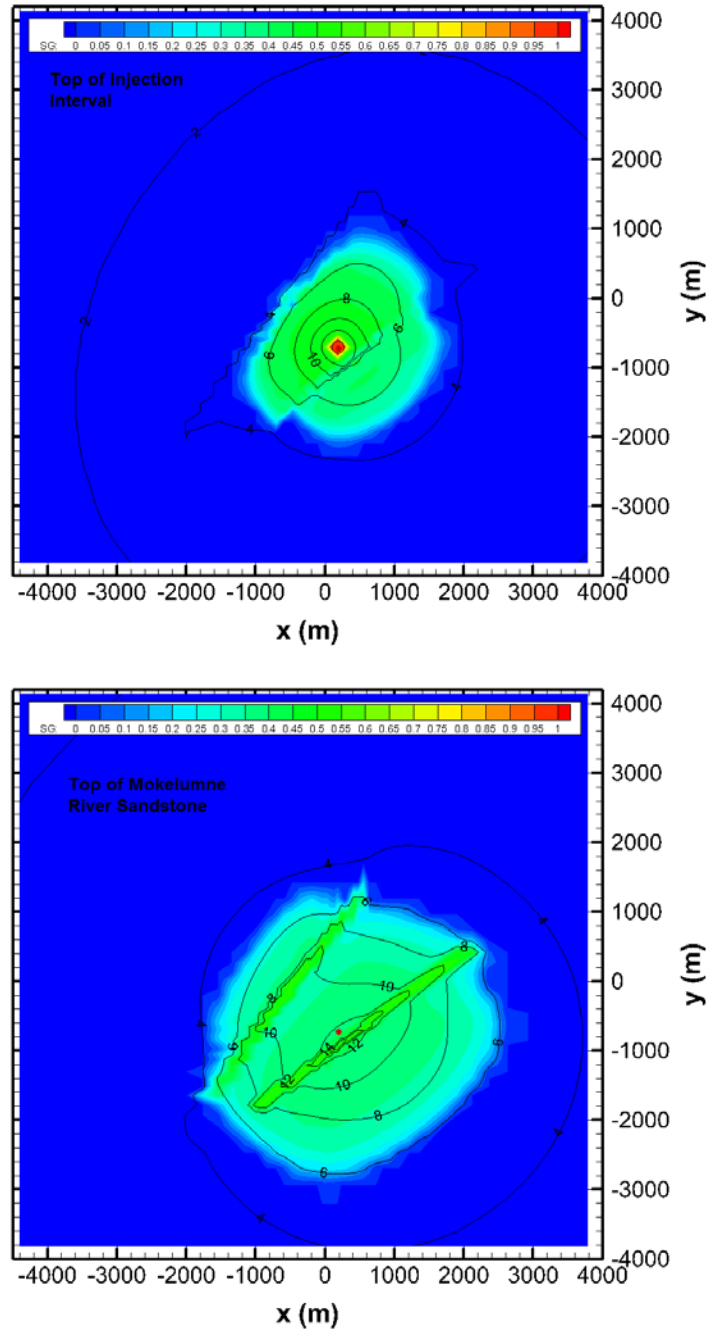
At the top of the injection interval (top) and the top of the model (bottom) at 20 years, the end of the injection period. The injection well is shown as a red dot. Pressure in bars (10 bar = 1 MPa).

Figure 17 shows the spatial distribution of CO$_2$ and pressure change in a perspective view of the model at the end of the injection period, illustrating the role the faults play in pressure propagation.

Figure 17: Base Case CO$_2$ Distributions and Pressure Change - 20 Years
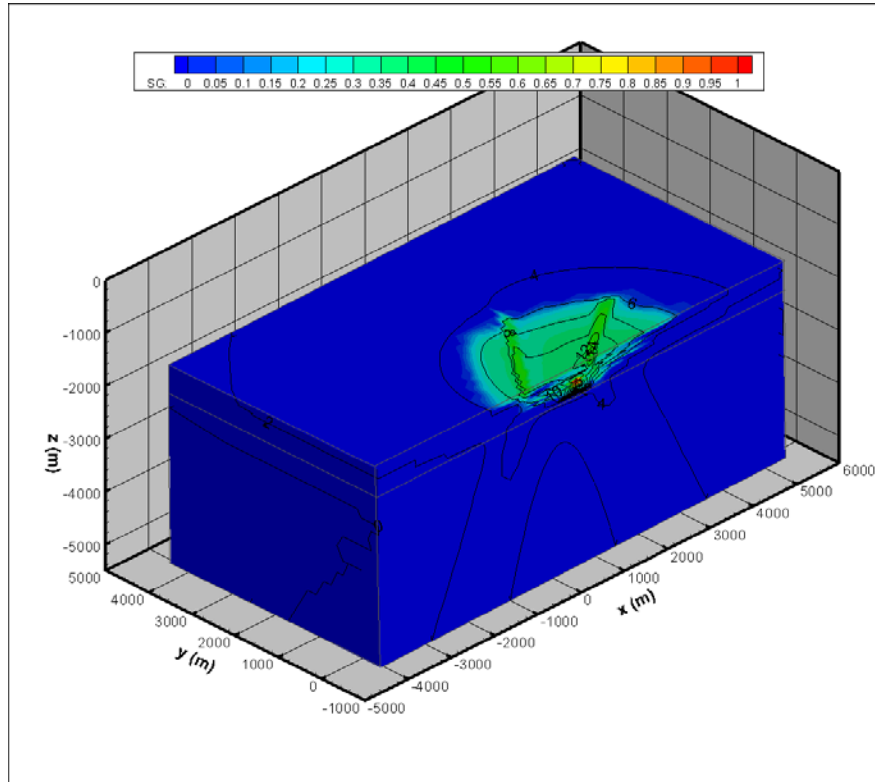
Twenty years is the end of the injection period, for a perspective view through the plane of the injection well.

Figure 18 shows the transient pressure response at the top of the injection interval and at one point on each fault, for illustrative purposes. The pressure at every point on the faults is recorded at roughly equal time intervals (every 30 days for the first 3 years of the injection and rest periods, and every 180 days thereafter). This is the information provided to the geomechanical model used to simulate induced seismicity. Note that the maximum pressure change occurs at about 2 years at the nearer Fault B and at about 7 years at the more distant Fault A, not at the end of the injection period. This is due to the lower viscosity of CO$_2$ compared to brine. As CO$_2$ fills more of the pore space, the effective viscosity of the system decreases, lessening the pressure buildup for a given injection rate. After injection ends at 20 years, pressure decreases rapidly as the pressure pulse continues to diffuse outwards.

Figure 18: Base Case Pressure Response to CO$_2$ Injection at Various Points
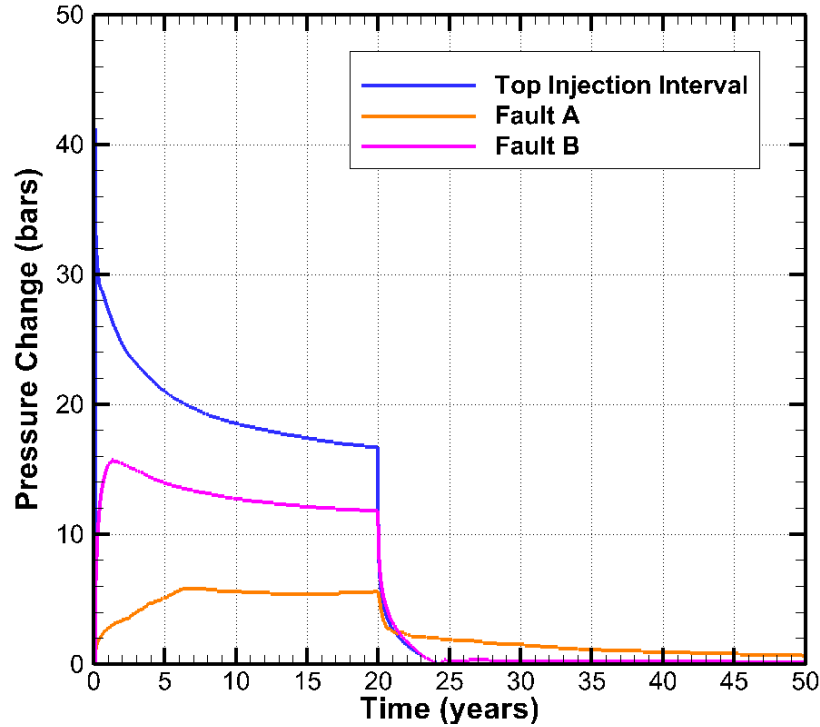
10 bars = 1 MPa.

4.2.2: Case A: Larger Injection Rate

Case A is just like the base case, except that injection rate is increased from 8 Mt/year to 12 Mt/year. Figure 19 shows the spatial distribution of CO$_2$ through a vertical cross-section of the model at several times during the injection period. Greater flow in the faults is apparent, compared to the base case. Figure 20 shows the spatial distribution of the CO$_2$ and pressure change in two horizontal layers at the end of the injection period. The overall pattern is similar to the base case, but the magnitudes of the pressure changes are all increased.

Figure 21 shows the spatial distribution of CO$_2$ and pressure change in a perspective view of the model at the end of the injection period, illustrating the role the faults play in pressure propagation. The overall pattern is similar to the base case, but the magnitudes of the pressure changes are all increased. Figure 22 shows the transient pressure response at the top of the injection interval and at one point on each fault. As expected, the pressure change is about 1.5 times that of the base case, roughly proportional to the increase in injection rate.

Figure 19: Case A CO$_2$ Distribution in a Vertical Cross-Section
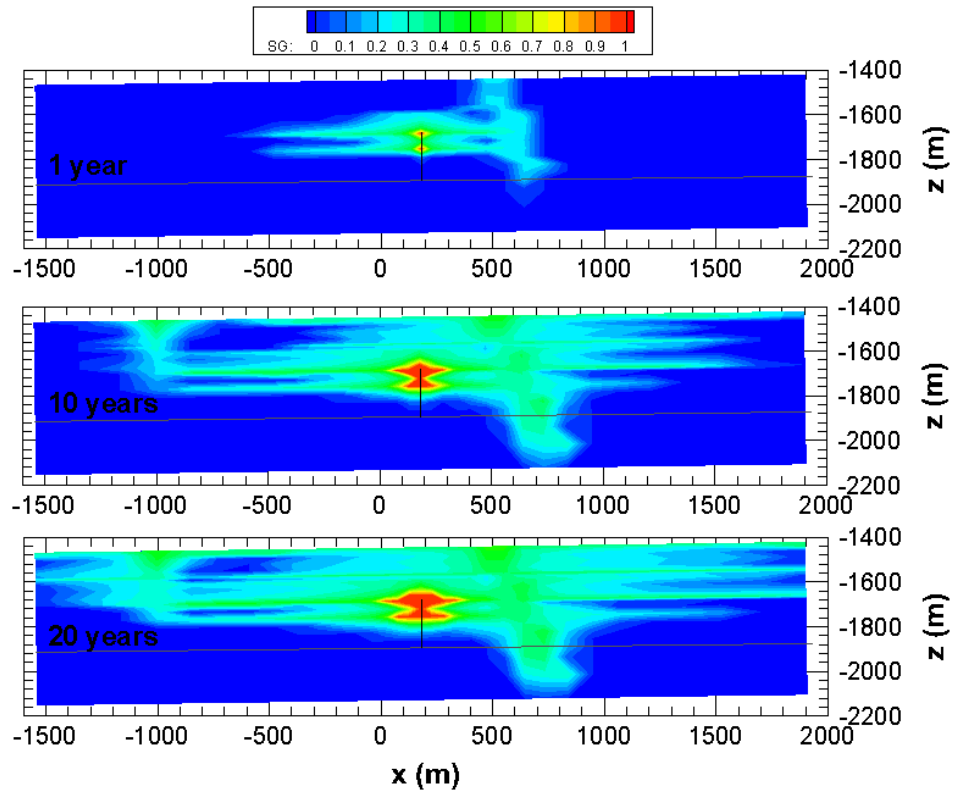
Through the injection well (black bar) at several times during the 20-year injection period. The lower limit of the Mokelumne River Sandstone is shown as a gray line.

Figure 20: Case A Distributions of CO$_2$ (color scale) and Pressure Change (contours)
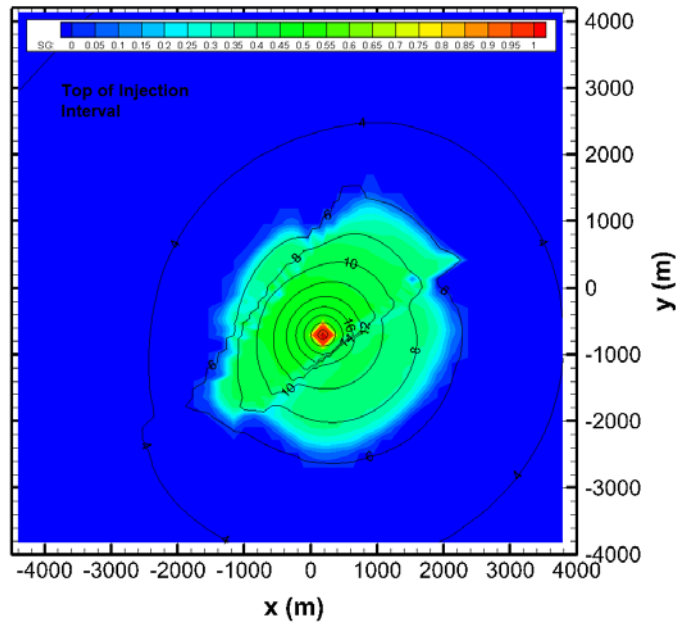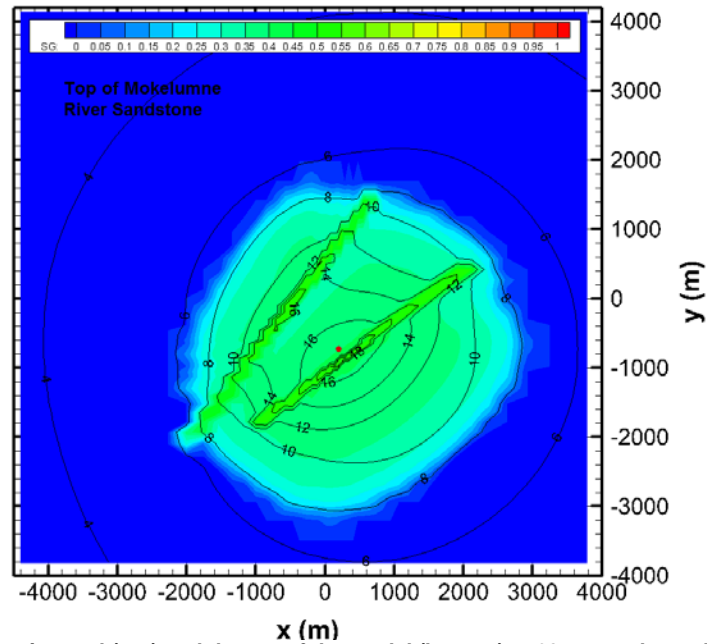
At the top of the injection interval (top) and the top of the model (bottom) at 20 years, the end of the injection period. The injection well is shown as a red dot. Pressure in bars (10 bar = 1 MPa).

Figure 21: Case A CO$_2$ Distributions and Pressure Change - 20 years
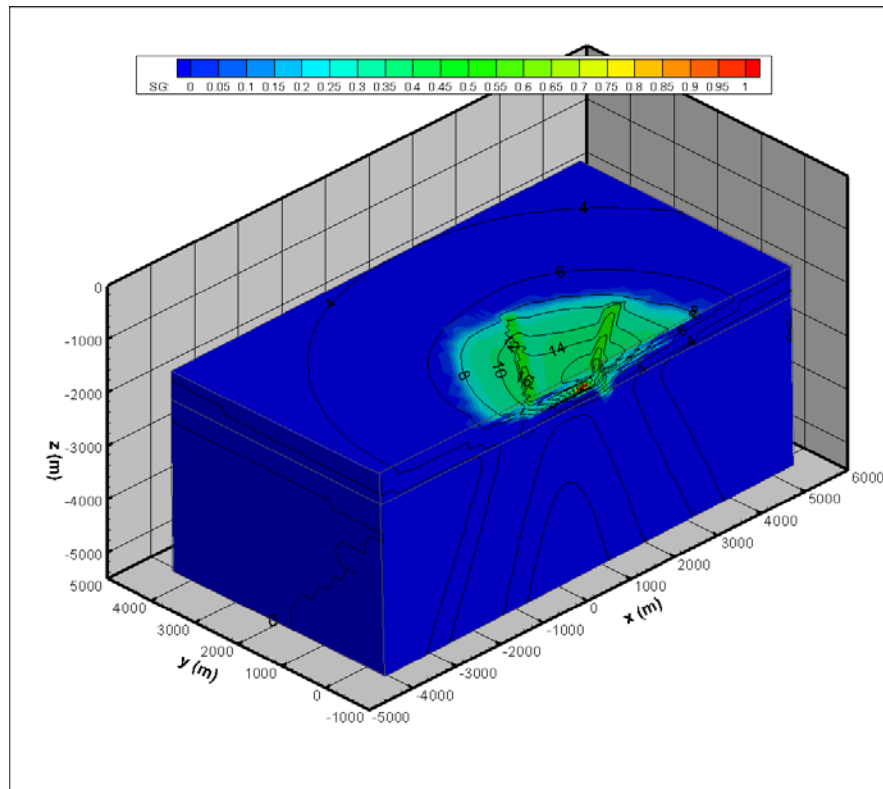
At the end of the injection period, for a perspective view through the plane of the injection well.

Figure 22: Case A Pressure Response to CO$_2$ Injection at Various Points

10 bars = 1 MPa.
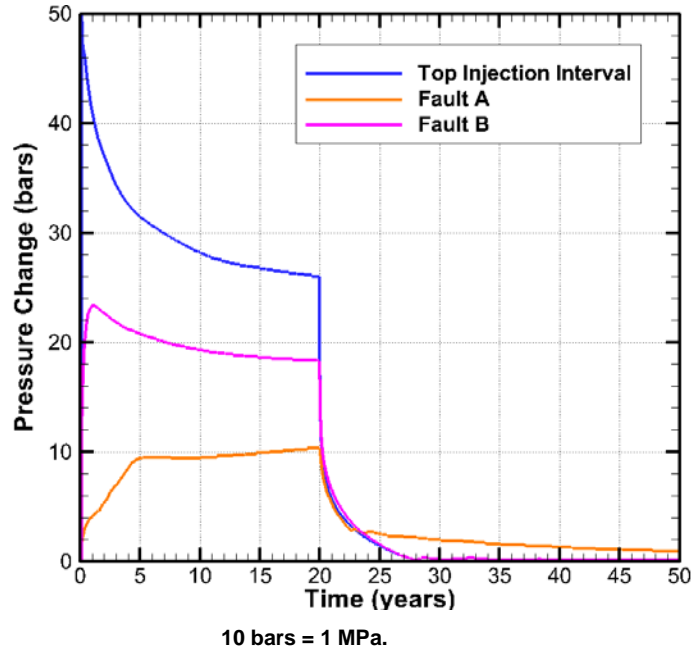
4.2.3: Case B: Lower Fault Permeability

Case B is just like the base case, except that the fault permeabilities (both fault-core and outer-fault-conduit) are decreased by a factor of 10. Figure 23 shows the spatial distribution of CO$_2$ through a vertical cross-section of the model at several times during the injection period. Much less spreading of CO$_2$ is apparent, both upward along the faults and radially away from the injection well, compared to the base case. Figure 24 shows the spatial distribution of the CO$_2$ and pressure change in two horizontal layers at the end of the injection period. The overall pattern is strikingly different from the base case, with much less lateral and vertical movement of CO$_2$. The pressure response is mainly within the region bounded by the faults, and it is much larger than for the base case.

Figure 25 shows the spatial distribution of CO$_2$ and pressure change in a perspective view of the model at the end of the injection period, illustrating the role the faults play in pressure propagation. The overall pattern is quite different from the base case, with large pressure increases concentrated on the parts of the faults near the injection interval. Figure 26 shows the transient pressure response at the top of the injection interval and at one point on each fault. The pressure responses are all larger and steadier than for the base case, and the pressure recovery after injection ends at 20 years is much slower.

42

Figure 23: Case B CO$_2$ Distribution in a Vertical Cross-Section Through the Injection Well (black bar)
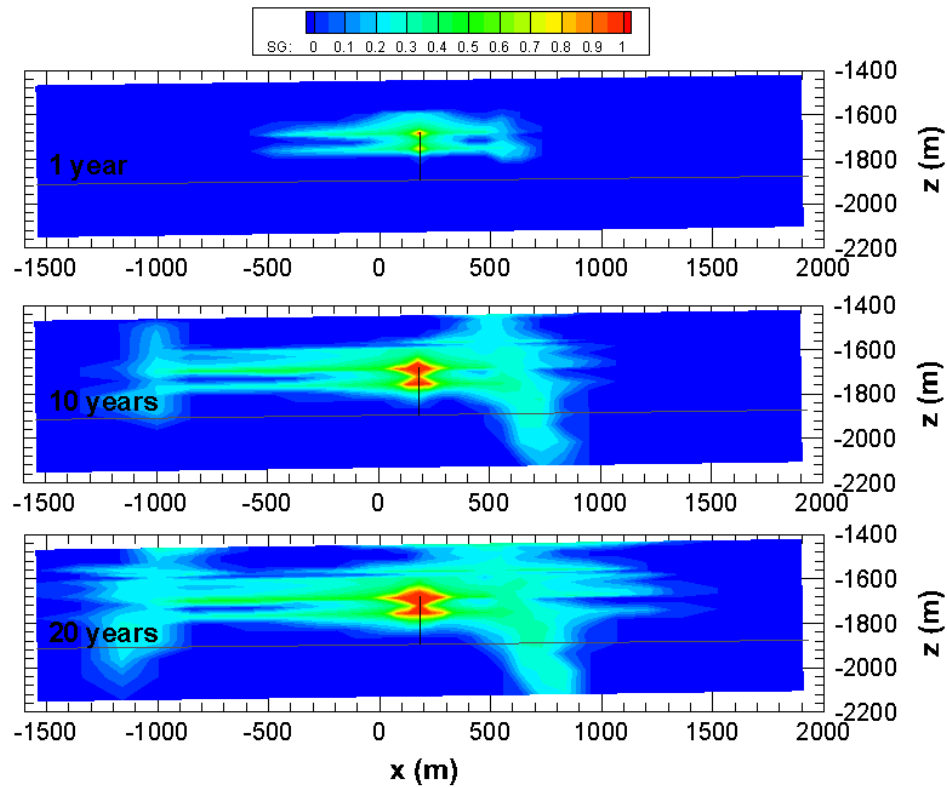
Injection several times during the 20-year injection period. The lower limit of the Mokelumne River Sandstone is shown as a gray line.

Figure 24: Case B of CO$_2$ Distributions (color scale) and Pressure Change (contours)
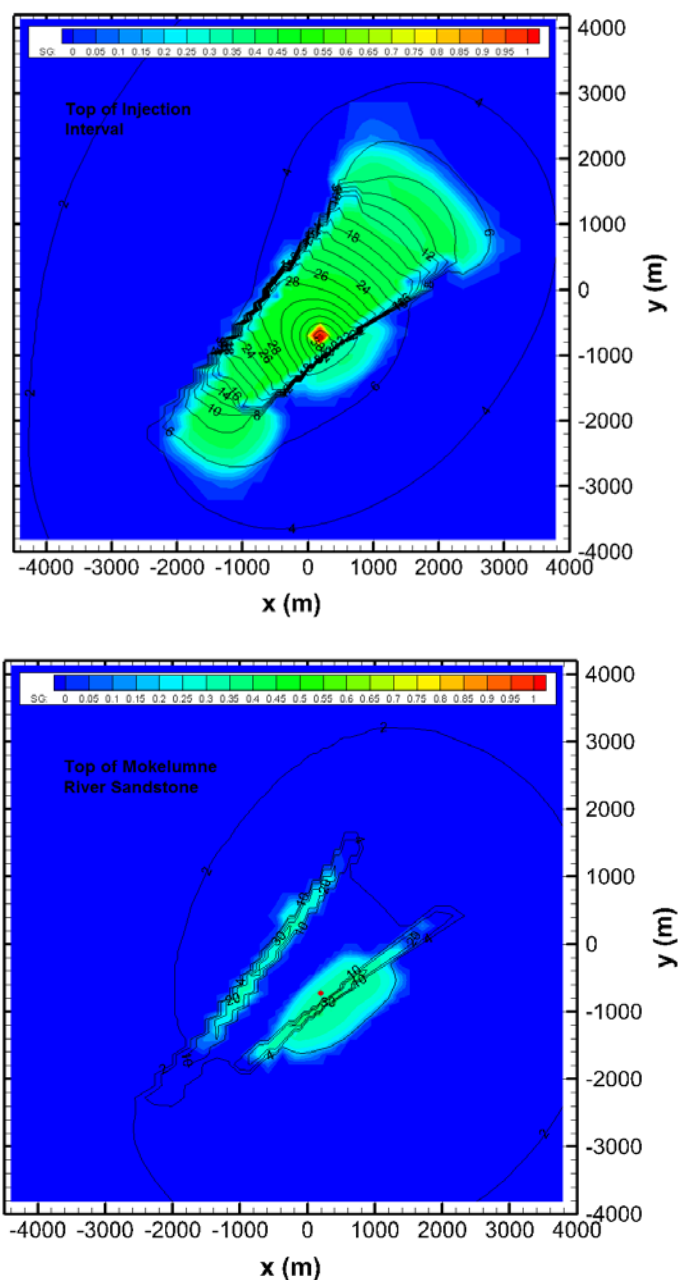
At the top of the injection interval (top) and the top of the model (bottom) at 20 years, the end of the injection period. The injection well is shown as a red dot. Pressure in bars (10 bar = 1 MPa).

Figure 25: Case B CO₂ Distributions and Pressure Change - 20 years
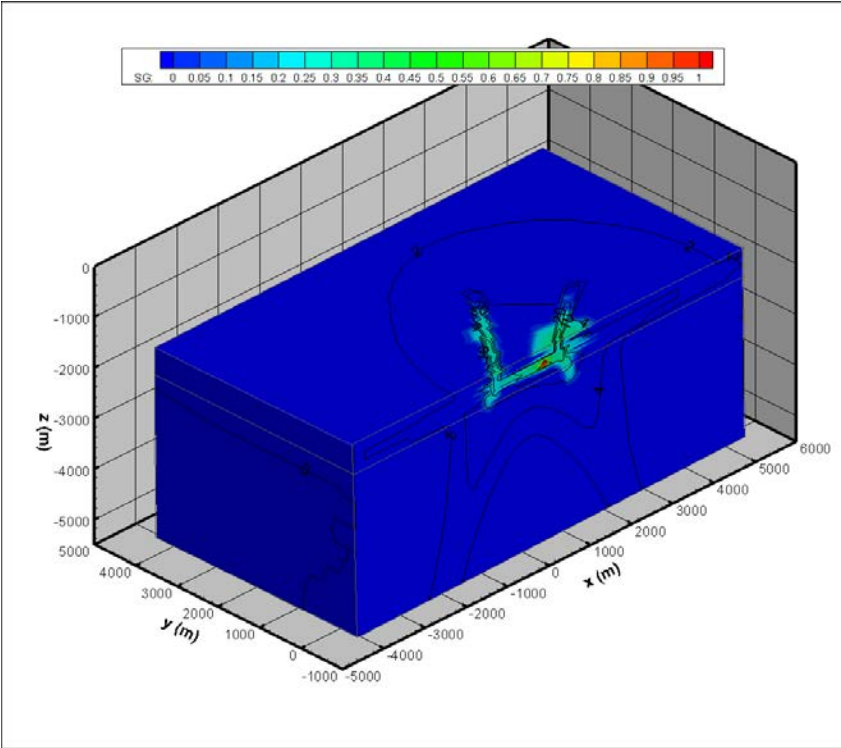
At the end of the injection period, for a perspective view through the plane of the injection well.

Figure 26: Case B Pressure Response to CO₂ Injection at Various Points

10 bars = 1 MPa.
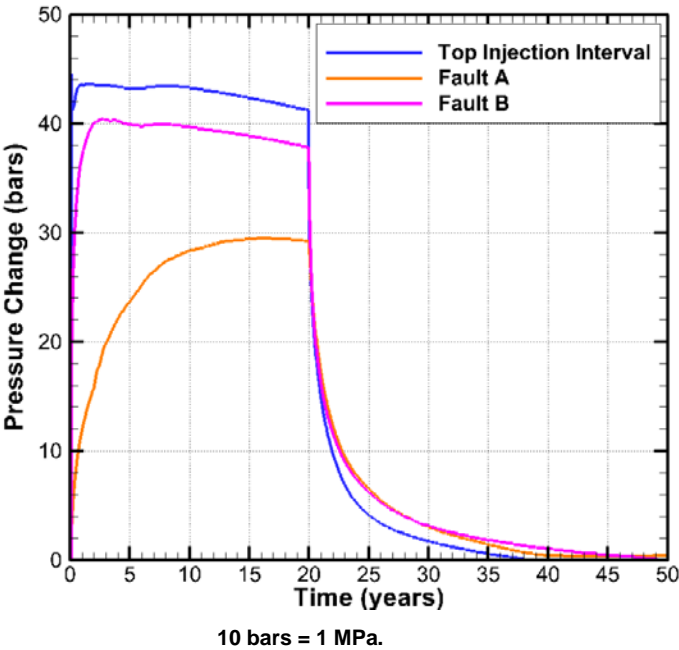
4.3: Discussion of Flow Modeling Results

A model of CO_2 injection into the Mokelumne River Sandstone at King Island was developed and used to predict the time-dependent pore pressure changes on local faults. The model includes the local geometry of the Mokelumne River formation, taken from a regional geologic model, and layering derived from well logs obtained from the CG1 well. Two faults are hypothesized, loosely based on picks taken from a 3D seismic survey. Simulations were done with two injection rates and a range of values for fault permeability. Increasing injection rate increased pressure change proportionately, with little effect on the overall pattern of CO_2 movement or pressure response. However, decreasing the fault permeability greatly impacted both the spatial distribution of CO_2 and pressure response and the magnitude of pressure response. The lower fault-core permeability meant that the faults acted as strong barriers to lateral spreading of CO_2, and the lower fault-outer-conduit permeability meant that the ability of the CO_2 to move upward by buoyancy flow through the faults was also curtailed.

Because fault permeabilities are generally very poorly known, their large impact signifies the importance of developing site characterization methods to learn more about their properties. Future studies will include the low-permeability gouge near the top of the model, but this is not expected to impact the pressure response in any major way. A more significant effect may be the use of hysteretic relative permeability functions, wherein the residual gas saturation is larger during the post-injection period, when brine begins to imbibe into pore space previously occupied by CO_2, than during the injection period, when the CO_2 plume is generally expanding in all directions. This larger residual gas saturation enables trapping of CO_2 and is generally accompanied by a slower pressure decline after injection ends.

CHAPTER 5:
The Effect of Residual Methane on Pressure Rise Due to Injection of CO₂ Into Depleted Gas Reservoirs

5.1: Introduction

Depleted natural gas reservoirs are believed to be promising for GCS by virtue of their capacity to store and produce gas (Oldenburg et al., 2001). Despite the normal meaning of "depleted," the fact is that depleted gas reservoirs can still contain significant amounts of methane (CH_4). The reason for this is that gas production may stop for economic reasons or due to technical issues such as water upcoming, long before the reservoir is actually depleted. For the same reasons, the pressures in depleted gas reservoirs are not necessarily low; it is common for pressures in deep gas reservoirs to be higher than the critical pressure of CO_2 (71 bars, 7.1 MPa).

Upon the injection of CO_2 into a depleted gas reservoir, mixing of injected CO_2 and residual CH_4 in place occurs by dispersion and molecular diffusion. When CO_2 mixes with CH_4, the mixture density decreases drastically as shown in Figure 27, which was computed by the NIST Chemistry Webbook as a function of pressure at 40°C (Linstrom and Mallard, 2001). Above the pressure of 100 bars (10 MPa), mixing of CO_2 with CH_4 causes a significant decrease in density. This means that the pressure in a gas reservoir can increase by the mixing of CH_4 and CO_2, even after the injection of CO_2 has stopped. The prediction of pressure rise in the injection and post-injection periods is critical for assessing the hazard of GCS-induced seismicity in depleted gas reservoirs.

In this work, TOUGH2/EOS7C was used to simulate the injection- and mixing-induced pressurization in the Mokelumne River Sandstone. The simulation cases present the results for different fault permeabilities and different formation porosities and permeabilities. The sensitivities of pressurization to the degree of sealing by faults, the storage of the reservoir, and the connectivity of the reservoir to the surrounding aquifers at the boundaries were analyzed from the simulation results.

5.2: Reservoir System and Input Data

The central portion of the 19-layer (483 m-thickness) reservoir model of the Mokelumne River Sandstone described in Sections 5.1.2 and 5.1.3 was used, with the following specifications: (1) The reservoir system extends from -21 to 21 km in the *x*-direction and from -30 to 31 km in the *y*-direction; (2) the model discretization, shown in Figure 28, is the original gridding scheme (rather than the simplified one described in Section 4.1.3); (3) the model does not extend into the deeper sedimentary formations; (4) all three of the faults implied by the seismic picks from Section 3.2.5 are included, two of which are connected and act as one fault (Fault B) for fluid flow; and (5) a low permeability gouge representing the Meganos Gorge was added under the caprock

to create potential traps for gases in the upper six layers (129 m-thickness) of the model. The distribution of permeability in the top layer is shown in Figure 29.

Figure 27: Density and Compressibility Factor (Z) of CO_2-CH_4 Mixtures as a Function of Pressure at 40°C.
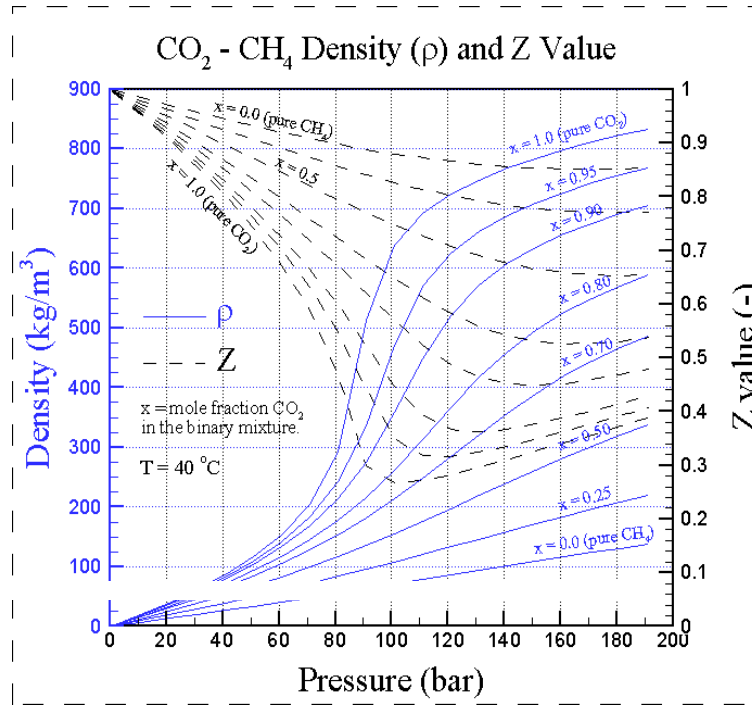
Figure 28: Faults A (right) and B (shown in blue) and Injection Well in the Reservoir System
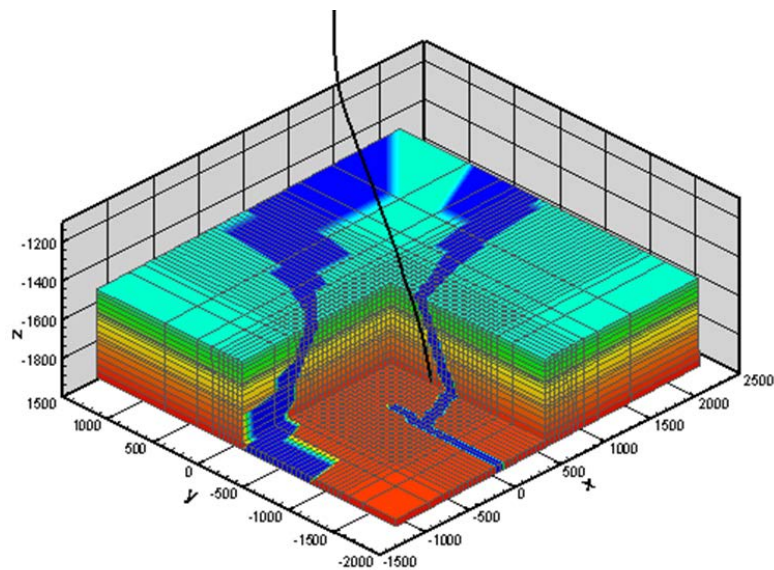
Figure 29: Permeability Distribution (mD) in Layer 1
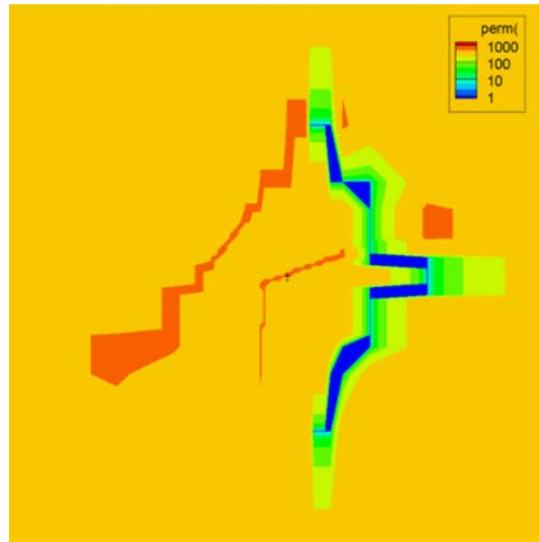
The reservoir is closed on all sides to represent faults or termination of the reservoir except in the $+x$-direction, where the reservoir has a constant-pressure boundary to represent a connection to a more distant high-permeability formation. The base case properties of the reservoir model used in the simulations are listed in Table 3. It was assumed that the reservoir system contains an aqueous phase at irreducible saturation equal to 25%, which corresponds to 75%-gaseous phase saturation. Average formation porosities and permeabilities were obtained from the well logs, and the averaging procedure described in Section 4.1.4.

Locating the injection interval to span the lower eight model layers (239 m-thickness) as before takes advantage of gravity stratification of CO_2 and CH_4; that is, the injection of CO_2 is done in the lower part of the reservoir, where dense CO_2 would naturally tend to migrate, in order to delay a mixing-induced pressure rise. The effects of density stratification were investigated by Oldenburg et al. (2004a) in the context of enhanced gas recovery using CO_2, during which the breakthrough of CO_2 to production wells was delayed by injecting CO_2 low in the reservoir and producing it from high in the reservoir.

Table 3: Reservoir System Base Case Properties

Property	Value	Property	Value
Molecular diffusivity (*D*)	10^{-5} [m²·s⁻¹]	Tortuosity (τ)	$\phi^{1/3}S_g^{10/3}$ (Millington and Quirk, 1961)
Initial saturations	S_a = 0.25 S_g = 0.75	CO$_2$ injection rate	50 Mt/year
Relative permeability (Van Genuchten, 1980)	S_{ira} = 0.25, S_{irg} = 0.01 S_{ls} = 1, λ = 0.457	Capillary pressure (Van Genuchten, 1980)	λ = 0.457, $1/P_0$ =5.1×10⁻⁵ [Pa⁻¹], P_{max} = 10⁷ [Pa]
Permeability across the faults	5.0×10⁻¹⁵ [m²]	Permeability along the faults	5.0×10⁻¹³ [m²]
Gouge permeability	3.0×10⁻¹⁶ [m²]		

5.3: Sensitivity Analyses and Results

In a high-quality reservoir with high porosity and permeability and an open boundary at hydrostatic pressure, pressure diffusion is expected to affect the pressure rise induced by injection and mixing. Pressure diffusivity is defined as transmissivity (*T*) divided by storativity (*S*) as shown in the following equation (Freeze and Cherry, 1979):

$$D_P = \frac{T}{S} = \frac{\dfrac{k\rho g}{\mu}b}{\rho g b(\alpha + \phi\beta)} = \frac{\dfrac{k}{\mu}}{\alpha + \phi\beta} \qquad \left[m^2 s^{-1}\right] \tag{5.1}$$

where *k* is the permeability of the reservoir [m²]; μ the viscosity of the fluid phase [Pa.s]; α and β the rock and fluid compressibilities [Pa⁻¹], respectively; and ϕ the porosity of the reservoir. From the dimensions of pressure diffusivity, the time scale for pressure diffusion (τ_P) can be estimated by the following equation:

$$\tau_P = \frac{L^2}{D_P} \tag{5.2}$$

where *L* is the length scale. Using the average permeability of the reservoir of 50 mD, viscosity 2.4 × 10⁻⁵ Pa.s, rock compressibility 1 × 10⁻⁸ Pa⁻¹, porosity 0.3, and fluid compressibility 1×10⁻⁷ Pa⁻¹, the pressure diffusivity is 0.052 m²/s. By inserting this pressure diffusivity and the distances between the top of the injection interval and Fault A (1,040 m) and Fault B (500 m) into Equation 5.2, time scales for hydraulic diffusion of 0.66 years (2.08 × 10⁷ s) and 0.15 years (4.80 × 10⁶ s) are obtained from the injection well to Fault A and Fault B, respectively.

Analyses were conducted of the sensitivity of pressure rise to: (1) Degree of sealing provided by faults; (2) the storativity of the reservoir; and (3) the connectivity of the reservoir to an open

boundary. Sensitivity analysis Case 1, to fault permeability, was done by decreasing the fault permeabilities in Table 5.1 by factors of (a) 20 and (b) 100. Sensitivity analysis Case 2, to storativity, was done by reducing the average porosity in each layer derived from Figure 4.6 by (a) 50% and (b) 75%. Sensitivity analysis Case 3, to reservoir permeability, which controls pressure communication to the open boundary, was done by reducing the average permeability in each layer by (a) 50% and (b) 75%.

TOUGH2/EOS7C was used to model the system of water, brine, CO_2, a gas tracer, and CH_4 (Oldenburg et al., 2004b). The initial gas in the pore space was composed primarily of CH_4, minor water vapor and CO_2. The injection rate was chosen as an extremely high value of 50 Mt of CO_2 per year, to produce a clear injection-induced pressure rise. The injection was simulated for 50 years to clearly see any effect of CO_2-CH_4 mixing in the reservoir.

Pressure rise and mass fraction of CO_2 in the gaseous phase versus time for the various sensitivity analyses are shown in Figures 30-33. Pressure and gas composition were observed at three monitoring points: at the top of the injection interval and at Faults A and B at the same depth. Results only for the period of injection for Cases 2 and 3 (Figures 32 and 33) are presented, because the post-injection period showed very similar behavior to the base case. In every case, the pressure rise at Fault B was higher than that at Fault A because of the shorter distance to the injection well. In the base case (Figure 30) and Case 1 (Figure 31), it was found that the pressures at the monitoring points drastically decreased after the 50- year injection period because of active pressure diffusion to the surrounding reservoir.

Figure 30: Pressure Rise (*left*) and Mass Fraction of CO_2 (*right*) in Gaseous Phase vs. Time-Base Case
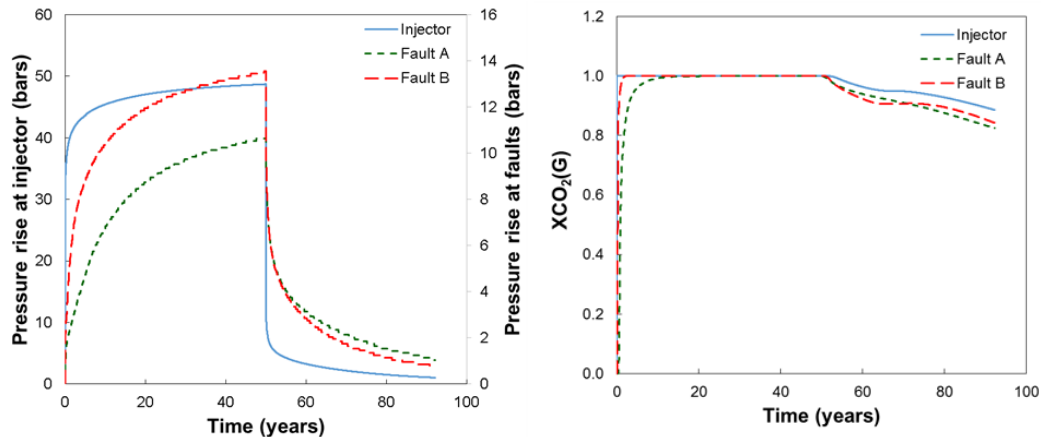
Note different ordinate scales for the pressure rise at the injector and faults. 10 bars = 1 MPa.

The mass fraction of CO_2 in the gaseous phase at the faults approached unity within 20 years in every case except for Case 1b (Figure 31, bottom). Decreasing the porosity of the reservoir (Case 2) shortened the time for the mass fraction of CO_2 to approach unity at the faults. On the other hand, decreasing the permeabilities of the reservoir and the faults (Cases 1 and 3) extended the

approach time. In the post-injection period, the mass fraction of CO_2 in the gaseous phase gradually decreased by molecular diffusion to the surrounding reservoir.

The maximum pressure rise at the faults in each case is summarized in Table 4. Every maximum pressure rise was injection-induced. Case 3b showed the largest pressure rise at the faults (34.09 bars; 3.409 MPa). The maximum pressure rise comparisons indicate that pressurization resulting from decreased reservoir permeability is more significant than that from decreased reservoir porosity or fault permeability.

Figure 31: Pressure Rise (*left*) and Mass Fraction of CO_2 (*right)* in Gaseous Phase vs. Time for Sensitivity Analysis Case 1
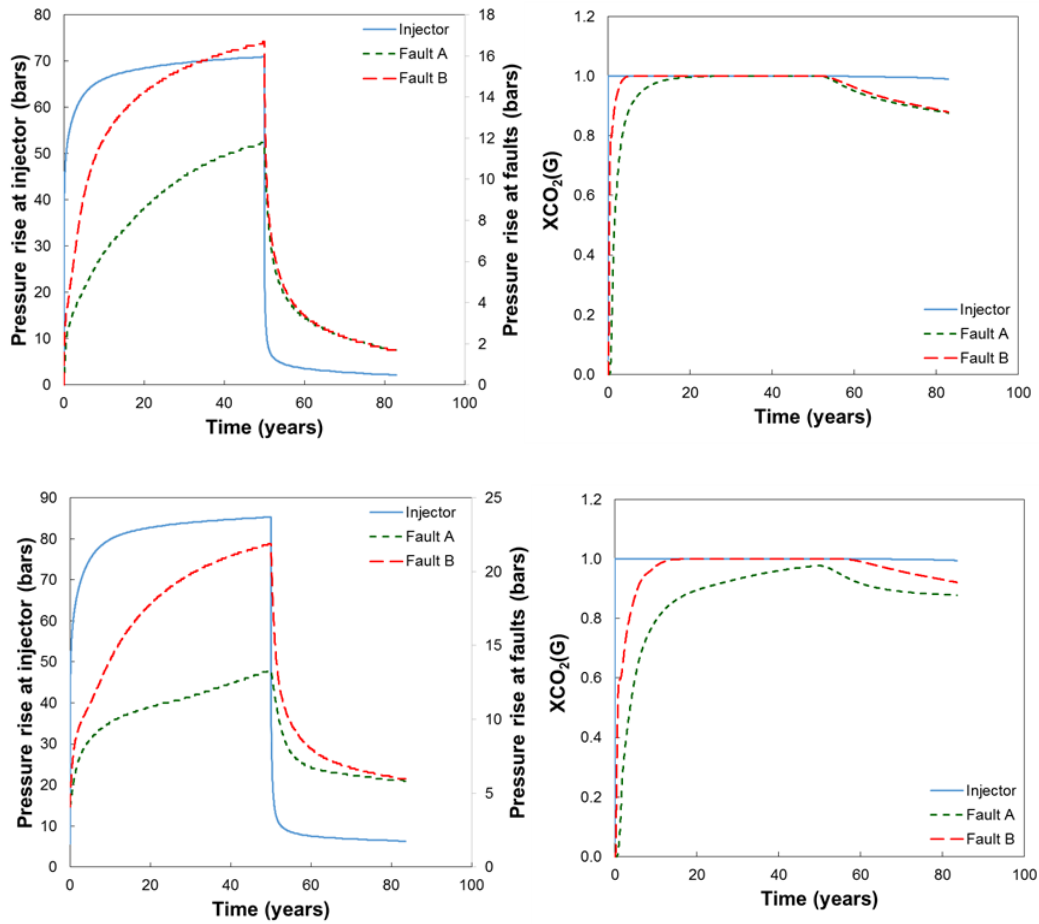
Case 1 (different values of cross-fault permeability). Case 1a (top), Case 1b (bottom). Note different ordinate scales for the pressure rise at the injector and faults. 10 bars = 1 MPa.

Figure 32: Pressure Rise (*left*) and Mass Fraction of CO₂ (*right)* in Gaseous Phase vs. Time for Sensitivity Analysis Case 2
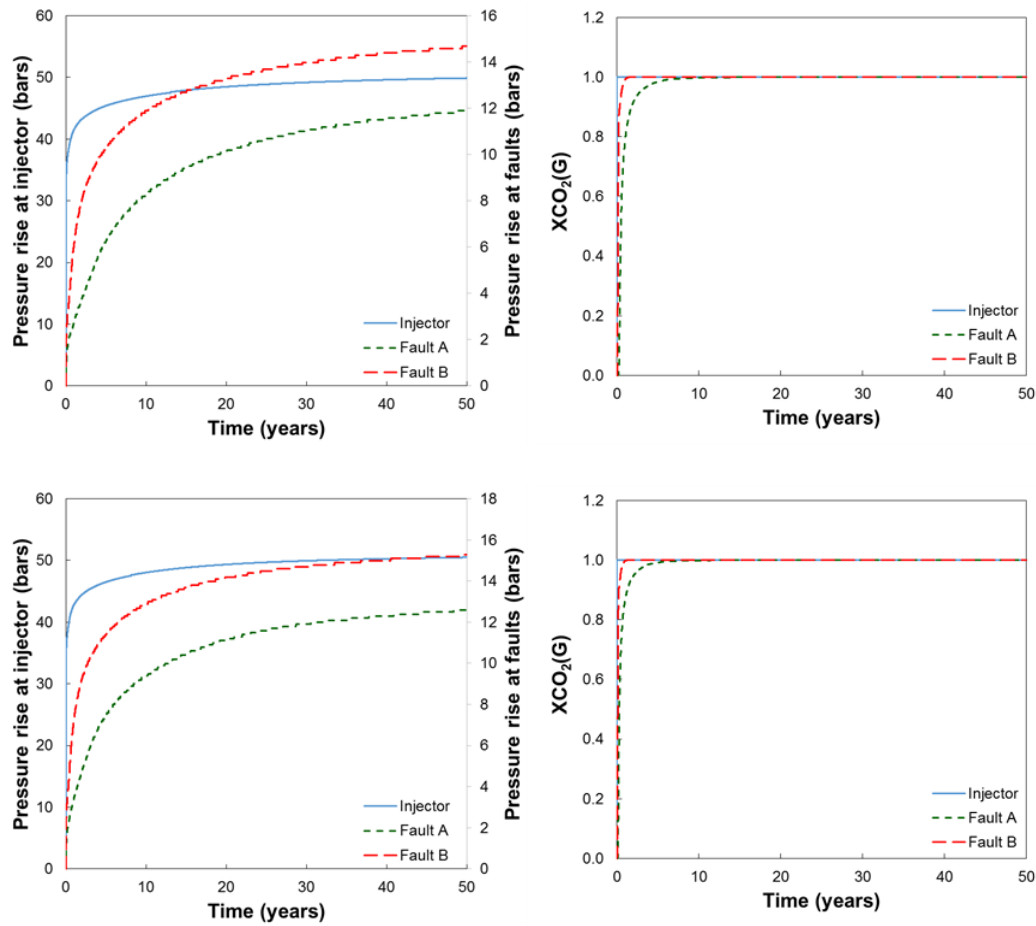
Case 2 (different values of reservoir porosity). Case 2a (top), Case 2b (bottom). Note different vertical axes were used for the pressure rise at the injector and faults. 10 bars = 1 MPa.

Table 4: Maximum Pressure Rises at the Faults

	Maximum pressure rise at the faults	
Base case	13.55 bars*	
Case 1: Across-fault permeability	(a) 0.05 times base value	(b) 0.01 times base value
	16.69 bars	21.89 bars
Case 2: Reservoir porosity	(a) 0.5 times base value	(b) 0.25 times base value
	14.69 bars	15.29 bars
Case3: Reservoir permeability	(a) 0.5 times base value	(b) 0.25 times base value
	21.49 bars	34.09 bars

* 10 bars = 1MPa

Figure 33: Pressure Rise (*left*) and Mass Fraction of CO₂ (*right*) in Gaseous Phase vs. Time for Sensitivity Analysis Case 3
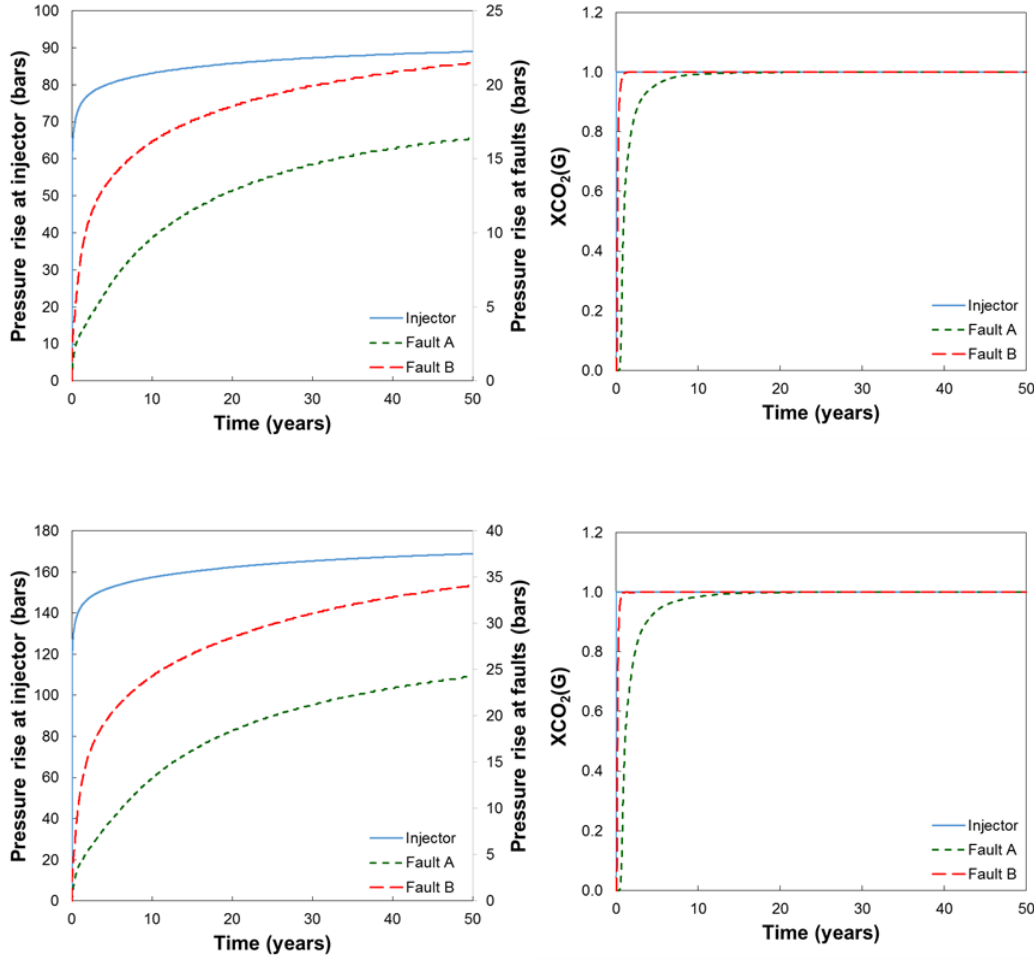
Case 3 (different values of reservoir permeability).Case 3a (top), Case 3b (bottom). Note different vertical axes were used for the pressure rise at the injector and faults. 10 bars = 1 MPa.

5.4: Discussion of the Effect of Methane-CO₂ Mixing

The time scale of mixing by molecular diffusion (τ_D) can be computed by the following equation:

(5.3)

$$\tau_D = \frac{L^2}{D_D} = \frac{L^2}{\phi \tau D}$$

where the tortuosity is 0.077 (= $\phi\tau = \phi^{4/3}S_g^{10/3} = 0.3^{4/3}0.75^{10/3}$)) (Millington and Quirk, (1961).

The distances between the injection well and the monitoring points at Faults A and B are 1,040 m and 500 m, respectively. From these values, the mixing times by molecular diffusion for Faults A and B are 1.48×10^5 years and 3.43×10^4 years, respectively. Time scales for hydraulic pressure diffusion over these two injection well-to-fault distances can be estimated from Equations 5.1 and 5.2, from which time scales of 0.66 years (2.08×10^7 s) and 0.15 years (4.80×10^6 s), respectively are obtained. Clearly, the much longer time scale for molecular diffusion means that over the time that mixing is occurring, hydraulic processes can act to dissipate pressure rise. And these effects

54

can be seen from the results, which showed negligible effects of mixing-induced pressurization. In summary, long distances from the injection well to the faults and hydraulic connection to surrounding aquifers dampened the effects of injection- and mixing-induced pressurization, respectively.

From the simulations of CO_2 injection into the depleted gas reservoir of the Mokelumne River Sandstone, it is found that the pressure rise at the faults due to the mixing of injected CO_2 and residual CH_4 after injection is dampened by pressure diffusion. When compared to simulations of CO_2 injection with no CH_4 initially present, the simulation results of the previous section show that the pressure rise due to the injection of CO_2 into a reservoir containing CH_4 is lower than the case of a reservoir model filled with 100% aqueous phase, because of the larger compressibility of CH_4 compared to water. The simulation cases revealed the sensitivity of pressurization to the fault permeability, reservoir porosity, and reservoir permeability. Pressure rise in every case was induced by the injection of CO_2. The mixing effect on pressurization after the injection of CO_2 was not explicitly observed, due to the strong effect of pressure diffusion. In the most pressurized case (Case 3b), the maximum pressure increase at the fault was 34.09 bars. From the sensitivity analyses, it was found that decreasing the permeability of the reservoir had a more significant effect on pressure rise than did decreasing the porosity of the reservoir or the permeability of faults.

CHAPTER 6:
Simulation-Based Probabilistic Seismic Hazard And Risk Assessment For King Island

6.1: Introduction to Induced Seismic Hazard and Risk Assessment

6.1.1: Overview

LBNL has developed an approach to assessing the risk from induced seismicity that adapts the conventional Probabilistic Seismic Risk Analysis (PSRA) method widely used to estimate the risk of structural damage from naturally-occurring earthquakes (e.g. Cornell, 1968; Budnitz et al., 1997). PSRA links the probability of occurrence of earthquakes to their societal consequences, which in the case of induced seismicity include nuisance caused by felt ground shaking as well as structural damage. A comprehensive discussion of the application of PSRA to seismicity related to GCS is given in a recent paper by White and Foxall (2016).

In general, PSRA involves the following steps:

1. Characterization of earthquake sources.
2. Estimation of the frequencies of occurrence of earthquakes of different magnitudes on each source.
3. Calculation of the ground shaking produced by each earthquake at sites of interest quantified in terms of ground acceleration or velocity or seismic intensity. The ground motions are functions primarily of source-to-site distance, earthquake magnitude, and local site conditions.
4. Integration of the frequencies of occurrence of ground motions generated by all of the sources to produce a hazard curve. The hazard curve expresses the annual (or other interval) probability of exceeding each ground motion value, and is used to forecast the hazard over future time periods of different lengths.
5. Development of vulnerability functions that express the probability of a particular consequence from each level of ground motion. For conventional PSRA the consequences are degrees of structural damage, but for induced seismicity they also include the probability of causing nuisance.
6. Convolution of the hazard curve with the vulnerability functions to produce risk curves, which give the annual probabilities of given consequences, such as specific degrees of structural damage.

Steps 1 to 4 together are termed Probabilistic Seismic Hazard Assessment (PSHA), while Steps 5 and 6 add the consequence element to complete the PSRA. The general purpose PSRA computational framework developed at LBNL for both naturally-occurring and induced seismicity is shown schematically in Figure 34, in which the circled numbers refer to the steps above. The framework can accommodate seismicity catalogs (Steps 1 and 2) generated either empirically or

by physics-based or stochastic hybrid simulation. Similarly, a variety of empirically-based, analytical or numerical methods can be used to calculate earthquake ground motions (Step 3). Some of these alternatives are discussed later in this chapter.

Figure 34: Probabilistic Seismic Risk Analysis General Purpose Computational Framework
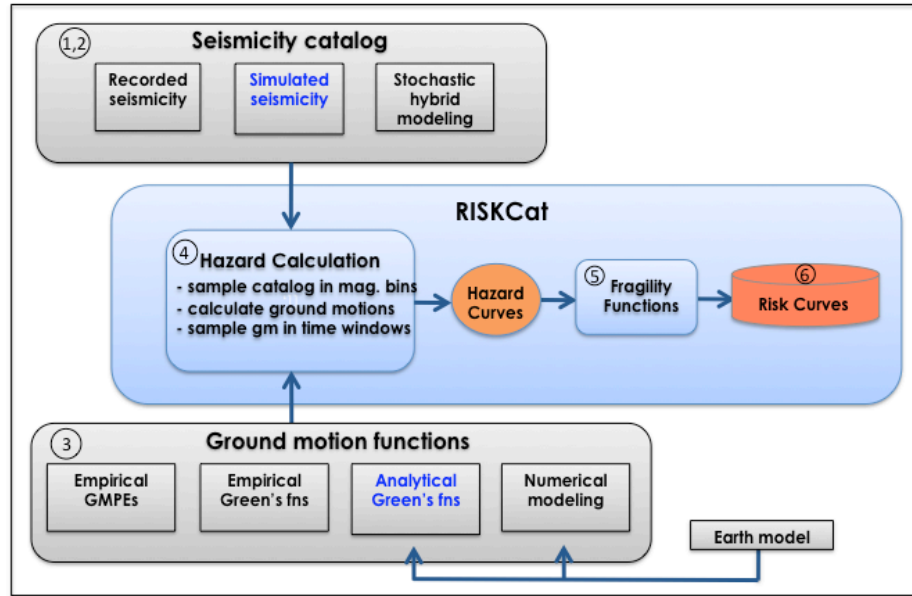
Circled numbers refer to the six PSRA steps. The methods used to generate seismicity catalogs and calculate ground motions in this study are shown in blue.

Important modifications to the standard PSRA approach are required in order to apply it to induced seismicity. The first modification is to Step 2. In conventional PSHA earthquake frequencies are estimated from an existing historical seismicity catalog and from long-term tectonic slip rates on known active faults. In most PSHA applications earthquake occurrence is assumed to be a stationary Poissonian process – i.e. the probability of an earthquake occurring is independent of time – and uniformly distributed across each source. This assumption cannot be applied to fluid-induced seismicity, where the growth of the overpressure plume resulting from injection introduces strong time- and space-dependency to induced earthquake occurrence. Furthermore, whereas recorded seismicity can be used to estimate hazard and risk on an ongoing basis during and after injection, obviously no catalog of induced events can exist during the project planning and permitting phase of a project, before injection begins. Therefore, alternative means of estimating induced earthquake frequencies for PSRA at this pre-injection phase – the focus of the present study – have to be devised, and these must incorporate a dependence on injection and subsurface flow parameters.

The second modification is needed because the risk of nuisance from induced seismicity must be considered as well as damage risk. The damaging earthquakes of concern in standard PSHA generally have magnitudes greater than about M4.5, but shallow, local induced earthquakes as small as M2 can be felt in nearby communities. Extending the magnitude range of concern has implications for Steps 3 and 6. In standard PSHA, ground motions for Step 3 are normally calculated using generic ground motion prediction equations (GMPEs) empirically determined by

57

regressions on worldwide data. The most recent GMPEs extend down to M3, but are very poorly constrained below M6 and at distances less than 5 km. Douglas et al. (2013) developed GMPEs for magnitudes less than 3.5, but the uncertainties in these are quite large. Alternative methods of calculating ground motions for pre-injection PSHA include deriving site-specific GMPEs using recorded data from local earthquakes or a VSP (see Section 3.2.1), numerical wave propagation modeling and empirical and synthetic Green's functions (the transfer functions that account for wave propagation between the earthquake source and receiver site).

6.1.2: Treatment of Uncertainty

The probabilistic framework for seismic hazard analysis was introduced specifically to deal with the uncertainties in the input earth science data, which are usually quite large. Uncertainties are commonly classified into two categories: The first are epistemic uncertainties, which stem from lack of knowledge, of, for example, the true shear loading rate and the geometry of a fault at depth used to estimate maximum earthquake magnitude and frequencies of occurrence; the second are aleatory uncertainties caused by inherent randomness in a physical process. In theory, epistemic uncertainties are reducible by further measurement or research but aleatory uncertainties are not.

Because of the generally large uncertainties in input parameters, a seismic hazard estimate can be accurately represented only by giving the full range of uncertainty, i.e. the mean or median hazard curve plus upper and lower percentile uncertainty bounds. This is accomplished by carrying out multiple realizations of the hazard calculation that sample the entire uncertainty distributions of all of the input parameters used to calculate earthquake frequencies and ground motions (Budnitz et al., 1997). This is achieved in the general-purpose RiskCat code (Figure 6.1) developed at LBNL and used in the present study by Monte Carlo sampling.

6.2: Simulation-based Approach to Seismic Hazard Assessment

6.2.1: Induced Earthquake Simulation

The problem of generating the frequency-magnitude distributions (Steps 1 and 2) needed for induced seismicity hazard assessment prior to injection remains the subject of ongoing research. The most promising approaches proposed to date involve simulation of induced seismicity catalogs using some form of hydromechanical modeling in which earthquakes are triggered by a reduction in the frictional shear strength on a fault (or fracture) resulting from increased fluid pressure. In its most basic form, the frictional strength – or resistance to shear slip – of a cohesionless fault is given by the modified Coulomb relation

$$\tau_s = \mu(\sigma - P),$$
(6.1)

where τ_s is the shear strength, μ the coefficient of friction, σ the normal stress applied perpendicular to the fault plane, and P the fluid pressure within the fault. Therefore, the *effective* confining stress that prevents the fault from slipping is $(\sigma - P)$. The onset of fault slip occurs when the applied shear stress τ becomes equal to τ_s. This critical state occurs either by increasing the shear stress, decreasing the normal stress, or increasing the pressure (or a combination of all

58

three). Fault slip caused by an increase in fluid pressure is recognized as the primary cause of fluid-induced seismicity, although poroelastic stress changes may also play a role.

Hybrid physical-statistical models have showed some success in simulating the seismicity "clouds" induced by short-term injection for enhanced geothermal stimulation (Goertz-Allmann and Wiemer, 2013; Gischig and Wiemer, 2013), but they rely on very simplified physics and have not been developed to simulate seismicity on specific larger-scale faults. On the other hand, sophisticated numerical models that incorporate much of the physics of coupled hydromechanical processes responsible for fluid-induced seismicity (e.g. McClure and Horne, 2011; Cappa and Rutqvist, 2012) are too computationally intensive to be a practical means of simulating entire seismicity catalogs, let alone the large numbers of catalog realizations required for PSHA.

In this project the computer program RSQSim is used to simulate earthquakes induced on multiple faults by CO_2 injection. RSQSim was developed by Dieterich and Richards-Dinger at UC Riverside (Dieterich and Richards-Dinger, 2010; Richards-Dinger and Dieterich, 2012), who have recently extended the code capabilities to include simulation of fluid-induced earthquakes (Dieterich et al., 2015). The core physics employed in RSQSim is a rate-and-state frictional law (e.g., Dieterich, 1978; Ruina, 1983; Marone, 1998). Rate-and-state frictional laws were empirically derived from laboratory experiments, and provide the most complete description of the mechanics of earthquake nucleation and the entire earthquake cycle currently available (Ben-Zion, 2008). A brief description of the rate-and-state formulation used in RSQSim is given in Appendix C. A key feature of RSQSim that enables rapid simulation of very large seismicity catalogs over arbitrarily long time periods is that adaptive, event-driven time steps are determined by approximate analytical calculations, which is computationally much faster than time stepping over predetermined fixed intervals.

6.2.2: RSQSim Simulations of Induced Seismicity Catalogs

To generate seismicity catalogs, faults and fractures in the simulation model are gridded into elements and are subject to constant-rate long-term tectonic shear loading. The resolved initial normal and shear stresses on the faults at the beginning of a simulation are determined from the in situ tectonic stress field (Section 3.4). Because heterogeneous stress distributions are required to generate realistic earthquake frequency-magnitude statistics (e.g. Ben-Zion, 2008; Dieterich et al., 2015), these depth-dependent initial stresses are randomized by applying fractally-distributed perturbations.

The pore pressure time history on the faults resulting from injection is computed in advance as described in Chapter 4, and input to RSQSim to modify the effective stress on each element over time. When seismic slip nucleates under the prevailing shear and effective stresses on one of the fault elements according to the rate-and-state law, the resulting release of stress is transferred to all of the other elements in the model using a 3D boundary element calculation. This can cause other elements to fail in quick succession, so that larger earthquakes are produced by cascading sequences of element failures. Therefore, each of these larger events is modeled as a sequence of point-source sub-events that propagates on the fault from the nucleation point (hypocenter) at the earthquake rupture velocity.

The shear stress on an element at any given time is determined by the steady-state tectonic loading, the time since it last failed and contributions from other element failures. The effective stress is likewise determined by the pore pressure history and stress transfer from other element failures. The stress transfers from many element failures over time means that the stress distribution initially imposed is eventually forgotten. In practice, this is accomplished by running the model for a preliminary "burn-in" period to evolve the highly heterogeneous stress distribution characteristic of a fault that has experienced many earthquake cycles. This is then used as the initial stress distribution for the actual catalog simulation. The pore pressure history is typically applied sometime after the catalog simulation starts, which allows an estimate of the background tectonic seismicity rate to be made.

There are two important limitations in using RSQSim for induced seismicity simulations. The first is that fault slip is quasi-static, so that elastodynamic effects can only be approximated. The second is that potential slip-induced changes in fault permeability cannot be directly coupled back into the flow simulation. The present state of knowledge about shear slip-related permeability changes, particularly in sedimentary rocks, is insufficient to assess the effect of the latter limitation on the simulation results. Laboratory experiments like the one discussed in Chapter 7, indicate that the permeability response to slip depends heavily on the host rock type. Other factors, such as the maturity of the fault, which governs the mechanical characteristics and lithology of fault gouge materials and the architecture of the fault zone, and the scaling of slip to field scales are as yet very poorly understood.

6.2.3: Earthquake Ground Motion Calculations

In the present application, earthquake ground motions are calculated using synthetic Green's functions. These are synthesized using the LBNL computer code SYNHaz, which is an extension of the code EMPSYN of Hutchings et al. (2007). The Green's functions, which represent the point-source response (wave propagation) of the Earth along specific source-site paths, are computed using the frequency-wavenumber computer code FKRPROG (Saikia, 1994). Ground motions from each earthquake are calculated by convolving the source slip-rate function derived from the coseismic slip speed, slip duration and stress drop for each sub-event simulated by RSQSim with the appropriate Green's function, and summing the in-phase contributions from all of the sub-events (e.g. Graves and Pitarka, 2010; Hutchings et al., 2007).

6.2.4: Probabilistic Seismic Hazard and Risk Calculations

At the heart of the PSRA framework shown in Figure 35 is the computer code RiskCat, which was developed jointly by LBNL and LLNL. RiskCat is designed to be a general- purpose code that can accommodate seismicity catalog input and ground motion calculations from a variety of sources. SYNHaz is fully integrated into the hazard calculation framework.

RiskCat uses the basic historical approach to estimate seismic hazard (Veneziano et al., 1984), in which the hazard is calculated by statistical analysis of ground motions observed over a long time period. RiskCat makes no assumptions about the time and space distribution of seismicity, and therefore can accommodate any type of time and space non-stationary. When simulated seismicity is used as input, many synthetic catalogs are used to account for uncertainty, as

described in Section 6.1.2. Synthetic catalogs generated by physics-based simulation can be calibrated with regional seismicity when available. RiskCat can also generate seismicity catalogs from a description of potential seismic sources using a Monte-Carlo simulation procedure similar to that of Musson (2000). Ground-motion calculation options include SYNHaz or empirical GMPEs (Section 6.1.1). The code also performs additional random sampling to account for aleatory and epistemic uncertainties in all the input parameters.

Because of the strong non-stationarity in the frequency-magnitude characteristics of fluid-induced seismicity over geologically short times, it is necessary to calculate the hazard for time windows having different durations. Induced seismicity hazard calculation using catalogs generated by RSQSim presents a considerable computational challenge owing to the very large number of small- to medium-sized simulated events. Therefore, RiskCat employs an elaborate scheme to sample the seismicity in a set of

Figure 35: Nuisance Vulnerability Curves
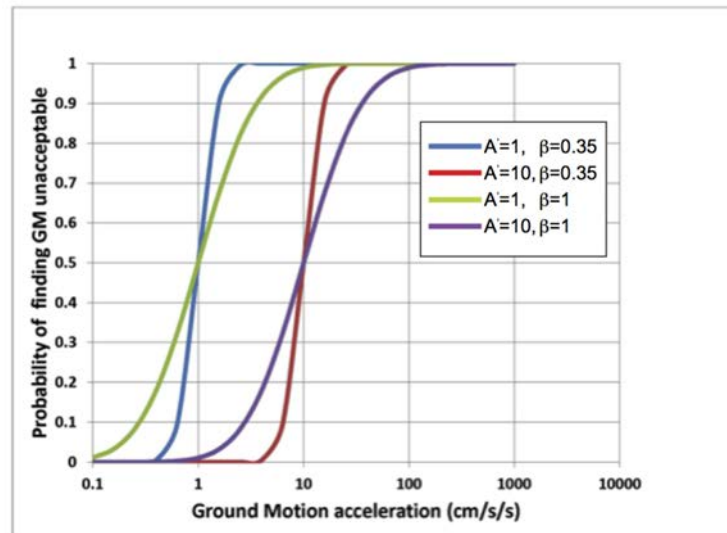
Each curve shows the vulnerability for a combination of A' and β□ A' is the anchor acceleration value at which there is a 50% probability that a person would find the ground motion unacceptable, and β is the epistemic uncertainty on that value.

magnitude bins to reduce calculation times significantly. Constraints on the sampling parameters under which the results are statistically stable are determined through extensive sensitivity analyses. Hazard curves (see Section 6.1.1) are expressed in terms of ground acceleration, velocity or displacement, or as the Uniform Hazard Response Spectra commonly used for structural design of critical facilities.

Because almost all of the induced earthquakes simulated under the King Island injection scenarios are smaller than M4.5, the analysis focused on the risk of nuisance. The "nuisance" parameter, *Nu*, is defined as the probability that a person would find a certain level of ground shaking to be unacceptable. Therefore, *Nu* takes values between 0 and 1; *Nu* = 0 implies that there is zero probability that a person would find the ground-motion unacceptable, and a value of

61

one would mean that the shaking would certainly be unacceptable. *Nu* can alternatively be interpreted as the percentage of people in an homogeneous population that would find the ground-motion unacceptable, which can be useful in estimating the average number of people in a given community that would be concerned or alarmed.

The risk of nuisance R_{Nu} is defined as the (annual) probability of exceeding a given value of nuisance. Therefore, the type of vulnerability function needed to calculate R_{Nu} from the hazard curve (Section 6.1.1, Steps 5 and 6) is in the form of a curve that plots *Nu* as a function of ground motion. Vulnerability functions used to calculate structural damage risk curves are usually in the form of fragility curves, such as those developed by the HAZUS project of the U.S. Federal Emergency Management Agency (FEMA, 2013). Less attention has been paid to developing vulnerability functions to estimate nuisance risk, although there has been extensive work on developing acceptability criteria for non-damaging ground motion and vibration from mining and construction (Dowding, 1996). Based on these criteria, preliminary nuisance vulnerability functions have been developed under the U.S. Energy Department's National Risk Assessment Partnership (https://edx.netl.doe.gov/nrap) following the same general approach as that used for damage fragility functions. Examples of nuisance vulnerability functions are shown in Figure 36. Following the approach of Kennedy et al. (1980; see also Majer et al., 2016), the time derivative of the ground-motion hazard curve is used to represent the frequency of occurrence of each ground-motion value, and that is combined with the fragility function to compute the risk. Examples of risk curves together with their corresponding hazard curves are shown in Section 6.4.

6.3: Application to King Island CO₂ Injection Scenarios

6.3.1: Induced Seismicity Catalog Realizations

The fault planes shown previously were resampled on to a grid of 50 m x 50 m elements for the seismicity simulations. This element size implies that the minimum event magnitude that can be simulated is about 1.5. Both faults extend from the top of the Mokelumne River Sandstone at about 1,400 m depth to 5,700 m, below the base of the sedimentary sequence. The in-plane dimensions of Fault A are 4.95 and 4.45 km in the along strike and dip directions, respectively, comprising 9000 elements; Fault B is 4.45 km both along strike and down-dip, totaling 8100 elements. The fluid pressure time history on each element was determined by spatial interpolation from the TOUGH2 grid.

In total, 467 induced seismicity catalog realizations were carried out using the fixed fault geometries described above and pressure histories from the base case flow simulation (8 Mt/year for 20 years) described in Section 4.2.1. Figure 36 shows the pressure distributions on the fault planes 5 and 10 years after the beginning of injection. The simulations were carried out in two parts. First, 20 burn-in runs were performed, the duration of each being sufficiently long to ensure that every grid element had ruptured at least once. Up 25 catalog realizations were then performed for each burn-in; i.e., the fault stresses at the end of the burn-in were used as the initial stress state for each of the realizations.

Figure 36: Pressure Changes in MPa on Faults A and B After (*left*) 5 Years and (*right*) 10 Years of Injection at 8 Mt/year
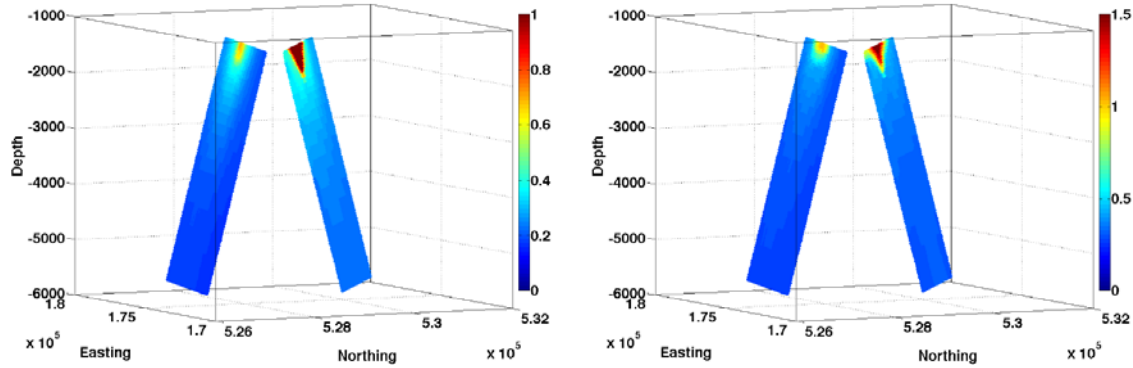
Note the different pressure scales for left and right figures.

Steady-state shear stress loading for each burn-in run was calculated assuming a long-term tectonic slip rate randomly sampled from a uniform distribution across the range $0.5\pm$ 0.05mm/year on both faults. Initial depth-dependent shear and normal stresses resolved on the faults at the beginning of each burn-in run were first calculated from the principal stress gradient ratios estimated in Section 3.4 and by randomly selecting an S_H azimuth from a uniform distribution across the range 039° to 059° (i.e., ±10° deviation on the best estimate value of 049°). The resulting regular, depth-dependent stress distributions were then perturbed by a randomly generated power-law distribution of the type characteristic of displacement and stress fields on active faults. These initial stresses resulted in dextral-reverse slip on both faults with rake angles (direction of the slip vector on the fault plane with respect to the strike direction) of about 20° to 25°. The random sampling is carried out by running RSQSim from within a Unix script, which also executes pre- and post-processing tasks.

Other parameters were either fixed or randomly sampled for both burn-in runs and catalog realizations, as indicated in Table 5. The Lamé parameters λ and μ were fixed at their values at 5.3 km depth. The rest of the parameters are those used in the rate-and-state law (see Appendix C). Note that the parameter ranges used in this demonstration do not capture the full uncertainty in the inputs that would be required in applying the simulation-based method to a real GCS site. In particular, the fault geometries are held fixed to limit the number of flow modeling runs required. The uncertainty bounds on some of the rate-and-state parameters may be too narrow, but this is because a comprehensive investigation of allowable combinations of these parameters has not yet been carried out.

Each catalog realization was run for a duration of 5,000 years or until 20,000 events had been simulated, whichever occurred first. The pressure history was applied beginning at 2,500 years. Therefore, pre-injection background seismicity was simulated from 0 to 2,500 years. The response to injection varied markedly among the realizations, as illustrated by the two examples shown in Figure 37. In all of the realizations, induced events began to occur soon after injection began and continued through the 20-year injection period. In some cases the increase in pressure induced relatively large (M3.5-4.5) events (e.g., top panel of Figure 37), but in other realizations

63

the response was a large increase in the occurrence of small events (e.g., bottom panel of Fig 37). In some instances the enhanced seismicity stopped abruptly after peak pressure was reached, but in others it continued through the period of pressure decay and even for some time after the pressure had declined to hydrostatic. A long-term effect of injection seen in some of the realizations was an increase in the minimum magnitude for periods up to several hundred years after injection. This might be an artifact of the simulations, but it has minimal, if any, impact on the risk results. Figure 38 shows an example of the rupture progression and final slip distribution on Fault A for an M4.2 earthquake.

Table 5: Earthquake Simulation Parameters

Parameter	Values
S_H azimuth[2]	049±10°
Long-term fault slip rate[2]	0.5±0.05 mm/yr
First Lamé parameter, λ	23.0 GPa
Shear modulus, μ	17.4 GPa
Steady-state coefficient of friction, μ_0	0.6 - 0.7
Rate-and-state direct effect parameter, a	0.001 – 0.0035
Rate-and-state evolution parameter, b	0.004
a reduction factor, fa	0.1 – 0.3
Stress overshoot factor, s	01. – 0.25
State evolution distance, D_c	10 $\square$m
Reference slip speed, V^*	1x10^{-6} m/s
Coseismic slip speed, V^{eq}	1 m/s
Normal stress modification factor, α	0.05 – 0.25

Notes: (1) See Appendix C for a description of the rate-and-state formulation (2) Burn-in runs only

Figure 37: Snapshots of Two Seismicity Realizations
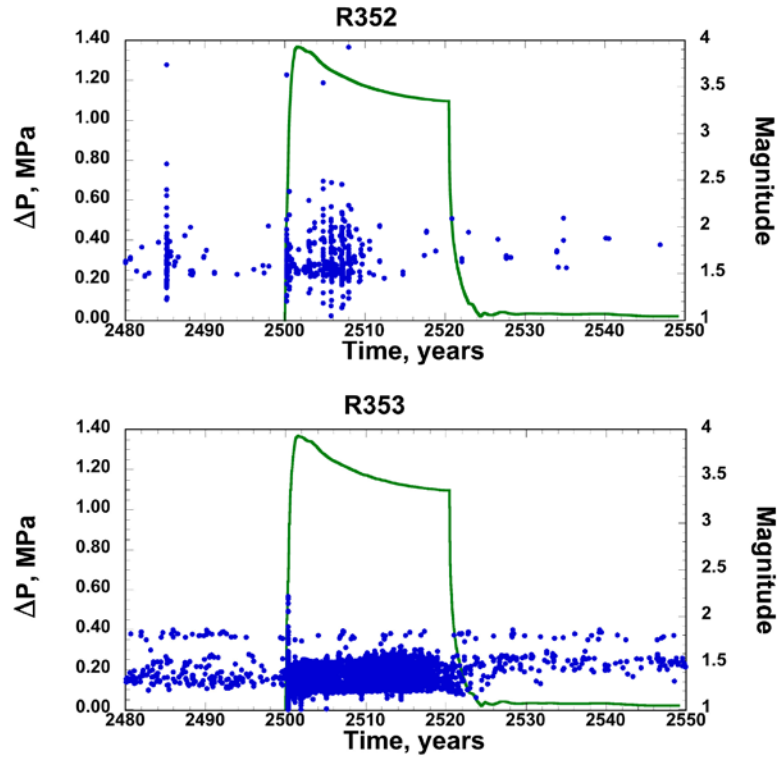
Realizations show differing responses to fluid pressure change (*green*).Seismic moment release during injection includes three events M>3.5 in the top sequence, but is largely concentrated in an intense swarm of small events in the bottom sequence.

Figure 38: Rupture Time (*left*) and Final Slip (*right*) for a Simulated M4.2 Earthquake
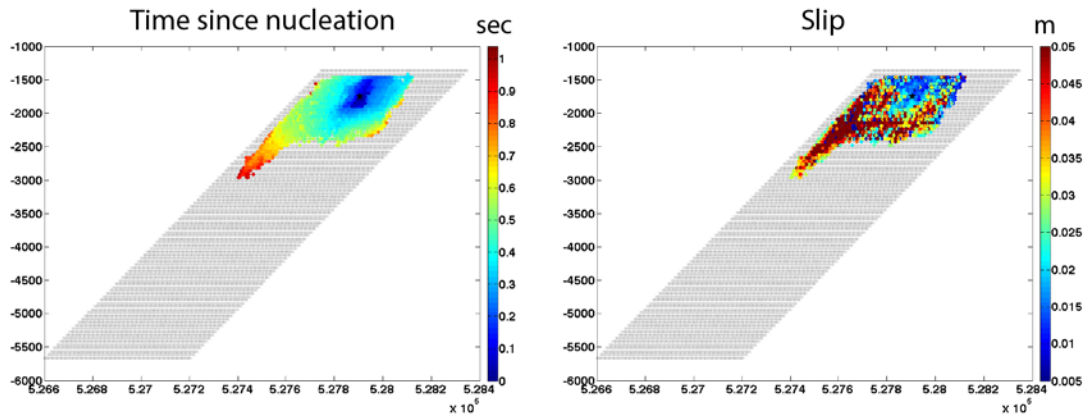
6.3.2: Ground Motion Calculations for King Island

The V_p and V_s models described in Section 3.3 were each simplified to a single velocity gradient overlying a constant-velocity (V_p=6.3 km/s, V_s=3.68 km/s) half-space to calculate synthetic point-source Green's functions using FKRPROG. The simplified V_p and V_s models depart appreciably from the original models only below depths of 7.4 km and 6.5 km, respectively, which has no

65

impact on the Green's functions computed. The Q_p, and Q_s models from Section 3.3 are also used in the Green's function calculations. No uncertainties are applied to the velocity and Q models. Peak ground motion accelerations from all of the events sampled by RiskCat from each catalog realization were calculated at the surface site shown in Figure 39. Shallow site corrections were not applied.6.4: Probabilistic Seismic Hazard and Risk Results Initial RiskCat runs used different subsets of the 467 simulated seismicity catalogs available for King Island to evaluate the sensitivity of the hazard results to the number of catalog realizations. The results were found to be closely similar for runs based on 50 realizations or more except at very low acceleration/high probability ground motions that are well below the nuisance risk threshold. Conservatively, 150 realizations were used for subsequent runs.

Figure 39: Surface Receiver Site in Relation to the Surface Projections of Faults A and B
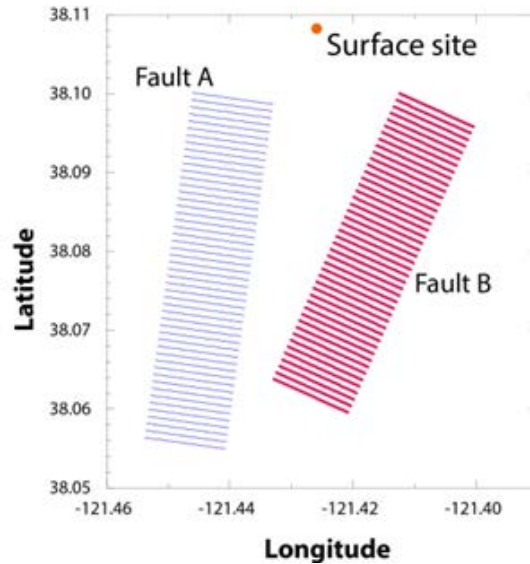
Figure 40 shows the mean hazard (mean annual probability of exceedance) for the surface site calculated over four time periods; the 0–2,500 year pre-injection period, 2,500–2,525 years from the start of injection until five years after well shut-in, and then two long post-injection intervals, 2,525–3,025 and 3,025–5,000 years; note that the fluid pressures over of both fault planes had returned to the ambient hydrostatic background about five years after shut-in. The pre-injection period and the 25 years following the start of injection are of the most interest. Only ground motion levels above about 10 cm/s/s (0.01g) are of relevance to the risk of nuisance, and above about 100 cm/s/s (0.1g) to damage risk. Within this range of ground motions the hazard is relatively low. At the 10 cm/s/s approximate threshold for nuisance risk the hazard is 0.2, which corresponds to an exceedance probability of 5% in 25 years; the mean hazard at 500 cm/s/s, within the range of damaging ground motions, is on the order of 0.001, or 0.025% probability in 25 years. A difference between the pre-injection mean hazard (red curve) and the hazard for the following 25 years (green curve) is discernable only for ground motions above about 2 cm/s/s (0.02g), where the difference monotonically increases with increasing ground motion/decreasing hazard. The 50 cm/s/s hazard increases 22% from 0.018 (0.45% in 25 years) to 0.022 (0.55% in 25 years); the hazard at 500 cm/s/s increases 70% from 0.001 (0.025% in 25 years) to 0.0017

66

(0.043% in 25 years). The hazard curve above 10 cm/s/s for the 2,525−3,025 post-injection period (blue) falls below the 2,500-2,525 curve, as would be expected, but does not return to pre-injection levels. This might be an artifact in the simulation process, but this has not yet been investigated.

Figure 40: Mean Hazard Curves for the Surface Site - Pre-injection (0-2,500 years)
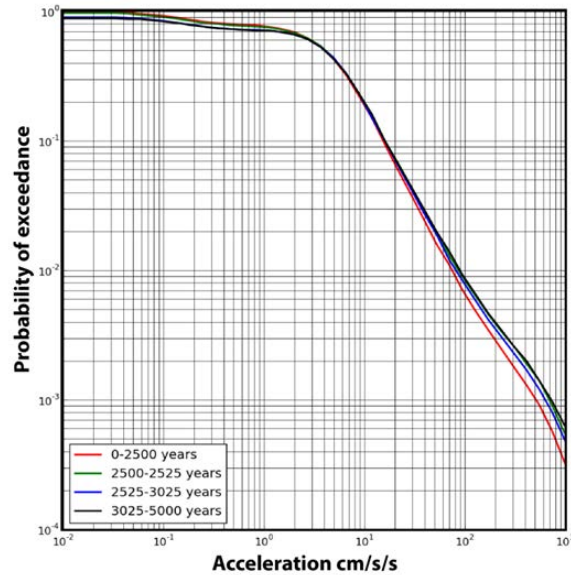
During and immediately following injection (2,500-2,525 years), and two post-injection intervals.

The hazard uncertainty for the 2,500-2,525 year time period is shown in Figure 41, which plots the mean and the 15%, 50% (median) and 85% percentile hazard curves based on the 150 catalog realizations. The range of uncertainty between the median and mean curves and the upper uncertainty bound is fairly typical of hazard curves in general. For example, the 50 cm/s/s hazard more than doubles from a mean value of 0.02 (0.50% in 25 years) to 0.047 (1.2% in 25 years) at the 85th percentile. The upper bound likely would be significantly higher if the uncertainty distributions in all of the seismicity simulation and ground motion parameters had been sampled. The upper bound hazard is governed both by relatively large events and by smaller events located at short distances from the surface site. The very large differences between the mean and median and the 15% lower bound, and the irregularity of the 15% curve are due to the large variation in the production of small micro-earthquakes among the realizations, and hence in the rates of occurrence of ground motions on the order of 10 cm/s/s or less, below the nuisance threshold. This variation is caused by the different possible combinations of the rate-and-state parameters.

Figure 42 shows the risk resulting from the mean hazard for the four time periods (Figure 40). The risk (annual probability of exceedance) at the 50% nuisance level for all of the time periods is approximately 0.13 (3.25% in 25 years). Towards the lower and upper end of the nuisance range, the risk at the 20% and 95% levels, are approximately 0.31 (7.75% in 25 years) and 0.02 (0.5% in 25 years), respectively. As expected from the hazard curves, there are only small increases in the nuisance risk during and immediately after injection, the maximum increase in risk above the pre-injection background being about 10%.

67

Figure 41: Mean, Median, 15% and 85% Hazard Curves for the Surface sites
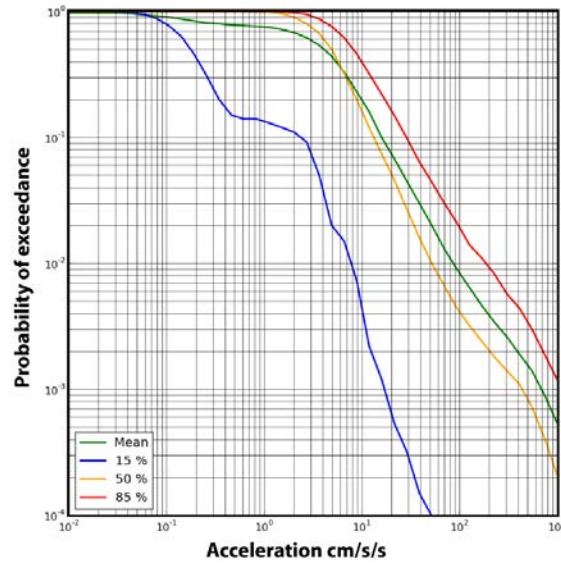
For the surface site for the 2,500-2,525 year period of elevated pressure at the faults.

Figure 42: Risk of Nuisance Curves Corresponding to the Mean Hazard in Figure 40 for the Four Time Periods
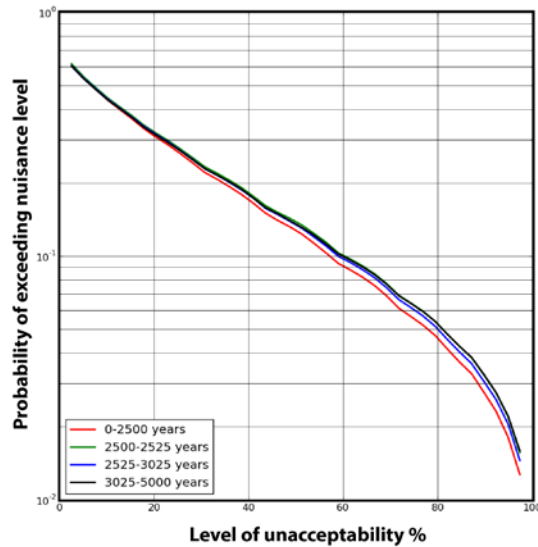
6.5: Discussion of Probabilistic Seismic Hazard and Risk Results

The overall conclusion from the demonstration PSRA is that the background hazard and risk at the King Island site are low, as might be expected from the low rate of deformation in the estimated tectonic setting. There is a modest increase in the hazard during and after injection, but these translate to only small increases in risk at all levels of nuisance. The risk of damage even at a site close to the two active faults is very low. The CO_2 injection rate of 8 Mt/year chosen for the demonstration is about double that for the largest GCS projects currently planned, but may be

representative of future industrial-scale projects. Although the results could provide some preliminary insight into the level of risk that might be expected at injection sites in similar tectonic settings in California, the earthquake frequency-magnitude distribution in the simulated seismicity catalogs depend on parameters in the rate-and-state frictional law that are presently poorly constrained at field scale. Therefore, studies that simulate the seismicity actually observed at well-characterized fluid injection sites will be crucial for parameter calibration and validation before the simulation-based approach can be applied with confidence to assess the potential risk associated with future GCS projects.

CHAPTER 7: Experimental Investigation Of Caprock Integrity

7.1: The Importance of Caprock Integrity to CO_2 Storage

The integrity of the caprock formation(s) overlying a CO_2 storage reservoir is vital for the viability of a GCS system. Failure of the caprock seal can result in CO_2 releases to the atmosphere, and contamination of shallow underground sources of drinking water by both CO_2 and in situ brine (and possibly other fluids such as oil or gas) mobilized by increased subsurface pressure. Faults are one type of potential leakage pathway. This project is concerned specifically with the potential for fault leakage caused by changes in fault permeability resulting from shear displacement during earthquakes. It has been proposed that earthquake-induced leakage poses a significant risk for long-term GCS in particular (Zoback and Gorelick, 2012), but this is the subject of ongoing debate (Juanes et al., 2012; Vilarrasa and Carrera, 2015; Zoback and Gorelick, 2015).

Fault permeability in general and slip-related permeability changes in particular are not yet well understood. This is especially true for faults in typical shale caprocks, at either field or laboratory scale. This Chapter describes an experimental investigation of shear slip-related permeability changes on a synthetic fault in a shale core sample, which is believed to be one of the first of its kind.

7.2: Experimental Objectives

Direct shear experiments were conducted on an induced single fracture within a shale core sample. These experiments simulated the mechanical and hydrological responses of a fault in a shale caprock to pore pressure changes and shear slip resulting from injection of supercritical CO_2.

7.3: King Island Caprock and Reservoir Core Samples

As discussed in Section 2.2, one of the reasons that the PAC recommended focusing on King Island as a demonstration site was the availability in house at LBNL of 20 feet of whole core from the Nortonville shale. Whole core is also available from the Upper Mokelumne River sandstone, and sidewall samples from the other storage and caprock formations.

Although the Nortonville shale core was preserved using the CoreSeal™ procedure, initial X-ray CT scans (Figure 43) revealed that the quality of the core is generally poor, and only three samples were identified as possible candidates for direct shear experiments. However, the poor quality of the samples meant that machining them would be very difficult, and beyond LBNL in-house capabilities. The possibility of having the Lawrence Livermore National Laboratory (LLNL) machine the samples was explored, a satisfactory arrangement for funding the work could not be found.

Figure 43: X-ray CT Images of Nortonville Shale Core
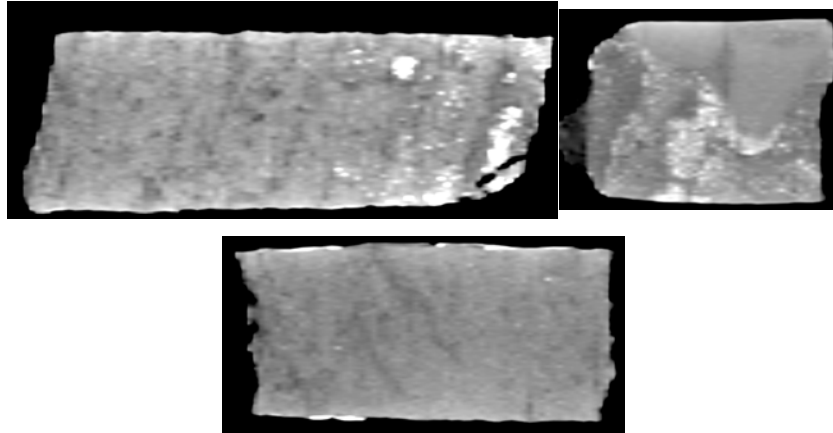
Core diameter ~2.5 inches.

As an alternative, the Energy Commission agreed that high-quality core of Opalinus Clay from Mont Terri in Switzerland could be used for the experiments. The Mont Terri clay is a shale that is similar in composition to certain caprocks of interest in California in that it has a significant swelling clay content. Compared with the 5-20% swelling clay content of the Mont Terri sample, very preliminary analyses indicate that the Nortonville and Capay shales have total clay contents of >25% and 5-25%, respectively; however, it not yet clear what proportion of these are swelling clays. The Mont Terri samples were successfully machined in-house at LBNL.

7.3: Experimental Setup and Procedures

The experiments were conducted under a stress state thought to be representative of the in situ stress at the depth of the Capay shale under King Island. The injected pore fluid was simulated brine with a composition based upon the Mont Terri in situ fluid chemistry for the Opalinus Clay sample. A single tensile fracture induced in the sample was sheared under confining stress, and slip on the simulated fault and accompanying changes in permeability were measured.

7.3.1: Rock Sample Preparation

The available Opalinus clay cores were semi-dry, with a water content of 2.2–3.2 wt%, compared to an estimated in situ water content of 6.6 wt% (Bossart, https://www.mont-terri.ch/en/geology%20/properties-and-characteristic-values.html). Even with this low water content, the samples were highly ductile. The presence of microcracks and silica inclusions meant that the samples were very heterogeneous and had a strongly anisotropic bedding texture. Because of these properties, preparation of the core samples for the experiments was difficult. To avoid the rock-water interaction that occurs during conventional coring, the required cylindrical geometry of the test cores was achieved by milling existing oversized cores down to the desired diameter of 2 inches. The length of the samples was four inches. Brazilian loading was used to induce a single tensile fracture along the core axis. In some cases, the strong interactions between the fracture and the rock texture resulted in non-planar fractures and disintegration of the cores

(Figure 44). For the experiments reported here, one of the samples that fractured relatively successfully was used. Minor damage (unwanted fractures) was repaired with low-viscosity epoxy.

Figure 44: Preparation of Rock Samples for Direct Shear Experiments

Unsuccessfully fractured samples (non-planar fracture and disintegration of the core) (*top*). Core used for the experiment (*bottom*). Core diameter 2 inches. The induced fracture is normal to the bedding plane. A fracture that was inadvertently formed parallel to bedding was repaired using epoxy.

Tto select the pore fluid used in the experiment, a series of simple rock-water interaction tests were performed by soaking small chips of the Opalinus Clay in different fluids at room temperature. The fluids included distilled water, 1% $NaCl_{aq}$, 10% $NaCl_{aq}$, 7% KCl_{aq}, 20% KCl_{aq}, 100% isopropyl alcohol, and a synthetic brine. The composition of the synthetic brine was based upon the "best estimate" values for the ionic composition of the in situ brine at Mont Terri given in Bossart's report. The brine was synthesized by dissolving the amount of the salts shown in Table 6 in distilled water. Only the concentrations of major cations (Na, Ca, and Mg) were matched.

With an exception of those soaked in isopropyl alcohol, all of the samples exhibited severe swelling and slaking due to clay expansion (Figure 45), although slightly less expansion was observed for the 20% $NaCl_{aq}$ case. Given the results of these tests, it was decided that there would be no advantage to using any solution other than the simulated Mont Terri brine for the pore fluid in the experiment.

Table 6: Composition of Synthetic Brine Used in the Experiment

Salt	Concentration g/L
NaCl	14.34

CaCl$_2$	1.686
MgCl$_2$	1.626

Figure 45: Swelling and Slaking of Rock Chips Exposed to Different Type of Fluids
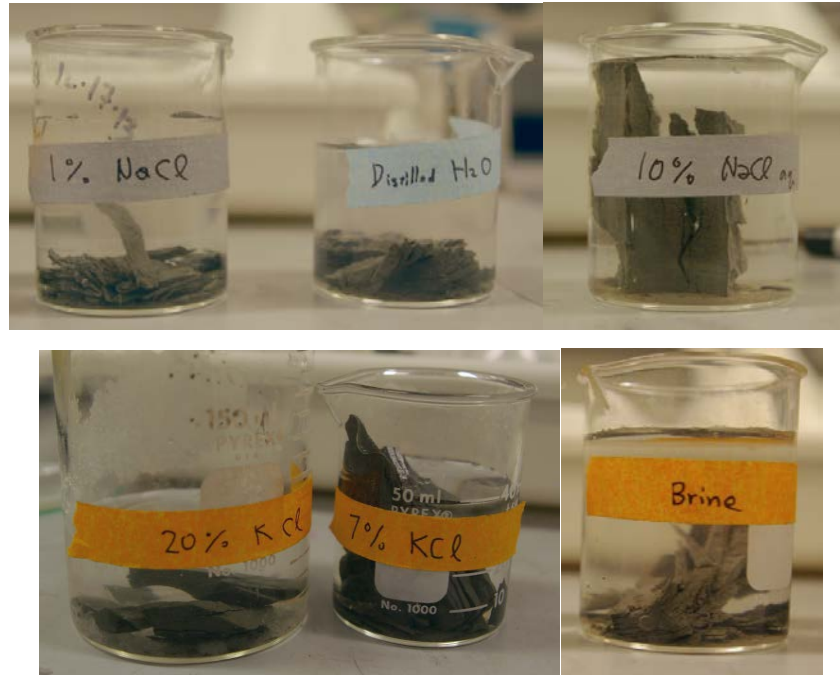
Although the KCl solution with the highest concentration (~20%) slowed the process, all the fluids tested caused swelling and disintegration of the Opalinus Clay chips.

7.3.2: Triaxial Direct Shear Test Method

LBNL has developed an experimental setup that allows direct shear experiments on single fractures to be conducted using a traditional (cylindrical) triaxial compression test system. Similar systems, based upon slightly different operating principles, have been developed by both the National Energy Technology Laboratory and Los Alamos National Laboratory. To apply shear loading to the single fracture plane in the current experiment, the system uses a half-split loading stage at each end of the sample, the seam between the two halves being aligned with the fracture. Axial loading is applied directly to the sample on one side of the fracture, while it is transmitted to the other half through a compliant elastometric spacer and mobile metal platen (Figures 46, 47). The stage assemblies at the two ends of the sample are rotated by180° with respect to each other; i.e., the elastometric spacers at either end are on opposite sides of the

Figure 46: Three LBNL's Triaxial Direct Shear Experiment System
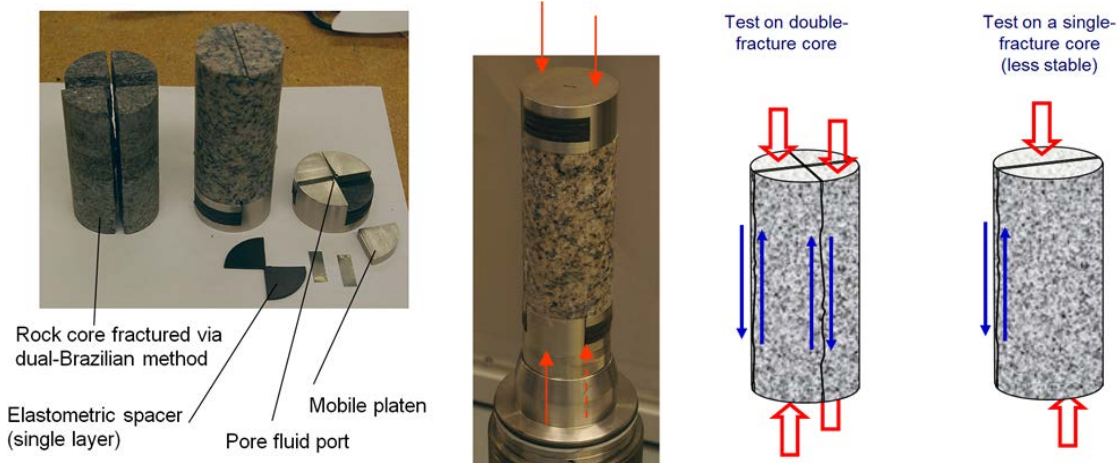
Quarter- or half-split end loading stages are placed at the top and bottom of a fractured cylindrical core sample. For doubly- and singly-fractured samples the loading stages at the two ends are rotated by 90° or 180°, respectively with respect to each other. The elastometric spacers behind the mobile platens transmit the confining stress applied to the jacket to the platens. (The example set up shown is from an experiment using a granite core.)

Figure 47: Current Experiment Using Loading Stages

Loading Stages at either end of the sample rotated 180° with respect to each other. The notched stainless steel shim in the picture is used to align the facture with the seam in the loading stage, and also to avoid the corner of the platen from catching the edge of the fracture.

fracture. Therefore, applied axial stress results in shear loading of the fracture plane as the stress applied to the directly loaded half of the sample at each end is greater than that applied via the spacer. Shear loading can also be applied to two orthogonal fractures using quarter-split platens. Greater shear stress can be applied to a single fracture, but the advantage of the dual-fracture arrangement is that the stiffness of the system is symmetric, which prevents possible rotation of the sample during shearing.

The permeability of the fracture(s) can be determined by flowing fluid between an inlet hole in the end plug at one end of the sample and an outlet hole at the other. Grooves (0.8 mm aperture) that

offset the edges of the fracture by 5 mm from both ends of the sample distribute injected pore fluid across the fracture plane. The grooves were also used to guide tensile fracturing during the Brazilian loading and to avoid interference between the platen and the fracture during shearing. The stainless steel shim seen in Figure 47 is used to align the facture with the seam in the loading stage, and also to avoid the corner of the platen from catching the edge of the fracture during displacement.

The nominal normal and shear stresses on the fracture(s) can be computed by

$$\sigma_N = \sigma_r \tag{7.1}$$

$$\tau = \left(\sigma_a - \sigma_r\right)\frac{\pi a}{2nh} \tag{7.2}$$

where σ_r and σ_a are the radial confining stress and axial stress, respectively, and a, n, h, are the core radius, number of fractures, and core length, respectively. Combinations of the normal and shear stresses achievable using the current system are shown in Figure 48.

The sample assembly including the end plugs is first jacketed in a thin latex membrane followed by a 0.5 mm-thick FEP heat shrink tubing, and then inserted into a ¼ inch-thick Viton sleeve. The semi-rigid FEP tubing is used to reduce penetration of the Viton sleeve into the fractures under elevated confining stress. To reduce the constraints on the core deformation by the FEP tubing, rows of cuts were made along the length of the jacket surrounding the fracture.

7.3.3: Experimental Setup

The experimental setup is shown in Figure 7.6. The jacketed sample assembly is installed inside a triaxial testing holder (Temco/Corelab triaxial test cell), as shown in the top-right panel of Figure 7.6, which is capable of applying axial and radial (confining) stresses of up to 10,000 psi (69 MPa: 1 psi=6.895x10^{-3} MPa) independently. During an experiment, each of the stresses is controlled by a dedicated syringe pump. Pore pressure and fluid flow in the sample are controlled by an upstream injection syringe pump and a backpressure regulator on the downstream side, controlled in turn by yet another syringe pump (Figure 7.6, top-left and bottom). The fluid pressure drop across the sample is measured using a differential pressure transducer. The axial displacement of the piston applying shear stress on the sample is measured using an LVDT (linear variable differential transducer) attached to one end of the core holder. Additionally, acoustic emissions from the sample are monitored using two sensors attached to the inlet and outlet tubing extending from the core holder ends.

Figure 48: (Nominal) Normal and Shear Stresses Applied Using the Direct Shear Device
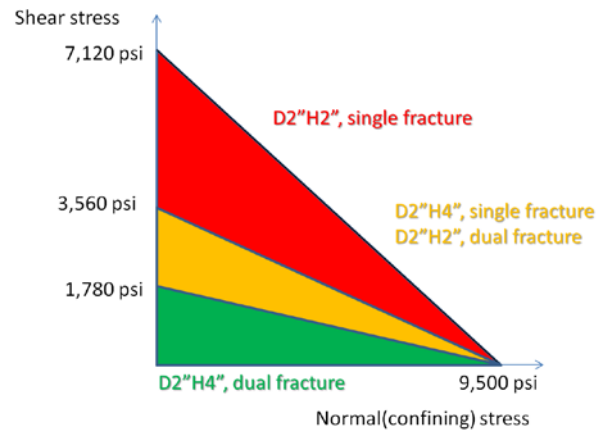
The maximum magnitude of the shear stress is determined by both fracture (core) length and the number of the fractures being sheared. 1 psi=6.895x10-3 MPa.

Figure 49: Experimental Setup
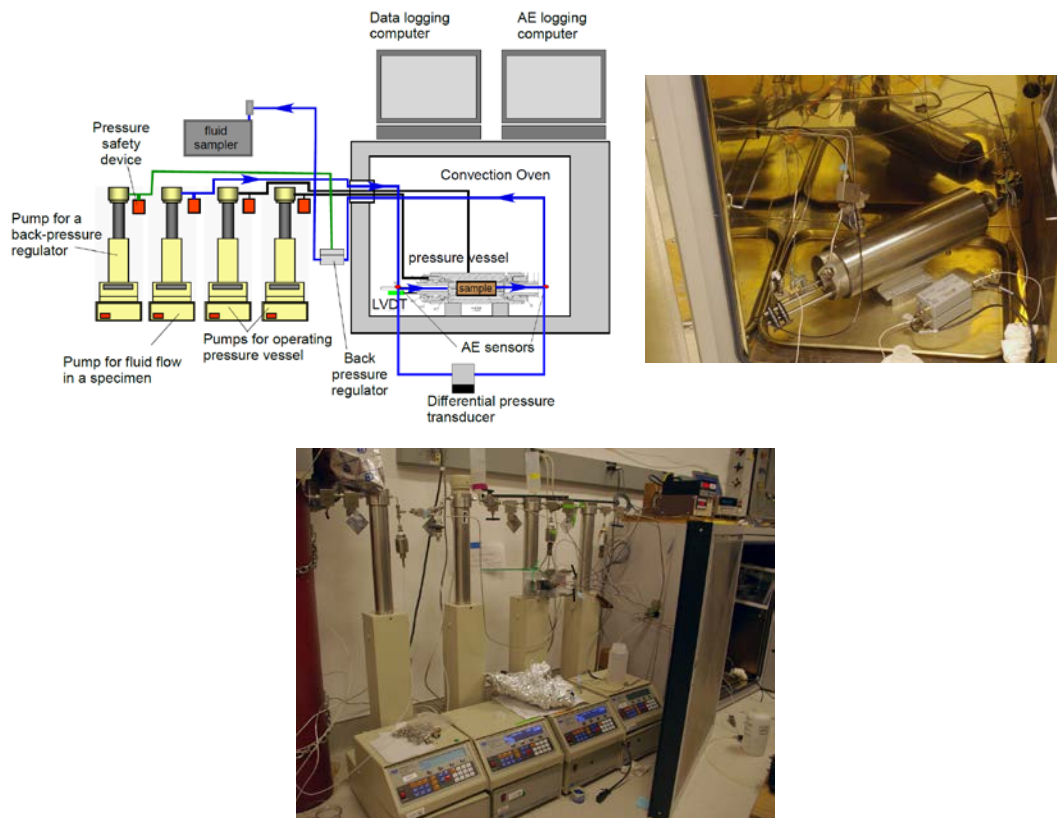
Test system schematic (top left); triaxial testing cell (top right); Syringe pump stack (bottom).

7.3.4: Loading Protocols

To select the initial normal and shear stresses that should be applied to the fracture during the test, it was assumed that the orientation of the fracture is given by the shear failure plane of intact

76

Opalinus Clay. From Bossart's report, the Opalinus Clay has an average cohesive strength of 3.6 MPa (522 psi) and an average internal friction angle of 24°, giving a hypothetical fracture orientation of 57° from horizontal. The normal and shear stresses on the fracture were then estimated from the failure envelope of the Opalinus Clay based on estimated maximum and minimum principal stresses at the depth of the Capay Shale under King Island of 3,700 psi and 2,800 psi, respectively. This yielded normal and shear stresses of 3,067 psi and 353.2 psi, respectively. From Eqs. 7.1 and 7.2, the corresponding axial stress for a 4 inch-long sample is 3,966 psi. In the experimental design, the pore pressure is increased under these stress conditions until the fracture is activated and slips. The estimated pore pressure necessary to activate the fracture is 2,124 psi. (Note that this value applies after the fracture has been activated and a gouge zone has developed. For the initial, mated fracture, the pressure may be higher due to the larger friction angle of the interface and also due to different principal stress orientations.)

7.3.5: Test Sequences

The experiment was conducted in two test sequences (Table 7 and Figure 50). The objective of the first sequence was to activate the fracture by increasing the pore pressure under constant normal and shear stress loading. A high hydrostatic stress (3,067 psi) was first applied to the sample, and then the test system and the fracture were saturated with brine after a vacuum was applied. At this point, little resistance to flow was observed under a pore pressure of 100 psi.

After an overnight interval, two fracture activation tests were conducted. The first test was conducted under a constant nominal shear stresses of 177 psi by increasing the pore pressure to a peak value of 2,295 psi. The pore pressure was then reduced to 100 psi and the nominal shear stress increased to 354 psi. After an overnight break, the second test was conducted at the constant shear stress of 354 psi by increasing the pore pressure to 2,994 psi. Following the second test, the fracture was activated by increasing the shear stress to a peak value of 1,197 psi while the pore pressure was 2,124 psi, close to its expected critical value. Lastly, after applying high pore fluid pressure (3,000 psi) to the sample overnight, all the stresses and the pressure were reduced to ambient. After the first loading sequence, the sample was taken out of the core holder, and examined using X-ray CT before removing the jackets. The results are discussed in Section 7.4 below. Subsequently, the sample assembly was placed back in the core holder, and the second test sequence was initiated.

In the second sequence, the same fracture was activated by applying large shear stresses. After an initial increase in the hydrostatic confining stress to 3,067 psi, the sample was vacuum saturated. The pore pressure was increased to slightly below the estimated pressure required to activate an open fracture (2,049 psi) under the estimated in situ stress state. Subsequently, the shear stress was increased to a peak value of 1,248 psi and the fracture was activated until a little over 4 mm of axial (shear) displacement was achieved. The sample was again taken out of the core holder, and examined using X-ray CT before removing the jackets.

Table 7: Test Sequences

I. First sequence

1) Initial hydrostatic loading ($\sigma_r = \sigma_a$ =3,067 psi)
2) Apply vacuum to the system. Saturate the system with synthetic brine
3) Increase pore pressure to 100 psi.
4) Overnight break
5) Increase axial/shear stress (σ_a up to 3,518 psi; τ □□□□□□□psi)
6) Pore pressure loading (up to 2,295 psi)
7) Reduce pore pressure to 100 psi
8) Increase axial/shear stress (σ_r= 3,067 psi up to σ_a up to 3,966 psi; τ □□354□psi)
9) Overnight break
10) Pore pressure loading (up to 2,994 psi)
11) Reduce pore pressure to 2,124 psi (expected critical pore pressure)
12) Shear loading (σ_a=6,114 psi; τ □□□1,197□psi. Axial displacement up to ~1mm,)
13) Reduce axial/shear stress (σ_a =3,966 psi; τ □□354□psi)
14) Overnight break
15) Pore pressure loading (up to 3,000 psi)
16) Pore pressure maintained overnight
17) Reduce all stresses/pressure to ambient

II. Second sequence

1) Initial hydrostatic loading ($\sigma_r = \sigma_a$ =3,067 psi)
2) Apply vacuum from both ends of the sample. Saturate the system with brine.
3) Increase pore pressure up to 100 psi, then to 2,049 psi
4) Overnight break
5) Shear loading (σ_a=6,245psi; τ □□1,248□psi. Axial displacement up to ~4.2 mm)
6) Reduce all stresses/pressure to ambient

---

1 psi=6.895x10^{-3} MPa

7.4: Experimental Results

7.4.1: Mechanical Response

The entire history of the stresses and pressures applied to the fracture in the Opalinus Clay core sample and the resulting axial/shear displacements are shown in Figure 50. Note that because the reduction of the fracture contact area by the two grooves described in Section 7.3.2 was not considered, the resulting normal and shear stresses were both slightly higher than originally planned.

Figure 50: Loading History and Resulting Axial/Shear Displacements
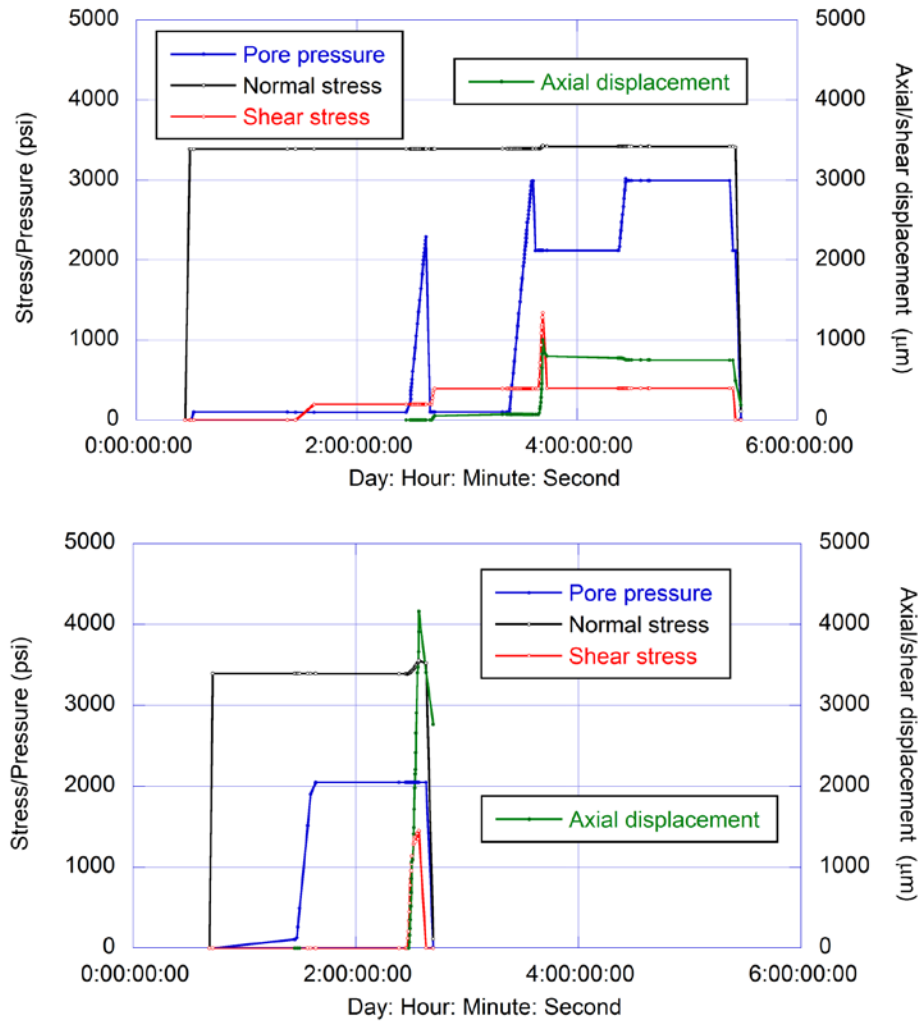
Loading sequences: (top) Sequence I; (bottom) Sequence II.

Remarkably, none of the tests to activate the fracture by pore pressure increases (Sequence I, tests 6,10 and 15 in Table 6) resulted in shear slip along the fracture, even when a high pore pressure near to the confining stress was applied to the sample and after the sample had been kept under the elevated pore pressure overnight. No measurable acoustic emissions were detected during the pore pressure loading tests. In contrast, the fracture did slip when a high shear stress was applied (~1 mm displacement for Sequence I, test 12 and ~4.2 mm for Sequence II, test 5). Part of the observed displacement (~100 μm for I12 and ~1.4 mm for II5), however, reversed when the shear stress was reduced, which is attributed to elastic deformation in both the sample and the test system.

Images of the core samples after the first and second loading sequences (Figure 51) indicate ductile flow and swelling of the shale at the ends of the sample. In particular, the grooves at the edges of the fracture were completely filled with clay. Additionally, after the second loading sequence, one side of the core's end surface was severely damaged, indicating shear failure within the rock matrix.

79

Figure 51: Photo Images of the Ends of the Sample After Each Loading Sequence
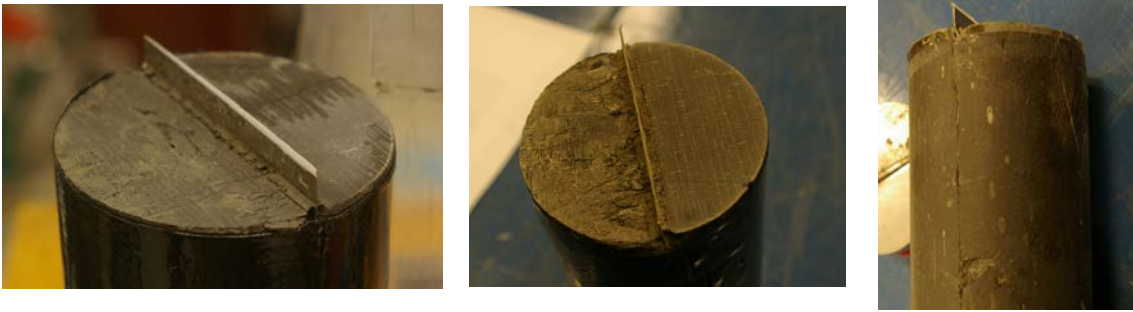
After Sequence I (left); after Sequence II (center and right).

7.4.2: Hydrological Responses

After the initial introduction of pore fluid into the sample, the fracture permeability was almost completely lost. (Note that the minimum measurable flow rate at differential pressures less than 8 psi was ~2 x 10^{-4} mL/min due to a very small fluid leak in the system.) This was also the case even after large shear displacements had been applied to the fracture.

The post-experiment X-ray CT images shown in Figure 52 (linear projection images from one side of the fracture) and in Figure 53 (sequential, tomographic images along the length of the core) revealed that the originally open fracture was mostly closed and filled with expanded clay. From the images, the fractures are slightly more open near the center of the sample. This may be because once the fracture near the edges of the sample closed, the fracture surface near the center had no more access to the pore fluid, which stopped or reduced further clay swelling and fracture closure. The fracture stayed closed even after the large shear displacement applied during the second loading sequence. However, in this case the fracture towards the center of the core appeared to be slightly more open.

7.5: Interpretation and Discussion of Experimental Results

The direct shear experiments were designed to measure changes in the permeability of the simulated fracture due to different amounts of imposed shear slip. However, because of the high ductility and high water-sensitive, swelling clay content (possibly bentonite/montmorillonite) of Opalinus Clay, the fracture totally lost permeability immediately after pore fluid having a chemical composition similar to that of the in situ brine at Mont Terri was introduced in the sample. The result of this was that, under an applied stress state estimated to be representative of in situ stress at the depth of the Capay Shale under King Island, externally applied pore pressures well above the estimated critical pressure for fault activation (but less than the hydraulic fracturing pressure) failed to activate shear displacement on the fracture.

Figure 52: Linear X-ray Scan Images of Jacketed Fractured Opalinus Clay Core
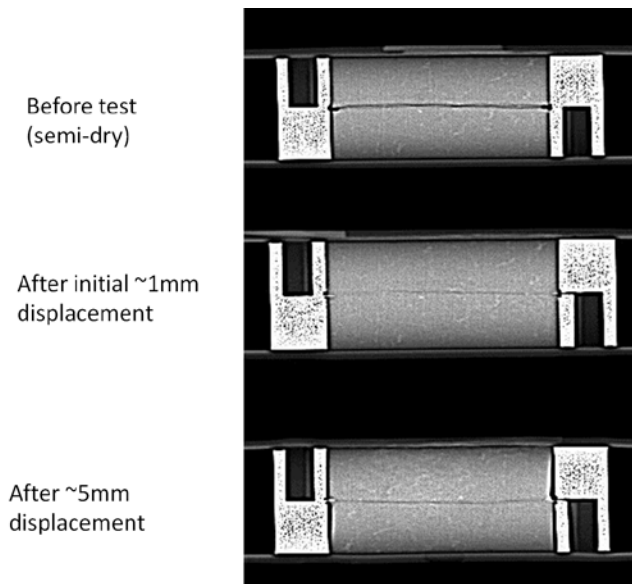
The initially open fracture closed due to ductile deformation and swelling of the shale during both loading sequences. Note that the grooves at the ends of the fracture are completely filled. After 4.2 mm of shear displacement in the second loading sequence, the fracture has a slightly larger aperture towards its center. (Note the split end stages used for applying the shear displacements are visible in these scans.)

The shear displacement observed during the second loading sequence of the experiment was attributed primarily to shear failure within the rock matrix, rather than to fluid pressure-assisted slip on the fracture. The loss of fracture permeability was exacerbated by the configuration of the experiment, including clogging of the pore fluid ports and grooves at the ends of the fracture. However, the experiment demonstrates the strong influence that plastic deformation and swelling of the clay-rich shale can have on its hydrological properties, and consequently on the mechanical strength of fractures and faults. This self-healing effect has important implications for the leakage potential along faults within the cap rock of a CO_2 storage reservoir.

Figure 53: X-ray CT Scans of Jacketed, Fractured Opalinus Clay
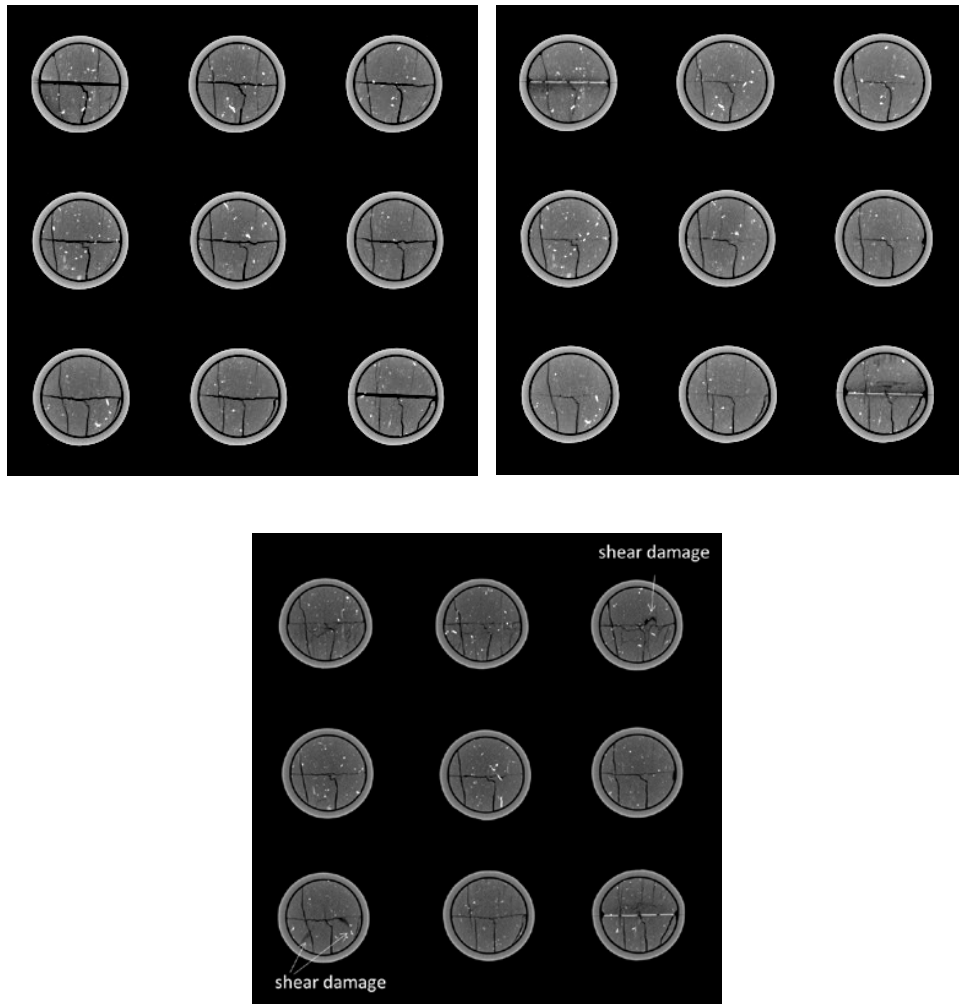
Initial scans (top left); after first loading sequence (top right); after second loading sequence (bottom). The black sub-vertical linear features are preexisting fractures that were filled with epoxy before the experiment. The bright white lines on the fracture in the first and last images in the top right panel and the last image in the bottom panel are stainless steel shims. In all of these images the fracture, particularly near the edge of the core, is tightly closed, resulting in the loss of overall fracture permeability. The images after the second sequence also show shear damage and additional fracturing of the core matrix.

CHAPTER 8: Technology Transfer: Regulatory Implications

8.1: Background

There have been several attempts in California to permit small-scale CO_2 injections (on the order of a few thousand tons) to be performed as experimental projects and precursors to large, commercial-scale storage projects. Induced seismicity typically has been included in permitting considerations, albeit via different approaches. The issue of induced seismicity caused by GCS has also been raised during legislative hearings and in proceedings convened by several of California's regulatory agencies, but there appears to be no clear consensus as to what technical data, monitoring, or mitigation plans should be required neither of project developers nor of how induced seismicity should be incorporated in forthcoming CCS regulations. The findings of this study provide information to significantly improve the knowledge basis on which to develop a consistent regulatory approach.

8.2: California's Permitting Process

Large, commercial-scale CCS operations are industrial development projects, elements of which crosscut the regulatory authority of various California and federal agencies. The existing permitting process for industrial development projects in California involves a multitude of federal, state, regional and local agencies, each with its unique authorities and regulatory requirements. The current regulatory framework allows a project developer to approach different agencies at different times to initiate permit applications and to begin to address the requirements of the California Environmental Quality Act (CEQA). The timing as to when a permit application is filed with each agency is the responsibility of the project developer.

The California Permit Streamlining Act of 1977 was enacted to address a complicated and often uncoordinated permit process by establishing a lead agency and a timeline with statutory deadlines for review and decision. This Act was intended to expedite government permitting of industrial development projects. Under the Act, if a public agency does not approve or deny a project within the statutory time limit, the project is deemed approved. The Act establishes that the lead agency must approve or deny a project within 6 months of certifying an Environmental Impact Report (EIR), or within 3 months of adopting a Negative Declaration. Other agencies, which are not the lead agency, must act within 6 months from the time a permit application is filed. The lead agency coordinates the permitting process with the environmental review process required by CEQA. The lead agency determines whether a project is exempt from CEQA or requires a negative declaration, mitigated negative declaration, or an EIR. It is the responsibility of the lead agency to involve other permitting agencies so that a coordinated environmental review results.

Developers of early projects and studies of existing regulatory processes show that about 15-20 different agencies have regulatory jurisdiction in California over various elements of a

commercial-scale CCS project. While some of the project elements may fall into overlapping areas of regulatory jurisdiction, other elements fall into gaps. Induced seismicity is an element that may fall into a gap unless an agency specifically opts to include it as an element to be reviewed. For example, in the permitting of the C6 Resources Solano County project, discussed further below, induced seismicity was called out by the Solano County agency tasked with issuing a land use permit. Recently, because of this gap, the Air Resources Board has considered whether regulations covering induced seismicity should be a necessary part of its selection protocols for CCS site eligibility to be considered under cap-and-trade and other GHG reduction regulations.

8.3: Federal Jurisdiction

The current overriding federal legislation that controls the injection of CO_2 is Part C of the Safe Drinking Water Act, which is the basis for the U.S. Environmental Protection Agency (EPA) Underground Injection Control (UIC) policies and regulations. The UIC policies are designed to ensure that injection activities do not contaminate underground sources of drinking water. There are currently six UIC classes, of which Class VI is specifically targeted at injection for CO_2 sequestration.

Class VI includes a combination of prescriptive and performance-based standards for monitoring internal and external mechanical integrity of the well(s), CO_2 plume migration away from the injection point(s), and the pressure front. While there is no explicit requirement for a seismic monitoring plan in the Class VI regulations, there are very prescriptive requirements for monitoring subsurface pressure. The internal integrity tests require use of continuous monitoring of "injection pressure, rate, injected volumes, pressure on the annulus between the tubing and long-stem casing, and annulus fluid during injection." (Code of Federal Regulations §146.89(b)). The external mechanical integrity test can be done in a variety of ways, but must be one of the mentioned tests, or approved in the permitting process. Plume and pressure front monitoring requirements are performance-based with the operator required to show a monitoring plan to ensure that the injectate is safely confined in the intended subsurface geologic formations and underground sources of drinking water are not endangered. In addition, there are some requirements that pertain to all wells and some that are site-specific.

Under Class VI, the monitoring plan should be designed to detect changes in "ground water quality and geochemical changes above the confining zone(s) that may be a result of carbon dioxide movement" (Code of Federal Regulations §146.90(d)) and to "track the extent of the carbon dioxide plume and the presence or absence of elevated pressure (e.g., the pressure front)" (Code of Federal Regulations §146.90(g)).   The plan must also show that the site is "operating as permitted and is not endangering USDWs" (Code of Federal Regulations §146.90)).The monitoring requirements cover the types of analysis that must be included (i.e., groundwater quality and geochemical changes above the confining zone), but do not specify the exact testing or location of monitoring. These should be based on the identification and assessment of potential CO_2 leakage routes complemented by computational modeling of the site (Code of Federal Regulations §146.90(d).

8.4: California CCS Review Panel

The California Carbon Capture and Storage Review Panel was convened to advise the California Energy Commission, the California Public Utilities Commission, the Air Resources Board, the Department of Conservation and other state agencies on CCS policy (California Carbon Capture and Storage Review Panel, 2010). On the issue of induced seismicity, the background reports for the Panel (California Institute for Energy and Environment, 2010) include the following summary statement:

> "Induced seismicity is another risk consideration during CO_2 injection operations. It is well recognized that injecting fluids into the subsurface can result in seismic events, although the vast majority of these are not recognized as earthquakes because they do not release enough energy to be felt at the surface. In fact, there is an entire technology associated with the use of these small events, called microseismic events, as a tool for monitoring the movement of fluids in the subsurface. Although rare, there have been instances in which non-CCS injection operations—including some engineered geothermal operations—have resulted in ground motion that was felt by near-by communities. Seismic risks therefore need to be taken into consideration during site selection and in the design, operation, and monitoring of CO_2 storage projects. The identification and proximity of active faults will need to be considered during site selection, and specialized seismic monitoring may be warranted as part of the overall monitoring, verification, and reporting (MRV) plan." (California Institute for Energy and Environment, 2010, p.2-8).

While the Panel itself did not make any specific recommendations as to the elements of an MRV plan that should be required for induced seismicity, the background reports make some specific recommendations. The Technical Advisory Committee to the Panel recommended that monitoring for induced seismicity should begin during the site selection and assessment phase with establishing a baseline record of the natural background seismicity in the region encompassed by the project, using the state's existing seismometer network augmented by a local network. During operations, changes from the natural background should be observed and direct monitoring of fluid pressures should be performed. Site selection should also involve "both identifying existing faults and evaluating the potential for damaging shaking that might result from an earthquake. Probabilistic seismic hazard analysis (PSHA), the methodology most commonly employed in California to do this, forms the framework for an approach to evaluate the change in seismic hazard, if any, due to a CO_2 storage project." (California Institute for Energy and Environment, 2010, p.21-6).

According to the Committee, the record of the natural background seismicity should be compared to data collected after injection begins. It is important to analyze both the time history and the magnitude of any events that occur. Instrumentation for "real time" measurement and analysis should be employed to facilitate immediate response to significant events. Importantly, the Committee emphasized that definition of what constitutes a "significant" event, as well as the mitigating actions that need to be taken in response to the event, should be part of the seismicity monitoring plan. Many factors affect the definition of a significant event. Geologic factors affect

the magnitude of shaking and the potential for damage of structures, but the sensitivity of the public to any seismicity that can be felt could also be a major factor.

8.5: CCS Permitting in California

8.5.1: Hydrogen Energy California

The Hydrogen Energy California (HECA) project was the first proposed power plant project using CCS technology to be submitted to the Energy Commission for licensing. HECA planned to capture emissions from an Integrated Gasification Combined Cycle power plant fueled by petroleum coke and coal. The process to be used produces electricity, hydrogen and urea fertilizer. The captured CO_2 from the facility originally was to be sold for enhanced oil recovery (EOR) in the Elk Hills oil field. However, HECA withdrew the project application in March 2016.

As part of the Energy Commission licensing proceeding for the power plant, and as the lead agency for CEQA, the proceedings included assessments as to how the power plant would meet the maximum allowable annual CO_2 emissions set by California statutes to meet California Assembly Bill 32 goals. Consequently, the amount of permanent storage to be accounted for by the EOR operations had to be established as part of the Commission's proceeding. Since the Division of Oil, Gas, and Geothermal Resources (DOGGR) regulates EOR under its Class II UIC primacy, the Energy Commission anticipated folding DOGGR requirements for EOR in the oil wells into its licensing proceedings for the power plant—an unprecedented and somewhat complex undertaking. Induced seismicity is not explicitly part of DOGGR's Class II rules; however, there are very clear rules regarding maximum allowable injection pressures based on results of formation and wellbore integrity tests.

8.5.2: C6 Resources Pilot Project in Solano County

C6 Resources, LLC (a wholly owned subsidiary of Shell Oil Company) was awarded a grant from the U. S. Department of Energy under the American Recovery and Reinvestment Act to examine the potential of commercial CCS for refinery CO_2 in the Montezuma Hills of Solano County. The setting is a rural area where surrounding lands are used for agriculture, grazing, open space and wind energy production. A geologic CO_2 storage pilot of about 6000 metric tons was planned, with sequestration into deep sandstone formations containing saline formation fluids. The pilot test planned to drill injection and monitoring wells 3,000-3,700 m deep. A baseline seismic monitoring study was undertaken and two local seismometers were installed for a short time at the proposed site.

In 2010, the permitting process for the project began with obtaining an experimental well UIC permit (Class V) from U.S. EPA, Region 9 and a conditional land use permit from Solano County. The U.S. EPA first needed to make a determination regarding the need for an Environmental Impact Statement under the National Environmental Policy Act, while Solano County, the local lead agency, needed to make the determination on whether an EIR was needed to satisfy CEQA.

In the proceedings for the land use permit, Solano County required investigation of the potential for induced seismicity. Lawrence Berkeley and Lawrence Livermore National Laboratories were asked to develop an independent assessment of the likelihood that the proposed 6000 metric ton injection would cause felt seismic events (Daley et al., 2010; Myer et al., 2010; Oldenburg et al., 2010). The Labs' study identified faults close to the injection site, examined seismic history, and summarized the results of simulations of the pressure response to injection. Results, summarized below, demonstrate the approach and gaps in knowledge that affected the uncertainty in the findings.

The closest known fault to the proposed injection site is the Kirby Hills Fault. Shell's proprietary seismic survey data also indicated two unnamed faults about 5 km east of the project site. These faults do not reach the surface as they are truncated by an unconformity at a depth of about 600 m. The unconformity is identified as occurring during the Oligocene Epoch, 33.9–23.03 million years ago, which indicates that these faults are not currently active. Farther east are the Rio Vista Fault and Midland Fault at distances of about 10 km and 16 km, respectively. These faults have been identified as active during the Quaternary (last 1.6 million years), but without evidence of displacement during the Holocene (the last 11,700 years).

The Kirby Hills Fault is probably the site of micro-earthquakes as large as magnitude 3.7 over the past 32 years. Most of these small events occurred 15-28 km below the surface, which is deep for this part of California. However, attributing recorded earthquakes to specific faults using data from events in the standard seismicity catalog for the area is subject to considerable uncertainty because of the lack of nearby seismic stations. Since the study determined that installation of local seismic monitoring stations near the site would greatly improve earthquake location accuracy, two seismic stations were installed at the proposed site soon after the report was completed to gather baseline seismicity data prior to beginning injection operations (Daley et al., 2010). Interestingly, the deployed local seismometers picked up extensive background microseismic noise caused by the large number of wind turbines in the area.

The stress state (both magnitude and direction) in the region is an important parameter in assessing earthquake potential from injection activities. Although the available information regarding the stress state is limited in the area surrounding the injection well, the azimuth of the mean maximum horizontal stress is estimated at 41° and it is consistent with strike-slip faulting on the Kirby Hills Fault, unnamed fault segments to the south, and the Rio Vista Fault. However, there are large variations (uncertainty) in stress estimates, leading to low confidence in these conclusions regarding which fault segments are optimally oriented for potential slip induced by pressure changes. The study suggested that the uncertainty in the stress state should be reduced by making in-situ stress measurements once the wells were drilled at the site.

The injection of 6000 metric tons would result in a reservoir fluid pressure increase greatest at the well and decreasing with distance from the well. After the injection stops, reservoir fluid pressures would decrease rapidly. Pressure changes were predicted quantitatively by numerical simulation models of the injection (Oldenburg et al, 2010). Based on these models, the pressure increase on the Kirby Hills Fault at its closest approach to the well due to the injection of 6,000

metric tons of CO_2 would be a few pounds per square inch (psi), which is a tiny fraction of the natural hydrostatic pressure of approximately 5,000 psi (35.5 MPa) at 3,700 m depth. The likelihood of such a small pressure increase triggering a slip event is very small. It is even more unlikely that events would be induced at the significantly greater depths where most of the recorded earthquakes are concentrated, because it is unlikely that such a small pressure pulse would propagate downwards any appreciable distance.

The Solano County regulators specifically framed the induced seismicity question as "What is the likelihood of the CO_2 injection causing a magnitude 3.0 (or larger) event?" The Lab's analysis suggested that no such induced or triggered events would be expected. However, it is possible that a fault, too small to be detected by the existing seismic data, yet sufficiently large to cause a magnitude 3.0 event, could exist in closer proximity to the injection point where the pressure increase could cause slippage. However, the existence of any such faults would be detectable by data collection from the well prior to injection. It should be noted that natural earthquake events of up to 3.7 in magnitude have occurred in this area and would be expected to occur again regardless of the proposed CO_2 injection.

The EPA and Solano County permits were withdrawn in late 2010 after Shell determined that the project did not fit into its international portfolio of strategic projects. The local seismometers were uninstalled.

8.5.3: Kimberlina

An EPA Class V permit for a small-scale CO_2 injection into a saline formation was submitted in 2008-2009 for a site near Bakersfield, California. Clean Energy Systems planned to inject about 10,000 metric tons of CO_2 into the Vedder Formation at a depth of about 2,400 m. This was to be a pilot for a commercial-scale injection of about a million metric tons over four years. No explicit predictions of induced seismicity potential were required as part of the permit application. However, simulations of the pressure response due to the large-scale injection were included. The lateral extent of the pressure response to CO_2 injection showed rapid decline with distance from the injection well, and over time once injection stopped. The profiles of pressure change in the uppermost layer of the storage formation complex showed that the pressure response extends far beyond the CO_2 plume, which is limited to about 1 km, but the pressure response beyond the CO_2 footprint drops quickly to less than 0.15 MPa. Moreover, the pressure response decreases as distance from the injection well increases, and quickly dissipates after four years when injection ceases. Fault patterns and locations in the area are poorly constrained; based on available data, the pressure front appears unlikely to intersect any significant active faults.

8.6: Air Resources Board Protocols for CCS

The California Air Resources Board (ARB) CCS QM will need to establish a protocol that accurately accounts for GHG emission reductions and provides confidence in the permanency of

those reductions. To achieve this, the QM will need to include criteria, specifications, or other requirements to ensure selection of a proper injection site that minimizes the likelihood of potential CO_2 surface leakage and maximizes CO_2 trapping in the underground target storage complex. Assessing the potential for induced seismicity and associated fault leakage and establishing monitoring requirements are important elements in site selection and certification of storage permanence. To date, this study provides the best technical basis for formulating site data and monitoring plan requirements.

The Air Resources Board has commissioned LBNL to provide technical assessments of storage site characteristics likely to affect storage permanence. These assessments will inform ARB as it establishes GCS site selection criteria that must be met in order for stored CO_2 to be eligible as a reduction compliance method under cap-and-trade and other greenhouse gas reduction mechanisms. The site selection criteria are primarily focused on elements that affect leakage risk associated with wells and geological features—including faults and fractures. In consideration of the gap in current regulations and the association of induced seismicity with potential fault leakage, the Board also asked for the technical assessment to include induced seismicity risk.

This study provides an approach to GCS induced seismicity risk that forms a basis for informing future regulations, including site criteria and monitoring strategies for the ARB study. The full risk assessment procedure described and demonstrated in this report would require a project developer to carry out the following steps:

1) Provide a review of known faults and historic seismic activity extending over the maximum area predicted to be affected by the pressure response (the "pressure area of review" or PAR), which may be the same as the area of review (AOR) under the EPA's permitting requirements.
2) Provide available data on fault characteristics and geophysical properties of the relevant formations.
3) Perform simulations of the pressure effects created by the planned injection volume and rate.
4) Perform baseline monitoring by installation of a local monitoring seismometer network ideally, for a year or more prior to commercial-scale injection.
5) Perform measurements of in-situ stress, seismic velocities, hydrological and geomechanical properties, etc. in any existing nearby wells and in the injection and/or observation wells when they are drilled.
6) Simulate multiple realizations of induced seismicity catalogs based on the predicted pressure history and constrained by the measurements of in situ properties, and perform a probabilistic hazard and risk analysis.
7) Compare field data over the lifetime of the injection operation and post-operation monitoring to the simulated catalog and refine the simulations and hazard estimates based on improve history matching.

In practice, in the context of the current aim of the ARB QM to address leakage risk, it is unlikely that the comprehensive site characterization needed for a full probabilistic risk analysis will be required to fulfill ARB's site criteria for every project. Initial, low-level assessment during site screening could be used to place each site into one of a few induced

seismicity and leakage risk categories (e.g., low, moderate, high) using the following criteria based on Steps 1 to 4 above:

- Planned injection rate, cumulative volume, duration, and depth.
- Distance from active or potentially active faults (Steps 1,2).
- Existence of potential high-permeability pathways between the injection well and known faults (1,2)
- Preliminary estimation of pressure changes on nearby faults (3).
- Background seismicity (1, 4).

Criteria and monitoring requirements for a site in one of the moderate- or high-risk categories would be based on a level of hazard and risk assessment determined to be appropriate for that category. For example, future ARB siting and monitoring criteria could require developers of very large scale and/or high-risk projects to carry out extensive site characterization and full probabilistic risk analysis, whereas a less detailed characterization and perhaps a deterministic analysis based on limited simulations may be sufficient for moderate-risk projects. A higher level of site characterization, monitoring, analysis and modeling will be appropriate for projects having a large research component funded by federal or state agencies, which will add to the fundamental understanding of induced seismicity and its associated risks.

Currently, with its focus on the relationship of induced seismicity to leakage, the ARB study has proposed the following language (as of March 10 2017):

> Risk of induced seismicity: An interval with sufficient transmissivity and capillary entry pressure to fully dissipate overpressure along any hypothetical leakage path hydraulically connected to it exists between the storage zone and crystalline rock over the PAR.

This statement approaches the issue from the standpoint of how to select a site that is least likely to experience any induced seismicity that would indicate potential leaky faults. The underlying assumption here is that a fault that experiences slippage also is a likely conduit for leakage. The findings of this study support this notion, at least for larger faults that penetrate the caprock seal.

ARB is also considering criteria to minimize the risk of fault leakage. The key site characteristic is the ability of the shales to make faults sealing rather than transmissive. The following language is under consideration (as of March 10 2017):

> Likelihood of leakage via geologic pathways: For the portion of storage proposed in a saline aquifer, the proposed seal is sufficiently ductile within the CO_2 AOR that potential fractures and faults have annealed.

This demonstrates the application of the laboratory findings of this study—which showed how the ductility of the clay minerals present could make a fault or fracture more resistant to failure (and presumably to leakage) than the surrounding rock.

CHAPTER 9: Conclusions

The study discussed in this report investigated the potential for induced seismicity and associated fault leakage related to GCS in California. Following the recommendations of an external Project Advisory Committee, the research focused on demonstration of a simulation-based procedure for assessing the increased hazard and risk potentially associated with induced seismicity at a specific GCS site, and a laboratory experiment to investigate the potential for CO_2 leakage resulting from slip-induced permeability changes along caprock faults. The research activities were centered at King Island near Lodi in the southern Sacramento Valley, which a previous study had identified as a high-potential storage site and for which a set of characterization data is available.

Numerical modeling of CO_2 injection into the Mokelumne River Sandstone, a depleted natural gas reservoir under King Island, was carried out and used to predict time-dependent pore pressure changes on local faults for input to simulations of induced seismicity. The modeling included the local geometry of the Mokelumne River formation taken from a regional geologic model, and two faults loosely based on picks from a 3D seismic survey. The local stratigraphy and formation porosities and permeabilities were derived from the comprehensive suite of well logs from the CG1 well at King Island.

Simulations were carried out for injection rates of 8 Mt/year and 12 Mt/year and a range of assumed fault permeability values. Increasing the injection rate increased the magnitude of pressure change proportionately, but had little effect on the overall pattern of CO_2 movement or pressure response. However, decreasing the fault permeability greatly impacted both the spatial distribution of CO_2 and the magnitude of the pressure response. Lower fault-core permeability meant that the faults acted as strong barriers to lateral spreading of CO_2 within the storage formation, and the lower fault-outer-conduit (damage zone) permeability meant that the ability of the CO_2 to move upward by buoyancy flow through the faults was also curtailed.

The same geologic model was used to investigate the effects of CO_2–methane mixing on the long-term pressure rise resulting from CO_2 injection into a depleted natural gas reservoir, and the sensitivity to reservoir porosity and reservoir and fault permeability. It was observed that the pressure rise resulting from injection of CO_2 into a reservoir containing residual methane is lower than the case of a reservoir filled with 100% aqueous phase because of the larger compressibility of CH_4 compared to water. It was found that the effect of mixing is negligible because it is damped by pressure diffusion in the reservoir and even relatively weak hydraulic connectivity to surrounding aquifers.

Application of the simulation-based probabilistic seismic hazard and nuisance risk analysis to King Island site was intended to demonstrate the type of procedure that could be applied during the planning phase of an industrial-scale GCS project. Synthetic seismicity simulations utilized the geologic model developed for the flow modeling, and the pressure histories calculated on the two faults for the 8Mt/year injection scenario. To estimate hazard and risk uncertainties, multiple realizations of the seismicity catalogs used to estimate earthquake occurrence frequencies

randomly sampled the uncertainty distributions of the stress field, fault slip rates and parameters of the rate-and-state frictional law used for the seismicity simulations. The demonstration results show a modest increase in the hazard during and after injection, but these translate to only small increases in the risk of nuisance at all levels of acceptability. The risk of damage even at a site close to the two active faults is very low.

The tectonic setting of King Island is essentially unknown, but for this demonstration a faulting style, fault slip rates and in situ stresses based on extrapolation of sparse regional data were adopted. All of these parameters are highly uncertain because the stress state in particular is not constrained by local measurements of in situ stress magnitudes. Direct measurements of seismic wave velocities, needed both to derive rock elastic properties and densities and to calculate ground motions from the simulated earthquakes, are available for only a limited depth range in the CG1 well and from a local shallow tomography model. Therefore, sparse regional data and generic relationships were used to estimate velocities and properties for depths down to 6 km, but these are again uncertain.

A laboratory direct-shear experiment was carried out on a single, synthetically-induced fracture within a Mont Terri Opalinus Clay core sample. The objective was to measure the shear displacement on the fracture and the accompanying change in fracture permeability after it had been activated by increasing the pore pressure. However, the fracture sealed immediately after pore fluid having a chemical composition similar to that of the in situ brine at Mont Terri was introduced in the sample, resulting in a total loss of fracture permeability. This is attributed to the high ductility and high content of water-sensitive, swelling clays in Opalinus Clay. The result of this sealing effect was that under an applied stress state estimated to be representative of in situ stress at the depth of the Capay Shale under King Island, externally applied pore pressures well above the estimated critical pressure for fault activation failed to activate shear displacement on the fracture. Subsequent further increases in shear stress resulted in shear failure of the rock matrix rather than slip along the fracture.

The large uncertainties mentioned above in several of the parameters used in the hydrological and seismicity simulations are largely the result of the lack of complete site –specific characterization data for King Island. The primary requirement for a real-world application of the simulation-based risk assessment method (and other potential methods) will be a comprehensive site characterization that includes site-specific measurements of the in situ stress state and rock properties. The scale of the characterization studies required will depend on the volume of the crust affected by increased pressures, which could best be estimated by preliminary hydrological modeling of the planned injection using existing data.

The hydrological modeling demonstrated the large impact that fault permeabilities have on the magnitudes and distribution of subsurface pressure changes. Because the factors that govern fault permeabilities are very poorly known in general, this highlights the importance of in situ measurements of the characteristics and properties of local faults. A significant limitation in current earthquake simulations used to estimate induced seismicity hazard is that potential slip-induced changes in fault permeability are not yet coupled back into the flow simulation. Although

this is feasible computationally, the current poor state of knowledge about shear slip-related permeability changes, particularly in sedimentary rocks, means that it not yet possible to assess the effect of this lack of coupling on the simulation results.

This fundamental knowledge gap also significantly limits the ability to assess the impact of fault slip during earthquakes on caprock integrity. The experimental work discussed in Chapter 7 demonstrates the strong influence that plastic deformation and swelling of a clay-rich shale can have on its hydrological properties, and consequently on the mechanical strength of fractures and faults. The self-healing effect apparent in the experiment has important implications for the leakage potential along faults within the shale caprock of a CO_2 storage reservoir. This experiment was one of the first to investigate pressure-and slip-related permeability and strength changes specifically in a caprock shale. Experiments are ongoing at several institutions, but, considering its importance to GCS, there is a need for accelerated future research on this important topic.

Recent Mesoscale (1-10 m) experiments performed in underground research facilities (e.g., Guglielmi et al, 2015) are beginning to provide fundamental insights into the interplay among slip, permeability, pressure and fault zone architecture, and can also be used as a bridge to investigate the scaling between laboratory and field measurements. Continued investment in this type of research could also provide needed constraint on the scaling of parameters in the rate-and-state frictional law empirically derived from laboratory observations to field dimensions. Studies that simulate the seismicity actually observed at well-characterized fluid injection sites will be crucial in calibrating and validating these parameters before the simulation-based method can be applied with confidence to assess the potential risks associated with future GCS projects. These studies should be linked to empirical investigations of the relationship of seismicity to fluid injection, particularly at sites where high-volume disposal of wastewater from oil and gas production and other industrial processes is taking place. Upon the recommendation of the Project Advisory Committee such an investigation was not carried out as part of this project, but a study, which includes the needed augmentation of publically-available databases, has since been sponsored by the California Department of Conservation.

Because the characterization of King Island used in the demonstration falls short of what will be required for an actual industrial-scale GCS project, the site hazard and risk assessment results from this study can by no means be regarded as definitive for this site. However, the results could be indicative of the general impact that CO_2 injection might have at sites in California having similar characteristics to the King Island scenario and where the background seismic hazard and risk are low. The CO_2 injection rate of 8 Mt/year is about double that for the largest GCS projects currently planned, but is considered to be representative of future industrial-scale projects.

This timely study provides an assessment of the state of knowledge surrounding the issue of induced seismicity and makes a major contribution in informing policy makers how the potential risks associated with induced seismicity from geological carbon sequestration can be assessed during the planning and permitting stage of a project. It also lays out the remaining challenges to putting this assessment to work in practice, and what are some of the future research priorities that will contribute to its successful application. As the state considers adopting CCS as a

greenhouse gas reduction strategy while safeguarding ratepayers, property and the environment, it will be important to assure that agencies tasked with formulating regulations for and permitting future GCS projects in California continue to be aware of this study.

GLOSSARY

3D	Three-Dimensional
ANSS	Advanced National Seismic System
ARB	(California) Air Resources Board
CCS	Carbon capture and Storage
CEC	California Energy Commission
CEQA	California Environmental Quality Act
CG1	Citizen Green #1 (research well)
CISN	California Integrated Seismic Network
CMR	Combinable Magnetic Resonance
CSUB	California State University, Bakersfield
DOGGR	(California) Department of Oil and Gas Resources
EIR	Environmental Impact Report
EOR	Enhanced Oil Recovery
EOS	Equation of State
EPA	(U.S.) Environmental Protection Agency
FEMA	(U.S.) Federal Emergency Management Agency
FTE	Full Time Equivalent
GCS	Geological Carbon Sequestration
GHG	Greenhouse Gas
GMPEs	Ground Motion Prediction Equations
GPS	Global Positioning System
HECA	Hydrogen Energy California
LBNL	Lawrence Berkeley National Laboratory
LCFS	Low Carbon Fuel Standards
LLNL	Lawrence Livermore National Laboratory
LVDT	Linear Variable Differential Transducer
MRV	Monitoring, Verification, and Reporting
Mt	Million tonnes (metric tons)
NCEDC	Northern California Earthquake Data Center
NIST	National Institute of Standards and Technology
NMR	Nuclear Magnetic Resonance
PAC	Project Advisory Committee
PAR	Pressure Area of Review
PSRA	Probabilistic Seismic Risk Analysis
QM	Quantification Methodology
SCEC	Southern California Earthquake Center

SCECDC	Southern California Earthquake Center Data Center
U.S. EPA	United States Environmental Protection Agency
U.S. FEMA	United States Federal Emergency Management Agency
UIC	Underground Injection Control
USGS	United States Geological Survey
VSP	Vertical Seismic Profile
WSM	World Stress Map

REFERENCES

Amadei, B., and O. Stephansson, 1997. *Rock Stress and its Measurement*, Chapman and Hall, New York, 490p.

Ben-Zion, Y., 2008. Collective behavior of earthquakes and faults: Continuum-discrete transitions, progressive evolutionary changes, and different dynamic regimes, *Rev. Geophys.*, **46,** RG4006, 70p.

Beyer, J.H., J. Ajo-Franklin, C. Doughty, T. Kneafsey, S. Nakagawa, and E. Burton, 2012. Geologic characterization for CO_2 storage in California's Sacramento Basin, Carbon Storage R&D Project Review Meeting, National Energy Technology Laboratory, Pittsburgh, Aug 21-23, http://www.westcarb.org/pdfs/KingIslandPoster.pdf.

Birkholzer, J.T., A. Cihan, and Q. Zhou, 2012. Impact-driven pressure management via targeted brine extraction—Conceptual studies of CO_2 storage in saline formations, *Int. J. Greenhouse Gas Control*, **7**, 168–180.

Bossart, P. *Characteristics of Opalinus Clay at Mont Terri*, https://www.mont-terri.ch/en/geology /properties-and-characteristic-values.html, accessed March, 2017.

Brocher, T., 2005. Empirical relations between elastic wavespeeds and density in the Earth's crust. *Bull. Seismol. Soc. Am.*, **95**, 2081-2092.

Brocher, T., 2008. Compressional and shear-wave velocity versus depth relations for common rock types in Northern California, *Bull. Seismol. Soc. Am.*, **98**, 950-968.

Budnitz, R., G. Apostolakis, D. Boore, L. Cluff, K. Coppersmith, C. Cornell, and P. Morris, 1997. *Recommendations for Probabilistic Seismic Hazard Analysis: Guidance on Uncertainty and Use of Experts*, *NUREG/CR-6372*, 170p, U.S. Nuclear Regulatory Commission, Washington, DC.

Burton, E., J.H. Beyer, and N. Mateer, 2015. *Assessment of the Barriers and Value of Applying CO₂ Sequestration in California*, Report CEC-500-2015-100 prepared by Lawrence Berkeley National Laboratory and the California Institute of Energy and Environment for the California Energy Commission, Sacramento CA, 134p.

Burton, E., N. Mateer, R. Myhre, and M. Stone, 2016. *WESTCARB Phase III Final Report: Summary of California Activities*, Report CEC-500-2016-053 prepared by the California Institute of Energy and Environment for the California Energy Commission, Sacramento CA, 49p.

California Carbon Capture and Storage Review Panel, 2010. *Findings and Recommendations by the California Carbon Capture and Storage Review Panel*; accessed from http://www.climatechange.ca.gov/carbon_capture_review_panel.

California Institute for Energy and Environment, 2010. *Background Reports for the California Carbon Capture and Storage Review Panel*, Berkeley, California; accessed from http://www.climatechange.ca.gov/carbon_capture_review_panel.

Cappa, F., and J. Rutqvist, 2012. Seismic rupture and ground acceleration induced by CO_2 injection in the shallow crust, *Geophys. J. Intl.*, **190**, 1784-1789.

Chanchani, S., M.D. Zoback, and C. Barton, 2003. A case study of hydrocarbon transport along active faults and production-related stress changes in the Monterey formation, California, In: *Fracture and In-situ Stress Characteristics of Hydrocarbon Reservoirs*, A. Ameen (ed.), Geol. Soc. London. Spec. Pub., **209**, 17-26.

Colburn, R., and W. Mooney, 1986. Two-dimensional velocity structure along the synclinal axis of the Great Valley, California, *Bull. Seismol. Soc. Am.*, **76**, 1305-1322.

Cornell, A., 1968. Engineering seismic risk analysis, *Bull. Seismol. Soc. Am.*, **58**, 1583-1606.

Dalay, T., R. Haught, J. Peterson, K. Boyle, J. Beyer, and L. Hutchings, 2010. *Seismicity Characterization and Monitoring at WESTCARB's Proposed Montezuma Hills Geologic Sequestration Site*, Lawrence Berkeley National Laboratory Report LBNL-4006E, 10p.

Dieterich, J., 1978. Time-dependent friction and the mechanics of stick-slip. *Pure Appl. Geophys.*, **116**, 790-85.

Dieterich, J, and K. Richards-Dinger, 2010. Earthquake recurrence in simulated fault systems, *Pure Appl. Geophys.*, **167**, 1087–1104.

Dieterich, J, K. Richards-Dinger, and K. Kroll, 2015. Modeling injection-induced seismicity with the physics-based earthquake simulator RSQSim, *Seismol. Res. Lett.* **86**:4, 1-8.

Doughty, C. and L.R. Myer, 2009. Scoping calculations on leakage of CO_2 in geologic storage: the impact of overburden permeability, phase trapping, and dissolution, In: McPherson, B.J. and Sundquist, E.T. (eds), *Science and Technology of Carbon Sequestration*. Geophysical Monograph 183, American Geophysical Union, Washington DC.

Doughty, C., B.M. Freifeld, and R.C. Trautz, 2008. Site characterization for CO_2 geologic storage and vice versa: The Frio brine pilot, Texas, USA as a case study, *Environmental Geology*, **54**, 1635–1656.

Douglas, J., et al., 2013. Predicting ground motion from induced earthquakes in geothermal areas, *Bull. Seismol. Soc. Am.*, **103,** 1875-1897.

Dowding, C., 1996. *Construction Vibrations*, Prentice Hall, Upper Saddle River, 610p.

Eberhart-Phillips, D., C. Thurber, and J. Fletcher, 2014. Imaging *P* and *S* attenuation in the Sacramento-San Joaquin Delta Northern California, *Bull. Seismol. Soc. Am.*, **104**, 2322-2336.

Ellsworth, W. (2013). Injection-Induced Earthquakes, *Science, 341*, 142–149.

Fault Analysis Group, 2014. 3D *Relays from Seismic Data*, University College Dublin: https://www.fault-analysis-group.ucd.ie/gallery/3Drelay.htm.

FEMA, 2013. HAZUS, The Federal Emergency Management Agency's (FEMA's) Methodology for Estimating Potential Losses from Disasters; http://www.fema.gov/hazus

Field, E., et al., 2014. Uniform California earthquake rupture forecast, Version 3 (UCERF3)–the time-independent model, *Bull. Seismol. Soc. Am.*, **104**, 1122-1180.

Fletcher, J., and J. Boatwright, 2013. Site response and basin waves in the Sacramento-San Joaquin Delta, California, *Bull. Seismol. Soc. Am.*, **103**, 196-210.

Freeze, R.A., and J.A. Cherry, 1979. *Groundwater*, Prentice-Hall, Englewood Cliffs, NJ, 604p.

Gephart, J. and D. Forsyth, 1984. An improved method for determining the regional stress tensor using earthquake focal mechanism data: Application to the San Fernado earthquake sequence, *J. Geophys. Res.*, **89**, 9305-9320.

Gischig, V., and S. Weimer, 2013. A stochastic model for induced seismicity based on non-linear pressure diffusion and irreversible permeability enhancement, *Geophys. J. Intl.*, **194**, 1229-1249.

Goertz-Allmann, B., and S. Wiemer, 2013. Geomechanical modeling of induced seismicity source parameters and implications for seismic hazard assessment, *Geophysics*, **78**, KS25-KS39.

Graves, R., and A. Pitarka, 2010. Broadband ground-motion simulation using a hybrid approach, *Bull. Seismol. Soc. Am.*, **104**, 2095-2123.

Guglielmi, Y., D. Elsworth, F. Cappa, P. Henry, C. Gout, P. Dick, and J. Durand 2015. In situ observations on the coupling between hydraulic diffusivity and displacements during fault reactivation in shales, *J. Geophys. Res.*, **120**, 7729-7748.

Hauksson, E., W. Yang, and P. Shearer, 2012. Waveform relocated earthqauke catalog for southern California (1981 to June 2011), *Bull. Seismol. Soc. Am.*, **102**, 2239-2244.

Heidbach, O., Tingay, M., Barth, A., Reinecker, J., Kurfeß, D., and Müller, B. 2008. *The World Stress Map* database release 2008, doi:10.1594/GFZ.WSM.Rel2008.

Holbrook, W., and W. Mooney, 1987. The crustal structure of the axis of the Great Valley, California, from seismic refraction measurements, *Tectonophysics*, **140**, 49-63.

Hutchings, L., E. Ioannidou, W. Foxall, N. Voulgaris, J. Savy, Ioannis Kalogeras, L. Scognamiglio, and G. Stavrakakis, 2007. A physically-based strong ground-motion prediction methodology: Application to PSHA and the 1999 $M_W = 6.0$ Athens earthquake, *Geophys. J. Intl.*, **168**, 659-680.

Ijiri, Y., H. Saegusa, A. Sawada, M. Ono, K. Watanabe, K. Karasaki, C. Doughty, M. Shimo, and K. Fumimura, 2009. Evaluation of uncertainties originating from the different modeling approaches applied to analyze regional groundwater flow in the Tono area of Japan, *J. Contaminant Hydrology*, **103**, 168–181.

Jaeger, J., N. Cook, and R. Zimmerman, 2007. *Fundamentals of Rock Mechanics*, 4th Ed., Blackwell Publishers, Oxford.

Juanes, R., B. Hager, and H. Herzog, 2012. No geologic evidence that seismicity causes fault leakage that would render large-scale carbon capture and storage unsuccessful, *Proc. Natl. Acad. Sci. USA*, **109**, E3623.

Karasaki, K., C. Doughty, C.T. Onishi, and J. Goto, 2015. Development of geohydrologic model of the Wildcat Fault zone, *Transport in Porous Media*, **108**, 3-22.

Kennedy, R.P., C.A. Cornell, R.D. Campbell, S. Kaplan, and H.F. Perla, 1980. Probabilistic seismic safety study of an existing nuclear power plant, *Nuclear Engineering and Design*, **59**, 315-318.

Keranen, K., H. Savage, G. Abers, and E. Cochran 2013. Potentially Induced Earthquakes in Oklahoma, USA: Links between Wastewater Injection and the 2011 Mw 5.7 Earthquake Sequence, *Geology*, *41*, 699–702.

Linstrom, P.J. and W. Mallard, 2001. NIST Chemistry webbook; NIST standard reference database No. 69.

Ludwig, W., J. Nafe, and C. Drake, 1970. Seismic Refraction; in *The Sea*, A. Maxwell (ed.), **4**, Wiley Interscience, New York, 53-84.

Majer, E.; J. Nelson, A. Robertson-Tait, J. Savy, and I. Wong, 2016. *Best Practices for Addressing Induced Seismicity Associated With Enhanced Geothermal Systems (EGS)*, LBNL report: http://esd1.lbl.gov/files/research/projects/induced_seismicity/egs/Best_Practices_EGS_Induced_Seismicity_8-APR-2016.pdf

Marone, C., 1998. Laboratory-derived friction laws and their application to seismic faulting, *Annu. Rev. Earth. Planet. Sci*, *26*, 643–696.

McClure, M., and R. Horne, 2011. Investigation of injection-induced seismicity using a coupled fluid flow and rate/state friction model, *Geophysics*, **76**, WC181-WC198.

Myer, L, L. Chiaramonte, T. Daley, D. Wilson, W. Foxall, and J. Beyer, 2010. *Potential for Induced Seismicity Related to the Northern California CO_2 Reduction Project Pilot Test, Solano County, California*, Lawrence Berkeley National Laboratory Report LBNL-3720E, 13p.

Michael, A., 1987. Use of focal mechanisms to determine stress.: A control study, *J. Geophys. Res.*, **92**, 357-368.

Millington, R. and J. Quirk, 1961. Permeability of porous solids, *Trans. Faraday Soc.*, **57**, 1200-1207.

Murphy, J., 1990. *Data report for the Great Valley, California, Axial Seismic Refraction Profiles*, US Geological Survey Open-File Report 89-494, 36p.

Musson R., 2000. The use of Monte-Carlo simulations for seismic hazard assessment in the UK, *Annali Di Geofisica*, **43**:1, 1-9.

Narasimhan, T.N. and P.A. Witherspoon, 1976. An integrated finite difference method for analyzing fluid flow in porous media, *Water Resources Research*, **12**, 57 − 64.

National Research Council 2013. *Induced Seismicity Potential in Energy Technologies*. National Academies Press, Washington, D.C., 1787p.

Oldenburg, C., K. Pruess, and S.M. Benson, 2001. Process modeling of CO_2 injection into natural gas reservoirs for carbon sequestration and enhanced gas recovery, *Energy & Fuels*, **15**, 293-298.

Oldenburg, C., S. Stevens, and S.M. Benson, 2004a. Economic feasibility of carbon sequestration with enhanced gas recovery (CSEGR), *Energy*, **29**, 1413-1422.

Oldenburg, C.M., G.J. Moridis, N. Spycher, and K. Pruess, 2004b. *EOS7C version 1.0: TOUGH2 Module for Carbon Dioxide or Nitrogen in Natural Gas (Methane) Reservoirs*, Lawrence Berkeley National Laboratory Report LBNL-56589.

Oldenburg, C., P. Jordan, A. Mazzoldi, J. Wagoner, S. Bryant, and J-P. Nicot. 2010. *Certification Framework: Leakage Risk Assessment for CO_2 Injection at the Montezuma Hills Site, Solano County, California*, WESTCARB Phase II Final Report, Appendix 16.

Pan, L., N. Spycher, C. Doughty, and K. Pruess, 2016. ECO2N V2.0: A TOUGH2 Fluid Property Module for Modeling CO_2-H_2O-NaCl Systems to Elevated Temperatures of up to 300ºC, *Greenhouse Gas: Science and Technology*, in press.

Prescott, W., J. Savage, J. Svarc, and D. Manaker, 2001. Deformation across the Pacific-North America plate boundary near San Francisco, California, *J. Geophys. Res.*, **106**, 6673-6682.

Pruess, K., 2004. The TOUGH codes—A family of simulation tools for multiphase flow and transport processes in permeable media, *Vadose Zone J.*, **3**, 738 - 746.

Pruess, K. and N. Müller, 2009. Formation dry-out from CO_2 injection into saline aquifers: 1. Effects of solids precipitation and their mitigation, *Water Resources Research*, **45**, W03402.

Pruess, K., C. Oldenburg, and G. Moridis, 2012. *TOUGH2 user's guide, Version 2*, Lawrence Berkeley National Laboratory Report LBNL-43134, Berkeley, CA.

Pruess, K., J. García, T. Kovscek, C. Oldenburg, J. Rutqvist, C. Steefel, and T. Xu, 2004. Code intercomparison builds confidence in numerical simulation models for geologic disposal of CO_2, *Energy*, **29**, 1431– 1444.

Richards-Dinger, K., and J. Dieterich, 2012. RSQSim earthquake simulator, *Seismol. Res. Lett.*, **83**, 983–990.

Ruina, A., 1983. Slip instability and state variable friction laws, *J. Geophys. Res.*, **88**, 10,359-10,370.

Rummel, F., 1987. Fracture mechanics approach to hydraulic fracturing stress measurements; in *Fracture Mechanics of Rock*, B. Kean-Atkinson (ed.), 217-240, Academic Press Geology Series.

Saikia, C., 1994. Modified frequency-wavenumber algorithm for regional seismograms using Filon's quadrature: modelling of L_g waves in eastern North America, *Geophys. J. Intl.*, **118**, 142-158.

Scholz, C.H., 2002. *The Mechanics of Earthquakes and Faulting*, Cambridge University Press, 471p.

Teel, 2012. *Seismic Tomography of the Sacramento-San Joaquin River Delta: Joint P-wave/Gravity and Ambient Noise Methods*, Ph.D. Dissertation, Univ. Wisconsin-Madison, 95p.

Unruh, J., and C. Hitchcock, 2009. *Characterization of Potential Seismic Sources in the Sacramento-San Joaquin Delta, California*, Final Technical Report, US Geological Survey Award No. 08HQGR005, Reston, VA.

Van Genuchten, M.Th., 1980. A closed-form equation for predicting the hydraulic conductivity of unsaturated soils, *Soil Sci. Soc. Am. J.*, **44**, 892-898.

Veneziano D., C. Cornell, and T. O'Hara, 1984. *Historical Method of Seismic Hazard Analysis*, Report EPRI NP 3438, Elec. Power Res. Inst.

Vilarrasa, V., and J. Carrera, 2015. Geologic carbon storage is unlikely to trigger large earthquakes and reactivate faults through which CO_2 could leak, *Proc. Natl. Acad. Sci. USA*, **112**, 5938-5943.

Waldhauser, F., and D. Schaff, 2008. Large-scale relocation of two decades of Northern California seismicity using cross-correlation and double-difference methods, *J. Geophys. Res.*, **113**, B08311, doi:10.1029/2007JB005479.

Weingarten, M., S. Ge, J. Godt, B. Bekins, and J. Rubinstein 2015. High-rate injection is associated with the increase in U.S. mid-continent seismicity, *Science*, **348**, 1336-1340.

White, J.A., and W. Foxall, 2016. Assessing induced seismicity risk at CO_2 storage projects: Recent progress and remaining challenges, *Int. J. Greenhouse Gas Control*, **49**, 413-424.

Yang, W., E. Hauksson, and P. Shearer, 2012. Computing a large refined catalog of earthquake focal mechanisms for southern California (1981-2010): Temporal stability of the style of faulting, *Bull. Seismol. Soc. Am.*, **102**, 11789-1194.

Yeck, W., G. Hayes, D. McNamara, J. Rubinstein, W. Barnhart, P. Earle, and H. Benz 2017. Oklahoma experiences largest earthquake during ongoing regional wastewater injection hazard mitigation efforts, *Geophys. Res. Lett.*, **44**, 711-717.

Zoback, M.L., 1992. First- and second-order patterns of stress in the lithosphere: The World Stress Map project, *J. Geophys. Res.*, **97**, 11703-11728.

Zoback, M.D., and S. Gorelick, 2012, Earthquake triggering and large-scale geologic storage of carbon dioxide, *Proc. Natl. Acad. Sci. USA*, **109**, 10164-10168.

Zoback, M.D., and S. Gorelick, 2015. To prevent earthquake triggering, pressure changes due to CO_2 injection need to be limited, *Proc. Natl. Acad. Sci. USA*, **112**, E4510.

Zoback, M.D., D. Moos, L. Mastin, and R. Anderson, 1985. Well bore breakouts and in situ stress, *J. Geophys. Res.*, **90**, 5523-5530.

APPENDIX A:
Project Advisory Committee Members and Workshop Agenda

A-1: Project Advisory Committee Members

Name	Affiliation
David Stoms	California Energy Commission
Larry Myer	Lawrence Berkeley National Laboratory, retired (Coordinator)
Colleen Barton	Baker Hughes
Emily Brodsky	University of California, Santa Cruz
David Dempsey	Stanford University
Tom Dewers	Sandia National Laboratory
Matt Gerstenberger	GNS Science, New Zealand
Thomas Göbel	California Institute of Technology
Roland Gritto	Array Information Technology
Bill Harbert	University of Pittsburg
Steve Hickman	U.S. Geological Survey
David McNamara	GNS Science, New Zealand
Jean Savy	Savy Risk Consulting
Stephanie Vaille	Curtin University, Australia
Herb Wang	University of Wisconsin, Madison
Josh White	Lawrence Livermore National Laboratory
Ivan Wong	URS Corporation

AGENDA

LBNL Workshop on Potential for Induced Seismicity Related to CO$_2$ Injection in California

Thursday, December 18, 2014

San Francisco Marriott Marquis - Foothill F, 2nd Floor

780 Mission St.

San Francisco, CA 94103

Map/directions: http://www.marriott.com/hotels/maps/travel/sfodt-san-francisco-marriott-marquis/

12:35 pm	Welcome and introduction	Liz Burton
12:45	Lunch	
1:15	Project and workshop objectives	
1:30	Summary of 2014 Data Acquisition Tasks	
	California DOGGR and EPA well data	Preston Jordan
	Geological characterization	Preston Jordan
	Seismicity, faults and stress field	Bill Foxall
	King Island deep research well	Jonathan Ajo-Franklin
2:00	2015 Draft Scope of Work	
	Seismicity-injection correlation analysis	Corinne Bachmann
	Integration of King Island core data	Jonathan Ajo-Franklin
	Effects of CO$_2$/CH$_4$ mixing	Curt Oldenburg
	King Island simulation-based seismic risk analysis	Bill Foxall
2:30	Discussion and recommendations	All (Larry Myer compiles)
3:00	Adjourn	

LBNL Points of Contact: Liz Burton   (510) 486-6696

Bill Foxall   (510) 486-5082

Tom Daley (510) 486-7316

Ami Singh (510) 486-6455

APPENDIX B:
Report By The Project Advisory Committee On The CEC/LBL Induced Seismicity Project Review

B-1: Executive Summary

The Lawrence Berkeley National Laboratory (LBNL), as part of the research portfolio of the Earth Sciences Division, is carrying out a research project on induced seismicity, which is funded by the California Energy Commission (CEC). The project is carried out in two Phases. At the completion of the first Phase, the scope of work calls for a Project Advisory Committee (PAC) of subject matter experts to review Phase I results, and make recommends on priorities for Phase II activities. On December 18, 2014, in San Francisco, LBNL researchers presented results of Phase I and their plans for Phase II activities to the PAC. Overall, the committee found that the initial investigations, though preliminary, are insightful and of excellent quality, addressing several key technical issues. The proposed activities for Phase II are all of value, as is discussed in the following narrative, in addressing project objectives. However, because of limited project budget there is a need to focus and prioritize these activities. The committee recommends that high priority be given to activities, including laboratory and modeling, which utilizes and builds upon data previously obtained from the King Island research well.

B-2: Observations, Findings and Recommendations of the PAC

The objective of the project is to "Evaluate the potential for induced seismicity and resulting ground shaking and leakage risks associated with commercial-scale injection of CO_2 in California". The technical team includes 8 researchers from LBNL, and three from the California Geologic Survey. The total level of effort for Phase I was about 0.5 FTE (Full Time Equivalent) LBNL Staff Scientist and about 1.3 FTE for Phase II. The project leverages other, current, California State-funded research on hydrofracturing. It is also leveraging data previously obtained from a research well drilled at King Island in the southern Sacramento Basin.

In Phase I, LBNL assembled publically available, relevant, data and carried out some preliminary analyses in order to form the basis for Phase II activities

LBNL reviewed oil field production and injection data available at DOGGR, focusing on the Stevens, Vedder and Temblor formations in the Southern San Joaquin Basin. These formations are potential candidates for storage. Two pools in the Vedder were identified as having net positive fluid fluxes, that is, injected volumes larger than produced volumes. This implies that current reservoir pressures might be greater than original, pre-production pressures. However, few, if any, pressure measurements were available in the data sets available at DOGGR.

The observation that there are existing reservoir pools in which injection has resulted in pressures which may exceed virgin levels is important because such pressure conditions are likely to occur in saline formation storage of CO_2 and are thought to increase the risk of induced seismicity. Studies to identify net positive flux reservoir pools in other basins in California would be valuable. Further study of such pools, including reservoir simulation and geomechanical modeling, combined with analysis of seismicity regionally associated with these reservoirs, could provide

valuable new understanding of the potential for induced seismicity in these and similar potential CO_2 storage formations in California. However, the value of such studies will be very dependent upon the quality of data available as input for the modeling. Key data on reservoir pressures, in-situ stress, and reservoir properties apparently are not easily available from public sources. It is unclear to what extent such data may exist from proprietary sources. InSAR data might be available as a proxy for subsurface pressure measurements. Given the limited resources available in Phase II, further study of these reservoir pools is not a high priority for Phase II.

Two UIC Class I wells which inject large volumes of fluids in the San Joaquin basin were also identified. Like the positive flux reservoir pools, these projects could be used for reservoir simulation and geomechanical modeling to assess induced seismicity, but such efforts would also suffer from the same limitations.

Analysis of historical data on seismicity is important for understanding the potential for induced seismicity. In Phase I, LBNL assembled data from NCSN and SCEDC catalogs and produced a map of minimum magnitude detection thresholds for the San Joaquin Basin. The value of additional analysis of the San Joaquin data to establish possible correlations with water disposal wells was unclear, but would require considerable effort to resolve inconsistencies in the catalogues and other issues.

Using seismicity data in the Ventura and Santa Maria Basins, some preliminary analyses were carried out to determine if statistical correlations might exist between the location of injection wells and recorded seismicity. Two approaches were used: frequency-magnitude distribution analysis, and nearest distance analysis. For the Ventura Basin, no apparent correlation was found between b-values and location of injection wells. In the Santa Maria Basin, however, the nearest distance analyses showed promise for developing correlations between injection volume and pressure history of individual wells and recorded seismicity. This observation is noteworthy because previous studies of correlations between seismicity and oil and gas operations in California have been limited and have not resulted in definitive correlations. Continuation and expansion of the Phase I effort to develop statistical correlations between injection wells and recorded seismicity would be of great value but it was unclear if sufficient resources could be allocated to this effort in Phase II.

Previous work on the King Island "Citizen Green #1" deep research well provides an excellent basis for Phase II activities which are important for understanding the potential for induced seismicity in California. The advantages of focus on the King Island site include:

-   Relevance of the site to geologic storage in California. Formations representing potential CO_2 storage targets for California are present at the site and are intercepted by the well. These include the Domengine, Mokelumne River, and Starkey sandstone formations along with their overlying, regionally persistent shale seals.
-   Geologic structure of relevance to project objectives. The King Island field is fault bounded on two sides
-   Large database. This includes core (including rare core of a regional seal), extensive well logs, regional logs, and 3D seismic
-   Results of prior analyses. These include well log interpretations, various core measurements, and reservoir modeling studies

One potential disadvantage of the site is the lack of data on in-situ stresses and formation pressures. Serious consideration should be given to further processing of well logs (e.g., FMI) and mining of drilling records and reports for relevant information. Regional data on seismicity was not discussed, but should be assessed and analyzed if it is of sufficient quality (a figure presented at the meeting shows the minimum magnitude detection threshold in the area of King Island to be about 1.5). If a longer term study of King Island could be considered, it would be valuable to install instrumentation for monitoring of seismicity. The cost vs benefit of analysis of the available 3D seismic data needs to be assessed.

LBNL proposed three inter-related Phase II activities based on the King Island site: laboratory measurements on core; reservoir and geomechanical simulation; and induced seismicity hazard analysis.

Laboratory testing of the Nortonville core represents a potential unique, important contribution of the Phase II effort. Very little information is available on the geomechanical properties of shale seals, in general, and particularly in California, which makes the proposed stress dependent fracture permeability tests of high value. Serious consideration should be given to expanding the scope of the laboratory measurements on fractured core to include shear deformation, in order to specifically address the mechanics of fault slip in shale seals as well as potential leakage resulting from slip.

Phase II reservoir flow and geomechanical modeling should build upon previous modeling carried out for the site. Ultimately, management of induced seismicity will require accurate prediction of reservoir pressures, so reservoir and geomechanical simulators need to incorporate the physical processes which affect pressure. However, given the limited resources available for Phase II activities, as well as uncertainty in other important input parameters such as in-situ stress, significant effort devoted to code development is difficult to justify. Pressurization due to $CO_2 - CH_4$ mixing is a process which should be incorporated into the Phase II reservoir flow and geomechanical models of King Island as long as code modifications are not required.

The proposed Phase II work on probabilistic seismic hazard and risk assessment is important because it supports the development of a framework for calculation of the seismic hazard associated with induced seismicity in California. The King Island site offers a good test case for further validation of the framework. Input for the seismic hazard and risk assessment includes reservoir simulation and rock/fracture properties data from the other two proposed King Island-related Phase II activities. It also requires a distribution of fault properties which should be calibrated against Central Valley induced seismicity observations, and data on long-term fault slip rates, but it is unclear to what extent this information is available, or what the required level of effort is to develop it. If Phase II resources are sufficient, King Island provides an opportunity to investigate the potential for induced seismicity related to CO_2 injection in Central Valley geological and tectonic environment.

APPENDIX C:
Overview of Rate-and-State Friction and Its Implementation in the RSQSim Earthquake Simulator

Rate-and-state frictional laws like the one employed in the RSQSim earthquake simulator were empirically derived from laboratory experiments, and provide the most complete description of the mechanics of earthquake nucleation and the entire earthquake cycle currently available (Ben-Zion, 2008). According to these laws, the frictional sliding resistance of a fault is a function of the instantaneous fault slip rate, V, and evolves with the "state" of the fault (e.g., Dieterich, 1978; Ruina, 1983; Marone, 1998). The particular rate-and-state law employed in RSQSim contains a single state variable, θ, that has the dimensions of time and which is interpreted as the typical lifetime of the asperities at which the two sides of the fault are in contact. This "aging" law is expressed by the following functional relationships:

$$\mu(V,\theta) = \mu_0 + a\ln\left(\frac{V}{V^*}\right) + b\ln\left(\frac{V^*\theta}{D_c}\right), \tag{C.1}$$

in which μ is the current coefficient of friction, a and b are experimentally determined dimensionless constants, V is the instantaneous slip rate, V^* is a reference slip rate and μ_0 is the steady-state coefficient of friction at the reference slip speed and constant normal stress. θ is the state variable, which evolves at the current slip rate over a characteristic distance D_c according to an aging law given by:

$$\frac{\partial\theta}{\partial t} = 1 - \frac{V\theta}{D_c} - \alpha\frac{a\theta}{b\sigma}\frac{\partial\sigma}{\partial t}, \tag{C.2}$$

where α is an empirical constant. From these two equations, the response to a step change in slip rate is an initial, instantaneous increase in frictional resistance governed by the constant a (the *rate* effect) followed by a drop to a final value μ over slip distance D_c (the *state* effect). The net effect depends on the relative values of a and b. If $b>a$ then slip-weakening and slip acceleration occurs that can lead to the nucleation of unstable slip in an earthquake. Conversely, if $a<b$ then the fault is slip-strengthening and only stable, aseismic sliding can occur.

Determining appropriate bounds on most of the rate-and-sate parameters and the scaling of the laboratory-derived parameters a, b, and D_c to earthquake dimensions and crustal conditions remains the subjects of vigorous ongoing research (e.g. Marone, 1998; Ampuero and Rubin, 2008; Fang et al., 2011).

While the rate-and-state law provides an adequate description of the quasi-static process by which earthquakes nucleate and are arrested—and hence the seismic cycle that produces earthquake sequences—it does not represent the full elastodynamics of coseismic fault rupture over the order of seconds duration of the actual earthquake; i.e. the law does not give a description of dynamic earthquake slip and the generation of seismic waves. RSQSim provides a first-order approximation of the elastodynamic effects using two correction parameters

(Richards-Dinger and Dieterich, 2012). The first parameter addresses the observation in fully dynamic simulations of earthquake rupture (e.g. Madariaga, 1976) that the stress drop during an earthquake overshoots the sliding frictional level predicted by quasi-static calculations. Therefore, the stress on a fault element during dynamic coseismic slip is generally lower than predicted by the rate-and-state law. RSQSim mimics this by applying a stress overshoot factor, *s*, specified as an input parameter, that governs the stress level at which coseismic slip ceases and a fault element heals.

The second parameter corrects for the tendency of RSQSim simulations to underestimate the dynamic stress concentration at the edge of a fault element induced by the rupture of the element (which nucleates at the center). This makes it unrealistically difficult to overcome the resistance to rupture of adjoining elements posed by the *a* (strengthening) term in the first equation above, hence inhibiting multi-segment ruptures and larger earthquakes. This problem is particularly acute when large elements (~km) are used to simulate large tectonic earthquakes (Richards-Dinger and Dieterich, 2012), but should be less so for the smaller (50m) elements used in the simulations of typically smaller induced earthquakes. To address this problem, RSQSim temporarily reduces the *a* values at elements adjacent to elements undergoing seismic slip by a factor *fa* < 1, specified as an input parameter.

Although these two corrections, and particularly the latter, are somewhat *ad hoc*, appropriate ranges of both the stress overshoot and *fa* parameters have been calibrated to some extent by comparison of RSQSim results with fully dynamic simulations (Dieterich and Richards-Dinger, 2010; Richards-Dinger and Dieterich, 2012). A preliminary analysis of the sensitivity of earthquake simulations to some of the parameters was carried out by Trainor-Guiton et al. (2016).

Appendix C References

Ampuero, J-P, A. Rubin, 2008. Earthquake nucleation on rate and state faults – Aging and slip laws, *J. Geophys. Res.*, **113**, B01302: doi:10.1029/2007JB005082, 21p.

Ben-Zion, Y., 2008. Collective behavior of earthquakes and faults: Continuum-discrete transitions, progressive evolutionary changes, and different dynamic regimes, *Rev. Geophys.* **46,** RG4006, 70p.

Dieterich, J., 1978. Time-dependent friction and the mechanics of stick-slip, *Pure Appl. Geophys.*, **116**, 790-85.

Dieterich, J, and K. Richards-Dinger, 2010. Earthquake recurrence in simulated fault systems, *Pure Appl. Geophys.*, **167**, 1087–1104.

Fang, Z., J. Dieterich, and K. Richards-Dinger, 2011. Earthquake nucleation on faults with nonconstant normal stress, *J. Geophys. Res.*, **116**, B09307, doi:10.1029/2011JB008196, 13p.

Madariaga, R., 1976. Dynamics of an expanding circular fault, *Bull. Seismol. Soc. Am.* **66**, 639–666.

Marone, C., 1998. Laboratory-derived friction laws and their application to seismic faulting, *Ann. Rev. Earth. Planet. Sci*, *26*, 643–696.

Richards-Dinger, K., and J. Dieterich, 2012. RSQSim earthquake simulator, *Seismol. Res. Lett.* **83**, 983–990.

Ruina, A., 1983. Slip instability and state variable friction laws, *J. Geophys. Res.*, **88**, 10,359-10,370.

Trainor-Guiton, W., W. Foxall, and S. Johnson, 2016. *Parameter Sensitivity Analysis with the Seismicity Simulation Program RSQSim*, NRAP-TRS-III-006-2016, NRAP Technical Report Series, National Energy Technology Laboratory, Morgantown, WV, 24p.